

Passive remote sensing of the atmospheric boundary layer in Colorado’s East River Valley during the seasonal change from snow-free to snow-covered ground

Bianca Adler¹, James M. Wilczak², Laura Bianco³, Ludovic Bariteau⁴, Christopher Cox², Gijs de Boer⁴, Irina V. Djalalova², Michael R Gallagher⁵, Janet Intrieri², Tilden Meyers², Timothy A Myers⁴, Joseph Olson², Sergio Pezoa⁶, Joseph Sedlar⁷, Elizabeth Smith⁸, David D. Turner⁹, and Allen B. White³

¹CIRES, University of Colorado Boulder, NOAA, PSL

²National Oceanic and Atmospheric Administration (NOAA)

³Cooperative Institute for Research in Environmental Sciences

⁴University of Colorado Boulder

⁵CIRES/NOAA-ESRL

⁶NOAA/ESRL/Physical Sciences Division

⁷NOAA Global Monitoring Laboratory

⁸National Severe Storms Laboratory

⁹NOAA Earth System Research Laboratory

January 17, 2023

Abstract

The structure and evolution of the atmospheric boundary layer (ABL) under clear-sky fair weather conditions over mountainous terrain is dominated by the diurnal cycle of the surface energy balance and thus strongly depends on surface snow cover. We use data from three passive ground-based infrared spectrometers deployed in the East River Valley in Colorado’s Rocky Mountains to investigate the response of the thermal ABL structure to changes in surface energy balance during the seasonal transition from snow-free to snow-covered ground. Temperature profiles were retrieved from the infrared radiances using the optimal estimation physical retrieval TROPoe. A nocturnal surface inversion formed in the valley during clear-sky days, which was subsequently mixed out during daytime with the development of a convective boundary layer during snow-free periods. When the ground was snow covered, a very shallow convective boundary layer formed, above which the inversion persisted through the daytime hours. We compare these observations to NOAA’s operational High-Resolution-Rapid-Refresh (HRRR) model and find large warm biases on clear-sky days resulting from the model’s inability to form strong nocturnal inversions and to maintain the stable stratification in the valley during daytime when there was snow on the ground. A possible explanation for these model shortcomings is the influence of the model’s relatively coarse horizontal grid spacing (3 km) and its impact on the model’s ability to represent well-developed thermally driven flows, specifically nighttime drainage flows.

1 **Passive remote sensing of the atmospheric boundary**
2 **layer in Colorado’s East River Valley during the**
3 **seasonal change from snow-free to snow-covered ground**

4 **Bianca Adler^{1,2}, James Wilczak,² Laura Bianco^{1,2}, Ludovic Bariteau^{1,2},**
5 **Christopher J. Cox², Gijs de Boer^{1,2,3}, Irina Djalalova^{1,2}, Michael Gallagher^{1,2},**
6 **Janet M. Intrieri², Tilden Meyers,⁴ Timothy Myers^{1,2}, Joseph B. Olson⁵,**
7 **Sergio Pezoa^{1,2}, Joseph Sedlar^{1,6}, Elizabeth Smith⁷, David D. Turner⁵, Allen**
8 **White²**

9 ¹Cooperative Institute for Research in Environmental Sciences (CIRES), University of Colorado Boulder

10 ²NOAA Physical Sciences Laboratory, Boulder CO

11 ³IRISS, University of Colorado, Boulder CO

12 ⁴NOAA Air Resources Laboratory, Boulder CO

13 ⁵NOAA Global Systems Laboratory, Boulder CO

14 ⁶NOAA Global Monitoring Laboratory, Boulder CO

15 ⁶NOAA National Severe Storms Laboratory, Norman OK

16 **Key Points:**

- 17 • Temperature profiles retrieved from remotely sensed infrared radiances allow to
18 study the valley boundary layer over different snow covers.
- 19 • The nocturnal inversion in a high-altitude mountain valley is mixed out under snow-
20 free conditions and persists during daytime over snow.
- 21 • NOAA’s operational weather prediction model struggles to correctly forecast the
22 boundary layer likely due to the too coarse grid spacing.

Abstract

The structure and evolution of the atmospheric boundary layer (ABL) under clear-sky fair weather conditions over mountainous terrain is dominated by the diurnal cycle of the surface energy balance and thus strongly depends on surface snow cover. We use data from three passive ground-based infrared spectrometers deployed in the East River Valley in Colorado’s Rocky Mountains to investigate the response of the thermal ABL structure to changes in surface energy balance during the seasonal transition from snow-free to snow-covered ground. Temperature profiles were retrieved from the infrared radiances using the optimal estimation physical retrieval TROPoe. A nocturnal surface inversion formed in the valley during clear-sky days, which was subsequently mixed out during daytime with the development of a convective boundary layer during snow-free periods. When the ground was snow covered, a very shallow convective boundary layer formed, above which the inversion persisted through the daytime hours. We compare these observations to NOAA’s operational High-Resolution-Rapid-Refresh (HRRR) model and find large warm biases on clear-sky days resulting from the model’s inability to form strong nocturnal inversions and to maintain the stable stratification in the valley during daytime when there was snow on the ground. A possible explanation for these model shortcomings is the influence of the model’s relatively coarse horizontal grid spacing (3 km) and its impact on the model’s ability to represent well-developed thermally driven flows, specifically nighttime drainage flows.

Plain Language Summary

We investigated how the vertical temperature structure in a high-altitude mountain valley in Colorado’s Rocky Mountains evolves over snow-free and snow-covered ground. The vertical temperature structure in valleys determines how well air and thus pollutants in the valley can be mixed with the air above and is thus decisive for air quality and human health. During the night, air near the surface cools more than air above leading to an increase of temperature with height, a so-called temperature inversion forms which suppresses vertical mixing. During the day, solar radiation warms the ground and vertically mixes the air in the valley. When the ground is snow-covered, the mixing is limited to a shallow layer of a few hundred meter depth adjacent to the surface and the nocturnal inversion persists above through the daytime hours trapping air in the valley. We compared the observations to NOAA’s operational forecast model and found that minimum nighttime temperatures and daytime mixing were overestimated by the model, especially over snow-covered ground. We attributed the model errors to the relatively coarse horizontal grid spacing of 3 km, which suggests that a reduction of grid spacing in the operational model could improve the forecast accuracy in mountainous terrain.

1 Introduction

The atmospheric boundary layer (ABL) is the lowest part of the atmosphere that is directly affected by the Earth’s surface (Stull, 1988). Over mountainous terrain under clear sky fair weather conditions, the evolution of its structure is forced by convection and thermally driven circulations (Zardi & Whiteman, 2013; Serafin et al., 2018), which, in turn, are influenced by diurnal and terrain-induced variability in surface radiation and energy balance. Nighttime radiative cooling and drainage flows (i.e. downslope and downvalley winds) lead to formation of a surface temperature inversion in valleys and basins, that is, a layer in which temperature increases with height. Depending on the magnitude of energy input at the surface during the day, the nocturnal temperature inversions may erode after sunrise, either due to the upward growth of a well-mixed convective boundary layer (CBL) and/or the descent of the inversion top (Whiteman, 1982). While the convective heating in snow-free valleys is usually sufficient to erode the nocturnal inversion (e.g. Herrera-Mejía & Hoyos, 2019; Adler, Gohm, et al., 2021), multi-

73 day low-level inversions may persist in snow-covered valleys with very shallow CBLs form-
74 ing above the ground (e.g. Chemel et al., 2016; Llargeron & Staquet, 2016a, 2016b; Adler,
75 Wilczak, et al., 2021). During periods with strong persistent inversions, pollutants can
76 accumulate in valleys with significant implications for air quality and human health (e.g.
77 Lareau et al., 2013; Llargeron & Staquet, 2016b). Over areas of continuous snow cover,
78 average net radiation and sensible heat flux are often negative during wintertime (e.g.
79 Cullen & Conway, 2015; Stigter et al., 2021; Mott et al., 2018) meaning that solar en-
80 ergy is reflected and the surface is emitting energy, primarily at longer (infrared) wave-
81 lengths. Over patchy horizontally heterogeneous snow cover, very large differences in albedo
82 and surface fluxes occur on small scales, internal boundary layers form, and local advec-
83 tion of sensible heat becomes relevant (Mott et al., 2018).

84 Errors and uncertainties in mesoscale numerical weather prediction (NWP) mod-
85 els are usually amplified over mountainous terrain compared to flat terrain (Zhong & Chow,
86 2013, and references therein). One common problem is that nocturnal inversions in val-
87 leys are often too weak compared to observations, which may result in misrepresenta-
88 tion of the breakup of inversions during the day. Model performance largely depends on
89 the specific configuration, including details related to horizontal and vertical grid spac-
90 ing, domain extent, grid nesting, and the initial and boundary conditions applied. Also,
91 the physical parameterizations employed, such as turbulence and boundary layer param-
92 eterizations, land surface models (LSM), land use data sets, and radiation models, play
93 a central role in dictating model performance. One item that is known to be particularly
94 problematic is the model’s horizontal grid spacing, as coarse resolution limits the capa-
95 bility of the model to represent the detailed orographic structure of mesoscale valleys and
96 tributaries. Additionally, terrain smoothing used in some NWP systems results in the
97 underestimation of elevation differences between ridges and valley floors. Evaluating the
98 configuration of a specific model is also impacted by coarse resolution, as the detailed
99 observations required for such evaluation are often from instrumentation deployed to a
100 single location. This is particularly problematic in areas of complex terrain, where there
101 can be substantial variability in ABL conditions over very short distances. For exam-
102 ple, large differences between simulated and observed ABL thermal structure may re-
103 sult if observational data collected on a valley floor is compared to the nearest model grid
104 point, located on the adjacent slope. In general, high resolutions are required to accu-
105 rately portray flows over complex terrain, in part due to the need to have multiple grid
106 points present to detect features of interest. For example, to resolve flow features such
107 as thermally driven winds, the feature scale should be 6-8 times the horizontal grid spac-
108 ing according to Skamarock (2004) and Skamarock and Klemp (2008). This means that
109 models with a grid spacing on the order of 2-3 km would not be able to adequately cap-
110 ture features of less than 15 km in scale.

111 Much of the research on the ABL structure and evolution in snow-covered valleys
112 is based on *in situ* measurements on surface towers or airborne platforms such as radioson-
113 des and tether sondes. While the latter give detailed information on the vertical struc-
114 ture of the ABL, the measurements are not continuous and only provide snapshots. This
115 can be problematic in areas where atmospheric conditions evolve at time scales signif-
116 icantly shorter than those observed by these platforms. Great potential to gain a deeper
117 insight in the evolution of the vertical thermal ABL structure comes from ground-based
118 remote sensing instruments such as passive microwave radiometers and infrared spec-
119 trometers and active water vapor absorption lidars (Turner & Löhnert, 2021), which pro-
120 vide continuous information on the profiles of temperature and humidity. Such instru-
121 ments have been successfully deployed to study, for example, the summertime ABL in
122 a valley on the mountainous island of Corsica (Adler & Kalthoff, 2014), the wintertime
123 ABL in a snow-covered valley in the French Alps (Chemel et al., 2016), and the ABL
124 in a tropical valley in the Colombian Andes (Herrera-Mejía & Hoyos, 2019). The eval-
125 uation of NWP models in mountainous terrain is often based on near-surface measure-
126 ments only, as these measurements are widespread and readily available. However, im-

127 portant quantities like ABL depth and thermal stratification can only be evaluated against
128 profile measurements which emphasizes the value of continuous remotely sensed profiles
129 for NWP model evaluation. By utilizing both types of observations, Adler, Wilczak, et
130 al. (2022) evaluated the representation of a wintertime persistent cold air pool in differ-
131 ent versions of the National Oceanic and Atmospheric Administration (NOAA) opera-
132 tional High-Resolution-Rapid-Refresh (HRRR) model.

133 In this study, we investigate the response of the ABL thermal vertical structure to
134 changes in the energy balance at the surface during the seasonal transition from snow-
135 free to snow-covered ground in a high-altitude valley using continuous remotely sensed
136 temperature profiles. We then compare these observations to the operational HRRR model
137 to evaluate the model performance and investigate possible reasons for model errors. To
138 clearly isolate the response of the ABL to changes in snow cover and to avoid compli-
139 cating factors such as low-level clouds or synoptically-driven flows, we focus on completely
140 clear-sky days. Our research questions are grouped into two sets of questions, with the
141 first focused on process understanding, and the second focused on model evaluation: (i)
142 What is the vertical thermal structure of the ABL under different snow-cover conditions
143 and how does that structure change along the valley? How do the nocturnal tempera-
144 ture inversion, CBL, and stratification in the valley atmosphere vary temporally and spa-
145 tially? (ii) How well does the operational HRRR model capture the conditions in the val-
146 ley? Do the model errors depend on the time of the day, snow cover, and meteorolog-
147 ical situation, and do they vary along the valley?

148 To address these questions, we use data from a collaborative research initiative cur-
149 rently ongoing in the East River Watershed of Colorado. This work includes efforts as-
150 sociated with the National Oceanic and Atmospheric Administration (NOAA) Study of
151 Precipitation, the Lower Atmosphere, and Surface for Hydrometeorology (SPLASH, NOAA
152 Physical Science Laboratory, 2021b) and the U.S. Department of Energy (DOE) Atmo-
153 spheric Radiation Measurement (ARM) program Surface Atmosphere Integrated Field
154 Laboratory (SAIL, Feldman et al., 2021) campaigns. The main focus of the SPLASH ini-
155 tiative is to enhance weather and water prediction capabilities by measuring, evaluat-
156 ing, and understanding integrated atmospheric and hydrologic processes relevant to wa-
157 ter resources. The East River Watershed is a representative mountainous headwater catch-
158 ment of the Colorado River Basin, which is a primary source of water for much of the
159 southwestern United States. As part of the multi-year SPLASH and SAIL field campaigns,
160 three passive remote sensing infrared spectrometers were deployed simultaneously along
161 the axis of the East River Valley for a three-month period from the end of October 2021
162 to the end of January 2022, covering the seasonal change from snow-free to snow-covered
163 ground. To our knowledge, this is the first time such an instrument combination is used
164 to study the spatio-temporal characteristics of the ABL in a high-altitude valley. To ob-
165 tain temperature profiles from infrared spectrometers, we use an optimal estimation phys-
166 ical retrieval (i.e. Tropospheric Remotely Observed Profiling via Optimal Estimation (TROPOe
167 Turner & Löhnert, 2014; Turner & Blumberg, 2019; Turner & Löhnert, 2021). We then
168 compare the observations to model output at the grid point closest to the stations to in-
169 vestigate model errors under different snow-cover conditions.

170 The manuscript is structured as follows: Section 2 describes the investigation area
171 as well as the observational and model data. In Sect. 3, the temporal evolution of ob-
172 served near-surface conditions, including radiation and energy balance components dur-
173 ing the whole 3-month period, is analyzed (Sect. 3.1). This is followed by an investiga-
174 tion of the observed diurnal cycle of the ABL on a day-to-day basis at one site (Sect. 3.2)
175 and along the valley axis using 24-h composites (Sect. 3.3). In Sect. 4, the ABL ther-
176 mal structure in the HRRR model is evaluated (Sect. 4.1) and possible reasons for the
177 model errors are discussed (Sect. 4.2).

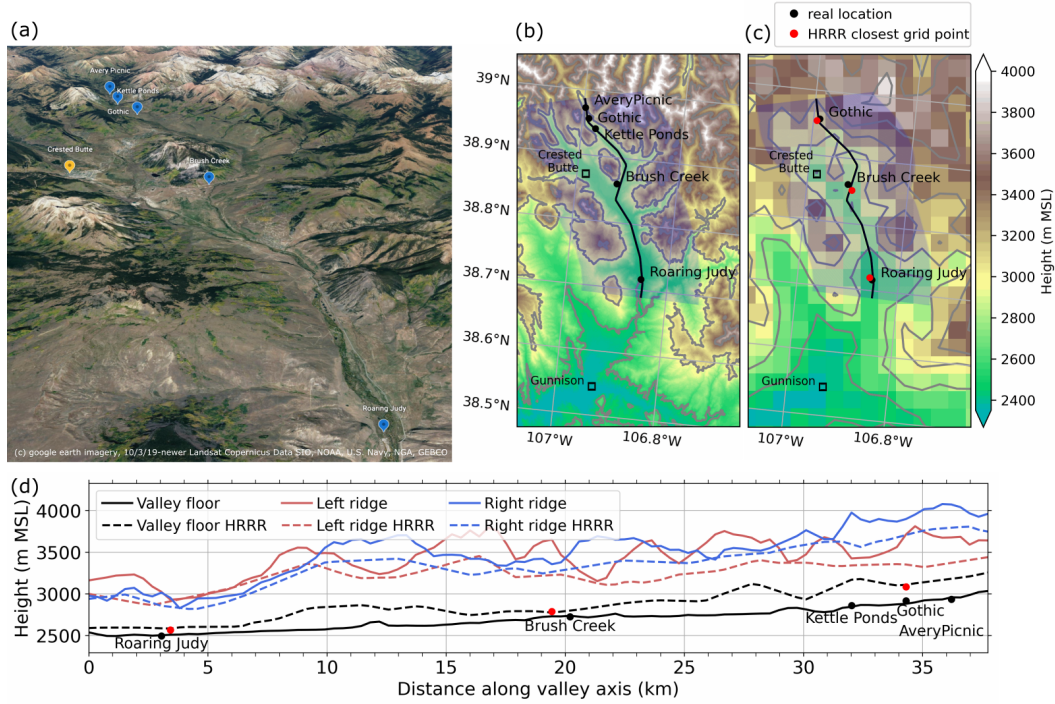


Figure 1. (a) Google earth imagery of the investigation area. Terrain height (b) based on 30-m resolution elevation data from the Shuttle Radar Topography Mission and (c) as used in the operational HRRR model with 3 km grid spacing. (d) Elevation of the valley floor and ridges (left and right of the valley axis when looking upvalley) computed from SRTM and HRRR elevation data along the axis of the East River Valley indicated by the black line in (b) and (c). The shaded polygon in (b) and (c) marks the area used for the estimates of the ridge heights. Black and red dots in (b)-(d) indicate the location and heights of the sites in the real world and in the HRRR model grid.

2 Investigation area, observational, and model data

The study area is the East River Valley, which is embedded in the East River Watershed and located near Crested Butte and Gunnison in Colorado's Rocky Mountains (Fig. 1a,b). The land cover type is a mix of evergreen and deciduous forest, grasslands, and barren land (Xu et al., 2022). The distance along the valley axis from the measurement site furthest down the valley (Roaring Judy) to the site furthest up the valley (Avery Picnic) is around 35 km (Fig. 1). All measurement sites are on the valley floor. The valley floor rises from around 2500 m above mean sea level (MSL) at Roaring Judy to nearly 3000 m MSL at Avery Picnic. The valley depth on average is more than 500 m and the flat part of the valley floor ranges in width from a few kilometers at its widest part to less than 1 km near the Kettle Ponds, Gothic, and Avery Picnic sites.

While the valley orography is much smoother in the 3-km HRRR model configurations, the primary features of the valley are still resolved (Fig. 1c). To characterize the ridge height on both sites of the valley floor in the observations and simulations, we manually defined a valley axis (black line in Fig. 1b,c) and extracted elevation data along slices perpendicular to the valley axes spanning 10 km on each side. For each slice and each side of the valley we determined the maximum elevation value. Figure 1d shows the elevation of the valley floor and ridges in reality (solid lines) and in the HRRR model (dashed lines). As can be expected due to the coarse model resolution, valley depth is reduced in the model compared to reality. In an automated near-real time routine, model data at the grid points closest to the real-world locations of the sites (red dots in Fig. 1c) are extracted from the operational HRRR forecasts. We evaluated the HRRR data at Gothic, Brush Creek and Roaring Judy, since these are the sites where continuous temperature profiles from the TROPoe retrievals were available. The extracted model grid points for these sites are on the simulated valley floor (Fig. 1c,d).

2.1 Observational data

2.1.1 Thermodynamic profilers

Three ground-based infrared spectrometers were deployed along the axis of the East River Valley at Gothic, Brush Creek, and Roaring Judy during the three-month investigation period from 21 October 2021 to 28 January 2022. At Gothic, an Atmospheric Emitted Radiance Interferometer (AERI Knuteson et al., 2004b, 2004a) is operated as part of the second ARM Mobile Facility (AMF2) deployed for the SAIL campaign (Feldman et al., 2021). A second AERI was deployed at Brush Creek as part of the Collaborative Lower Atmospheric Mobile Profiling System (CLAMPS) system (Wagner et al., 2019). A third infrared spectrometer at Roaring Judy was an Atmospheric Sounder Spectrometer by Infrared Spectral Technology (ASSIST Rochette et al., 2009) operated by NOAA's Physical Science Laboratory. The AERI and ASSIST generally have the same functionality, construction, and operating principles. While the AERI at Gothic and the ASSIST at Roaring Judy were operated during the whole study period, the AERI at Brush Creek was taken down 10 days earlier on 18 January to support a separate field campaign.

The AERI and ASSIST are passive spectrometers that receive downwelling infrared radiation between the wavelengths of 3.3 and 19 μm ($520\text{-}3000\text{ cm}^{-1}$) at a spectral resolution of about 0.5 wavenumber (Knuteson et al., 2004b, 2004a). The instruments have a hatch that closes during precipitation events to protect the fore optics, which inhibits measurements during rain or snow. We retrieved thermodynamic profiles every 10 min from the observed instantaneous radiances using the optimal estimation physical retrieval TROPoe (Turner & Löhnert, 2014; Turner & Blumberg, 2019; Turner & Löhnert, 2021). The spectral bands used in the retrieval are in the wavenumber range from 612 - 905.4 cm^{-1} and are specified in Turner and Löhnert (2021). Additional input data in TROPoe are cloud base height from a colocated ceilometer, temperature and water vapor mixing ratio from near-surface measurements and from hourly analysis profiles from the op-

229 erational Rapid Refresh (RAP, Benjamin et al., 2016) weather prediction model at the
 230 closest grid point. The latter are used only outside the ABL above 4 km above ground
 231 level (AGL) and provide information in the middle and upper troposphere where little
 232 to no information content is available from the infrared radiances. In addition to these
 233 temporally resolved input data, TROPoe requires an a priori dataset (*prior*) which pro-
 234 vides mean climatological estimates of thermodynamic profiles and specifies how tem-
 235 perature and humidity covary with height as an input (for details see e.g. Djalalova et
 236 al., 2022). The prior is a key component of the retrieval and provides a constraint on the
 237 ill-posed inversion problem. For this study, we computed the prior from operational ra-
 238 diosondes launched near Denver, CO, and re-centered the mean profiles of water vapor
 239 and temperature to account for the elevation difference between the East River Valley
 240 and the launch site near Denver to get a more representative prior (for details see Ap-
 241 pendix Appendix A).

242 The retrieval determines the optimal state vector, which consists of thermodynamic
 243 profiles, and satisfies both the observations, RAP profiles above 4 km AGL, and the prior.
 244 The state vector includes temperature and water vapor profiles with 55 vertical levels
 245 each from the surface up to 17 km, with the distance between levels starting at 10 m and
 246 increasing with height, as well as liquid water path. Starting with the mean prior as a
 247 first guess of the state vector, a forward model is used to compute pseudo-observations,
 248 which are then compared to the actual observations. The retrieval iterates until the dif-
 249 ferences between the pseudo-observations and the observations are small within a spec-
 250 ified uncertainty. As the forward model, we use the Line-By-Line Radiative Transfer Model
 251 LBLRTM (Clough & Iacono, 1995; Clough et al., 2005).

252 Before running TROPoe, a principal component noise filter is applied to the infrared
 253 radiances to reduce the random error (Turner et al., 2006). Ideally, uncertainties in the
 254 observations, prior, and forward model are propagated and characterized by the poste-
 255 rior covariance matrix. Because including the uncertainty of the forward model would
 256 increase the computational costs of the retrieval substantially, we assume the uncertainty
 257 of the forward model is zero and inflate the uncertainty associated with the observed ra-
 258 diances by using the radiance uncertainty before noise filtering is applied (for details see
 259 Turner & Blumberg, 2019). Because the AERI performs longer sky averages than the
 260 ASSIST, the radiance uncertainty of the AERI is lower and we found that it was not suf-
 261 ficient to compensate for the missing uncertainty in the forward model, resulting in an
 262 overfitting of the profiles. We hence further increased the noise in the AERI radiances
 263 by multiplying the radiance uncertainties with a factor for which the retrieved temper-
 264 ature profiles best agreed with the radiosonde profiles (for details see Appendix Appendix
 265 B).

266 **2.1.2 Surface observations**

267 Measurements of 2-m temperature and horizontal wind speed and direction were
 268 obtained at five sites along the valley axis, including Avery Picnic, Gothic, Kettle Ponds,
 269 Brush Creek, and Roaring Judy. Wind measurement heights were 3.8 m AGL at Avery
 270 Picnic, 10 m AGL at Gothic, 3 m AGL at Kettle Ponds and Brush Creek, and 4 m AGL
 271 at Roaring Judy. Measurement heights refer to snow-free ground, the growing snowpack
 272 reduced the height separation between sensor and surface through the season. Up- and
 273 downwelling longwave and shortwave radiation flux components as well as 30-min sen-
 274 sible heat fluxes were measured at the upper four sites, Avery Picnic, Gothic, Kettle Ponds,
 275 and Brush Creek, and precipitation measurements were used from Gothic. In this study,
 276 net radiation is positive when directed downwards towards the surface and sensible heat
 277 flux is positive when directed upwards away from the surface.

278 All data at Gothic were collected with AMF2. At the other sites, we utilized data
 279 from Atmospheric Surface Flux Stations (ASFS, Cox et al. (2023)) at Avery Picnic and

280 Kettle Ponds (sensible heat flux only) and from mobile SURFRAD-like stations (Butterworth
 281 et al., 2021; Sedlar et al., 2022) at Brush Creek and Kettle Ponds for radiation, cloud
 282 properties, and meteorology. To estimate albedo we averaged shortwave downward and
 283 shortwave upward radiation fluxes when the solar zenith angle was less than 85° before
 284 computing the ratio. At Gothic and Brush Creek, measurements of direct and diffuse
 285 solar radiation were available to compute shortwave downward radiation fluxes (McArthur,
 286 2005), while at the other sites we used broadband fluxes. Details on the platforms and
 287 sensors can be found in the meta data for the individual data sets (see Data Availabil-
 288 ity section).

289 **2.1.3 Radiosondes**

290 As part of the AMF2 deployment, radiosondes were launched twice daily at 5 and
 291 17 MST (0 and 12 UTC) at Gothic, providing thermodynamic and wind profiles through-
 292 out the troposphere. The radiosonde profiles were used to re-center the prior (Appendix
 293 Appendix A), to help determine the optimal uncertainty configuration for the AERIs (Ap-
 294 pendix Appendix B), and to compute different ABL quantities (Sect. 3.3). When com-
 295 paring the radiosonde profiles to TROPoe retrieved profiles, we first interpolated the ra-
 296 diosonde profiles to the same height levels as the retrieved profiles to avoid differences
 297 arising from the higher vertical resolution of the sonde.

298 **2.1.4 Ceilometer**

299 Four ceilometers manufactured by Vaisala were deployed at Gothic, Kettle Ponds,
 300 Brush Creek, and Roaring Judy measuring attenuated aerosol backscatter profiles with
 301 a temporal resolution of less than 1 min. In this study, we used the first cloud-base height,
 302 as determined using Vaisala’s CL-view software, to identify clear-sky and cloudy days.
 303 At each site, we computed a daily cloud-base fraction for cloud bases below 3 km AGL.
 304 We required it to be less than 5 % at all sites for a day to be considered clear-sky and
 305 we identified cloudy days for which the temporal low-level cloud-base fraction was larger
 306 than 50 % at any of the sites.

307 **2.1.5 Terra satellite**

308 To get information on the temporal evolution of spatial snow coverage in the area,
 309 we used the normalized difference snow index (NDSI) from MODIS on-board of the Terra
 310 satellite (Hall & Riggs, 2021). Snow-covered surfaces typically have a very high reflectance
 311 in visible bands and very low reflectance in shortwave infrared bands. The NDSI reveals
 312 the magnitude of this difference. NDSI is available daily on a regular grid with 500 m
 313 spacing. We computed a mean daily NDSI for the investigation area when valid NDSI
 314 data are available for at least 50 % of the pixels and not obscured by clouds.

315 **2.2 HRRR model data**

316 We evaluated the currently operational version of NOAA’s HRRR weather predic-
 317 tion model (version 4, Dowell et al., 2022) with a horizontal grid spacing of 3 km by com-
 318 paring the observations to the closest grid point in the model (Fig. 1c). The operational
 319 HRRR model is initialized hourly with a forecast horizon of 19 h. Every 6 hours, the fore-
 320 cast horizon is extended to 48 h. For this study, we used hourly model output from the
 321 48-hr forecasts which were initialized at 0, 6, 12, and 18 UTC. For each of these initial-
 322 ization times, we split the 48-hr forecasts in half and concatenated the first and last 24
 323 hours of the forecasts, illustrated in Fig. 2. This resulted in the development of a con-
 324 tinuous time series of model data for the different configurations (i.e., eight in total with
 325 four initialization times and forecast periods 0-23 and 24-47), which we could compare
 326 against the observations. With this method, discontinuities in model data resulted at

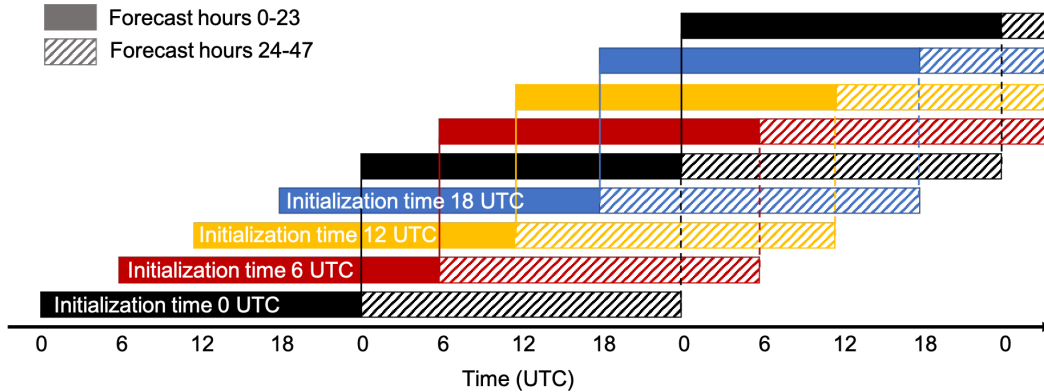


Figure 2. Illustration of the eight different configurations which are used to develop continuous time series of the HRRR model data. The different colored boxes indicate blocks of 24 h of data from runs initialized at different times, which are then concatenated to get continuous time series. Solid boxes indicate data from forecasts hour 0 to 23 and hatched boxes from 24-27.

327 the initialization times when the model data shifted from one forecast run to the next.
 328 We evaluated the model for all eight configurations and found that the main conclusions
 329 are similar for each configuration. Because of this, we decided to mostly show results from
 330 the first 24 hours of the forecasts initialized at 6 UTC (red boxes in Fig. 2).

331 Hourly model data were compared against instantaneous observation nearest in time
 332 with a maximum tolerance of 10 min, and simulated profiles were linearly interpolated
 333 to the measurement heights. Because wind observations were not performed at 10 m AGL
 334 at Brush Creek and Roaring Judy, the simulated 10-m horizontal wind data were reduced
 335 to the actual wind measurement height at the respective site assuming a logarithmic wind
 336 profile.

337 We computed 24-h composites of bias and mean absolute error (MAE) of temper-
 338 ature T as:

$$339 \quad Bias = \frac{1}{n} \sum_{i=1}^n (T_{i,model} - T_{i,obs}) \quad (1)$$

$$340 \quad MAE = \frac{1}{n} \sum_{i=1}^n |T_{i,model} - T_{i,obs}| \quad (2)$$

342 with n being the number of samples available at each hour of the day, T_{obs} being
 343 the observed temperature, and T_{model} being the simulated temperature.

344 **3 Observed evolution of the ABL during the seasonal snow cover change**

345 **3.1 Near-surface conditions**

346 Significant changes in near-surface conditions occurred during the three-month ob-
 347 servation period (Fig. 3) and these can clearly be linked to the snow cover. Smaller snow-
 348 fall events during the first half of the period (Fig. 3c) led to temporary increases in albedo
 349 (Fig. 3f), but this snow melted quickly and therefore did not result in an area-wide snow
 350 cover, as the mean NDSI values remained less than 20 % (Fig. 3d). This changed with
 351 a multi-day snowfall event between 6 and 10 December, after which the albedo increased
 352 to values larger than 0.9 and the mean NDSI remained above 60 % through the end of
 353 the investigation period in January. Using albedo and NDSI as criteria for snow cover,

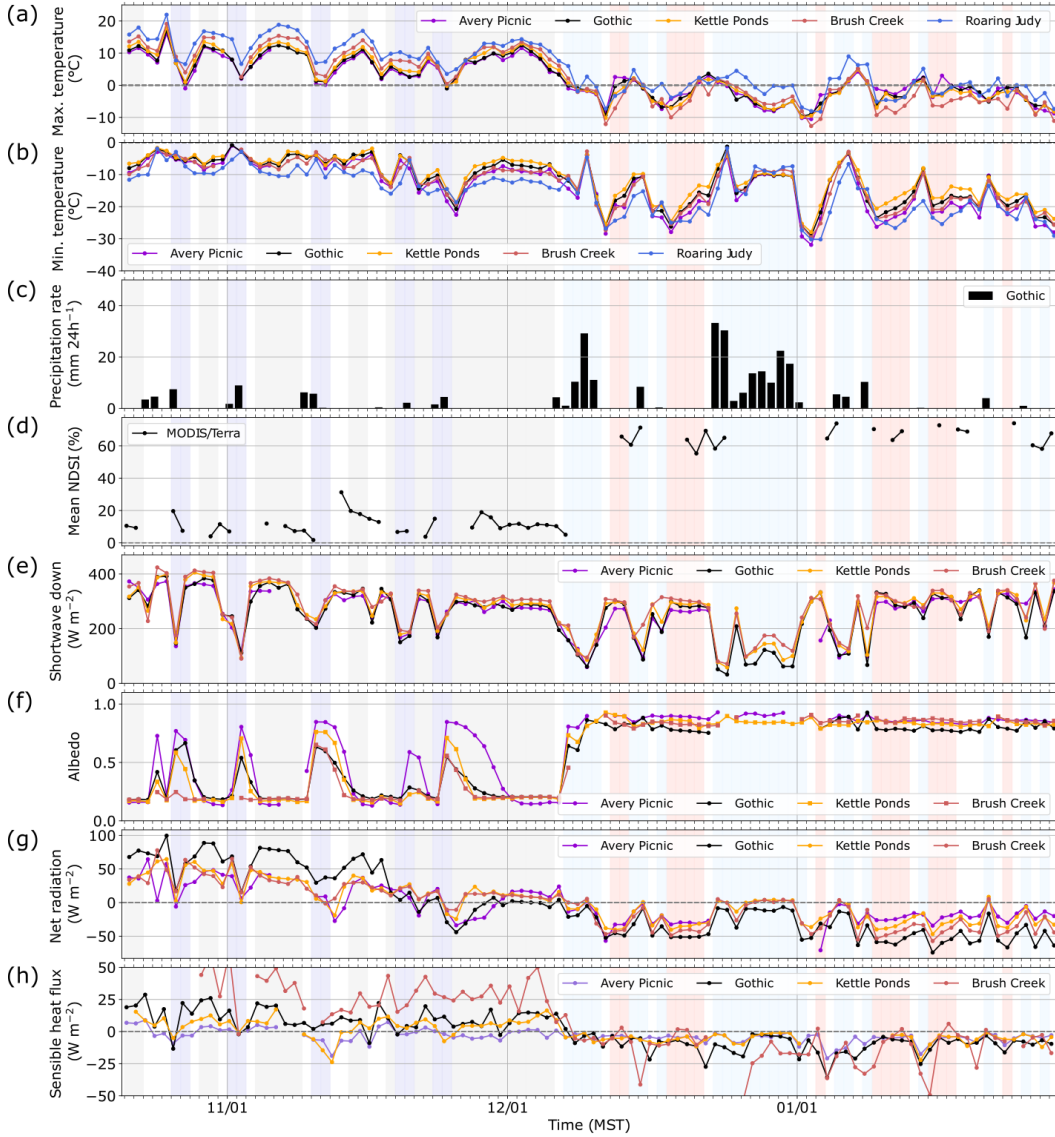


Figure 3. Daily (a) maximum and (b) minimum 2-m temperature, (c) daily precipitation rate, (d) domain mean normalized difference snow index (NDSI), (e) daily daytime mean shortwave downward radiation flux, (f) albedo at noon, (g) daily mean net radiation (positive when directed towards the surface), and (h) daily mean sensible heat flux (positive when directed away from the surface) during the 3-month investigation period. Grey and red shadings indicate clear-sky days and purple and blue shadings mark cloudy days during the snow-free and snow-covered regimes, respectively, determined using daily cloud-base fractions from ceilometers.

354 we split the observational period into two regimes. This includes a *snow-free* regime in-
 355 cluding and up to 6 December, during which any snow cover was patchy, intermittent,
 356 and heterogeneous, and a *snow-covered* regime including and following 7 December, dur-
 357 ing which a large fraction of the surface was continuously covered by snow. Visible cam-
 358 era images taken automatically at Gothic, Kettle Ponds, and Brush Creek confirmed the
 359 snow-cover change (not shown).

360 For both regimes, we identified clear-sky and cloudy days using cloud-base heights
 361 from the four ceilometers deployed along the valley axis (Sect. 2.1.4). Clear-sky days dur-
 362 ing the snow-free and snow-covered regime are indicated by gray and red shading and
 363 cloudy days by purple and blue shading in Fig. 3. During a few of the identified clear-
 364 sky days, mid-or high-level clouds occurred but were found to have a small impact on
 365 solar radiation (Fig. 3e).

366 Daily mean solar radiation on clear-sky days decreased before and increased after
 367 the winter solstice (Fig. 3e). This may explain the gradual decrease of daily mean net
 368 radiation (Fig. 3g) and daily maximum temperature (Fig. 3a) during the snow-free regime.
 369 Under snow-covered conditions, daily mean net radiation remained negative, even as one
 370 gets further away from winter solstice. Daily mean surface sensible heat flux dropped
 371 to negative values under snow-covered conditions (Fig. 3h), that is, it was directed to-
 372 wards the surface compensating for some of the surface radiative cooling (Fig. 3g). While
 373 maximum daytime temperatures regularly reached more than 10 °C under snow-free con-
 374 ditions at all sites, they generally did not exceed 0 °C on clear-sky days under snow-covered
 375 conditions (Fig. 3a). Minimum nighttime temperatures during clear-sky days were mostly
 376 between -5 to -10 °C under snow-free conditions, but regularly dropped below -20 °C un-
 377 der snow-covered conditions (Fig. 3b).

378 While the primary changes in near-surface conditions during the transition from
 379 snow-free to snow-covered ground generally occurred at all sites alike, differences are vis-
 380 ible between the sites on individual days which demonstrate the impact local terrain fea-
 381 tures can have on the surface energy balance components and air temperature. For ex-
 382 ample, the higher mean sensible heat fluxes at Brush Creek under snow-free conditions
 383 (Fig. 3h) were likely related to local site characteristics such as more rocks, more exposed
 384 aggregate, and fewer grass than at the other sites as well as its vicinity to a steep slope.
 385 Independent of snow cover, the overall lowest nighttime temperatures on clear-sky days
 386 were measured at Roaring Judy (Fig. 3b), that is the site furthest down the valley and
 387 lowest in altitude (Fig. 1) which is an indication of an extensive cold air pool filling the
 388 whole valley and which will be investigated in more detail in (Sect. 3.3). Despite being
 389 only a few kilometers apart from each other (Fig. 1d), minimum nighttime temperatures
 390 at the three sites furthest up the valley differed by several degrees with Avery Picnic mea-
 391 suring the lowest temperature (Fig. 3b). While the sites at Gothic and Kettle Ponds were
 392 not at the lowest point of the valley floor, the site at Avery Picnic was in close proxim-
 393 ity to the river and a small-scale terrain depression likely favored the formation of a lo-
 394 cal cold pool at this site.

395 3.2 Diurnal cycle of the ABL

396 After having investigated daily mean, minimum and maximum values in Sect. 3.1,
 397 we now focus on the diurnal cycle of the ABL through the snow-cover transition using
 398 measurements at Roaring Judy as an example (Fig. 4), as this was the site with the great-
 399 est and most continuous data availability for temperature profiles (Fig. 5a,b). While the
 400 2-m temperature on clear-sky days was overall lower under snow-covered conditions com-
 401 pared to snow-free conditions, a clear diurnal cycle was visible during both (Fig. 4a). Tem-
 402 perature started to increase about one hour after sunrise and started to decrease about
 403 one hour before sunset. Note that sunrise and sunset times were computed using the ge-

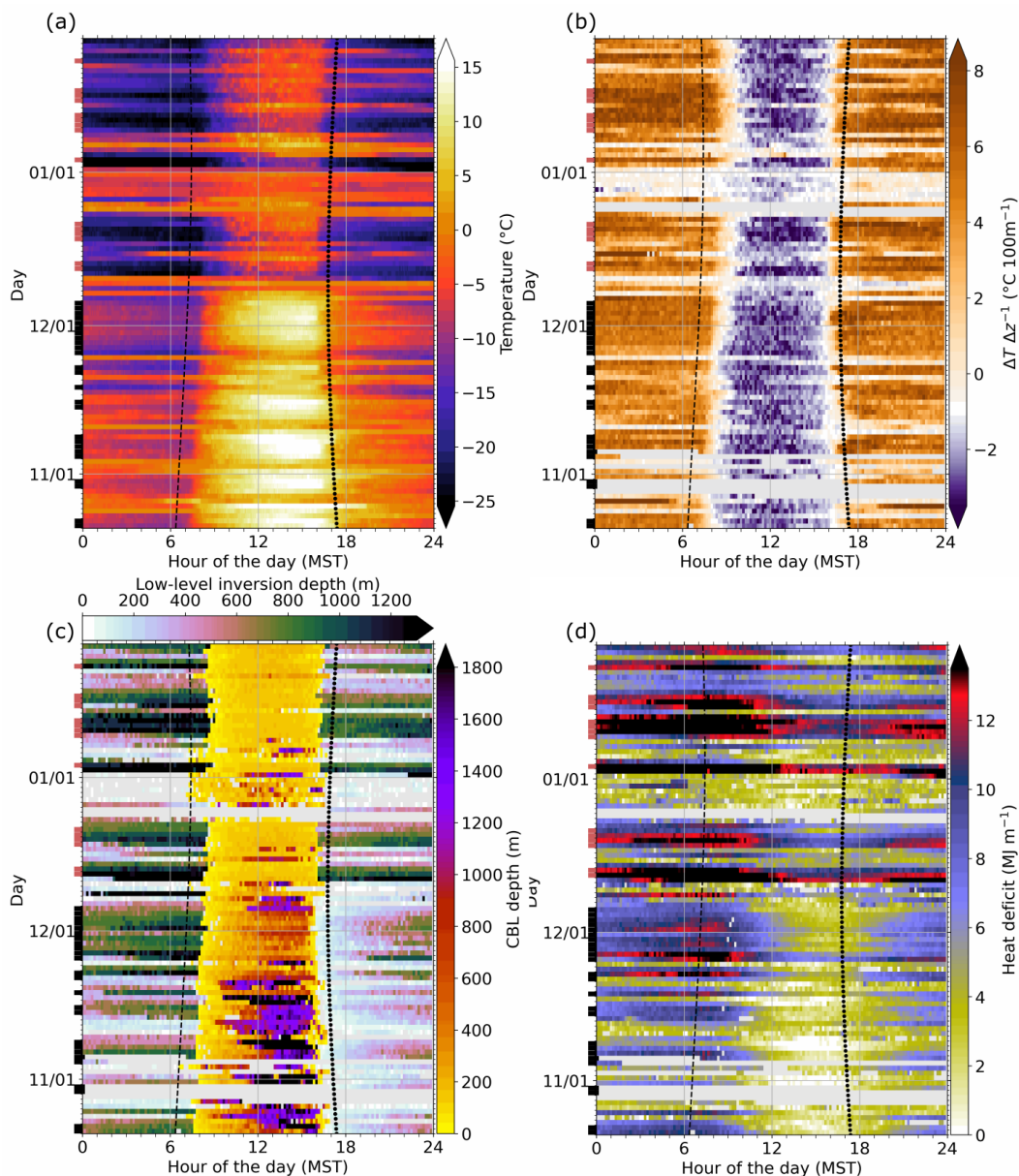


Figure 4. Daily evolution of (a) 2-m temperature, (b) temperature gradient over the lowest 100 m above ground, (c) CBL depth determined between sunrise and sunset using the parcel method and depth of the low-level inversion defined as the layer adjacent to the surface in which temperature increases with height, and (d) heat deficit computed after Eq. 3 at Roaring Judy. Besides the 2-m temperature, all quantities are computed using thermodynamic profiles retrieved with TROPoe. The dashed and dotted lines indicate sunrise and sunset, respectively. Black and red bars at the left y-axis indicate clear-sky days under snow-free and snow-covered conditions, respectively.

ographic location and do not consider local topographic impacts like shading from valley sidewalls.

Associated with the decrease in 2-m temperature shortly before sunset, a surface inversion regularly formed during clear-sky days as indicated by positive temperature gradients in the lowest 100 m AGL (Fig. 4b). Temperature gradients were typically around 5 to 6 °C 100 m⁻¹ and did not change much throughout the night. During the day, an unstable layer evolved near the surface, which was similar in strength (around -2 to -3 °C 100 m⁻¹) under both snow-cover conditions. The CBL, however, was much deeper under snow-free conditions (Fig. 4c). Its depth was computed between sunrise and sunset using the parcel method (Seibert et al., 2000), that is we determined the height at which the surface value of virtual potential temperature matched the virtual potential temperature profile. Duncan Jr. et al. (2022) found a good agreement for CBL depth estimates with the parcel method when using radiosonde and AERI-based TROPoe retrieved profiles.

The temporal evolution and depth of the stably stratified layer varied considerably with snow cover (Fig. 4c). We defined a low-level inversion as the layer adjacent to the surface in which temperature increased with height and determined its depth as the height above ground where temperature started to decrease. Under snow-free conditions, an inversion gradually formed, reaching average maximum depths of around 900 m in the early morning. In contrast when the ground was snow covered, an inversion of around 750 m depth on the average was detected as soon as the unstable layer near the surface diminished, preventing the detection of a CBL. This indicates that the very shallow CBL under snow-covered conditions was topped by a deep stably-stratified layer which connected to the surface-based inversion as soon as convection stopped. This will be investigated more in Sect. 3.3.

As a proxy for the stratification in the valley, we computed the heat deficit Q (Whiteman et al., 1999) from the surface (h_{sfc}) up to 4000 m MSL (this is the height above which we no longer found diurnal temperature changes, Sect. 3.3):

$$Q = c_p \int_{h_{\text{sfc}}}^{4000} \rho(z) [\theta_{4000} - \theta(z)] dz \quad (3)$$

where c_p is the specific heat capacity of air at constant pressure, $\rho(z)$ is the air density profile, θ_{4000} is the potential temperature at 4000 m MSL, and $\theta(z)$ denotes the potential temperature profile. With a station height of 2494 m MSL, the layer depth over which Q is computed amounts to 1500 m for Roaring Judy. Q describes the heat required to mix out the stable stratification below 4000 m MSL and to obtain a well-mixed layer with height-constant potential temperature. Small values indicate that the stratification is close to well-mixed, while large values are a sign of very stable layering. The temporal evolution of the heat deficit describes if stable layers are built, maintained or destroyed. Under snow-free conditions, the heat deficit showed a clear diurnal cycle with low values during daytime and high values during the night (Fig. 4d), reflecting the evolution of the CBL (Fig. 4c) which eroded the inversion during daytime and the build-up of the low-level inversion during nighttime. The heat deficit still generally decreased during the day under snow-covered conditions, which can be attributed to the formation of the shallow CBL (Fig. 4c) and upper-level warming (see Sect. 3.3), but the values remained much higher indicating that the stable layer was far from being mixed out. The persistent stable layer in the valley was washed out several times by synoptically-driven systems indicated by low heat deficit values (Fig. 4d), for example during the period between 24 December and 1 January, a period with heavy snowfall (Fig. 3b), but quickly rebuilt under clear-sky conditions.

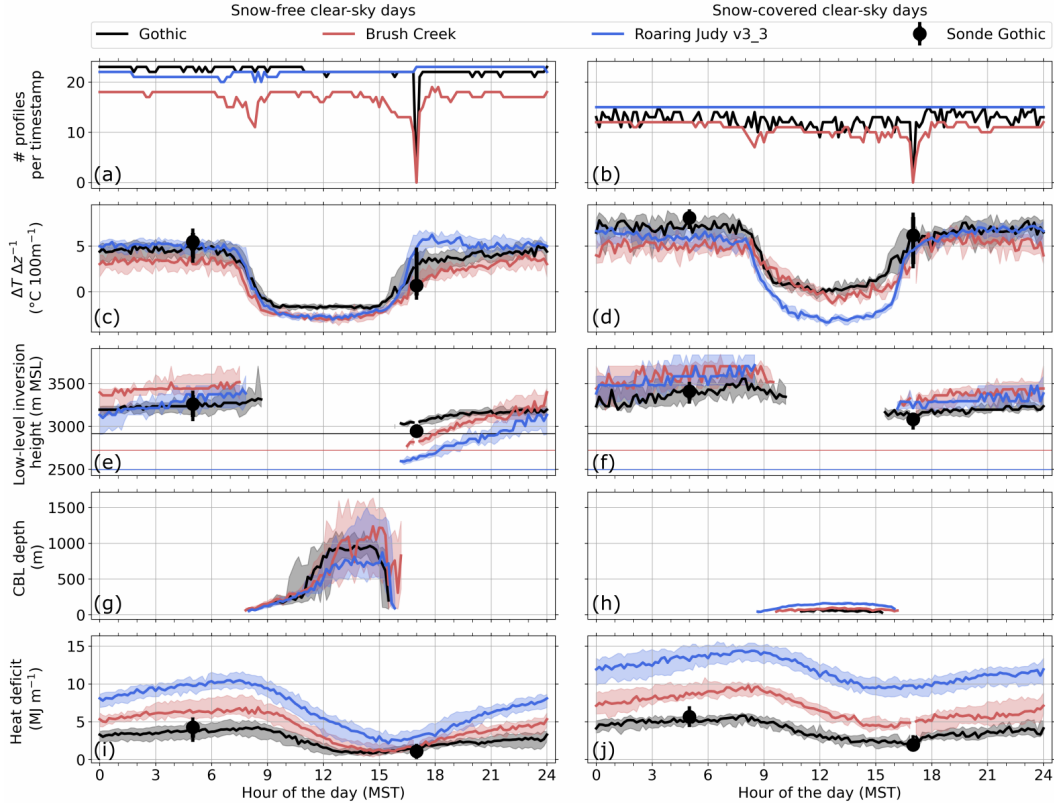


Figure 5. (a,b) Number of temperature profiles available for the analysis at each time stamp. 24-h median composites of (c,d) temperature gradient over the lowest 100 m AGL, (e,f) height of the low-level inversion defined as the layer adjacent to the surface in which temperature increases with height, (g,h) CBL depth determined between sunrise and sunset using the parcel method, and (i,j) heat deficit computed after Eq. 3 at Gothic, Brush Creek, and Roaring Judy for clear-sky days under snow-free (left column) and snow-covered (right column) conditions. In (c-j), shading marks the interquartile range. In (e,f), the thin horizontal lines indicate the respective station height. The black markers show quantities retrieved from the radio soundings at Gothic, all other quantities are computed using thermodynamic profiles retrieved with TROPoe.

452 Some of the changes we see in ABL conditions between both snow-cover regimes
 453 (Fig. 4) may be related to the reduction in solar radiation as one gets closer to winter
 454 solstice (Fig. 3d). However, the very abrupt changes right after the snowfall event ended
 455 on 10 December and the fact that the CBL depth remained low and the inversion remained
 456 deep even after solar radiation increased again in January, provide convincing evidence
 457 that the changes were dominated by snow cover strongly reflecting solar radiation and
 458 not by solar insolation.

459 3.3 Average ABL evolution along the valley axis

460 To compare the ABL evolution at the three sites Roaring Judy, Brush Creek, and
 461 Gothic along the valley axis (Fig. 1), we computed 24-h composites for clear-sky days
 462 under snow-free and snow-covered conditions of temperature profiles (Fig. 6) and, to pro-
 463 vide a quantitative analysis, of low-level stability, low-level inversion height, CBL depth,
 464 and heat deficit (Fig. 5).

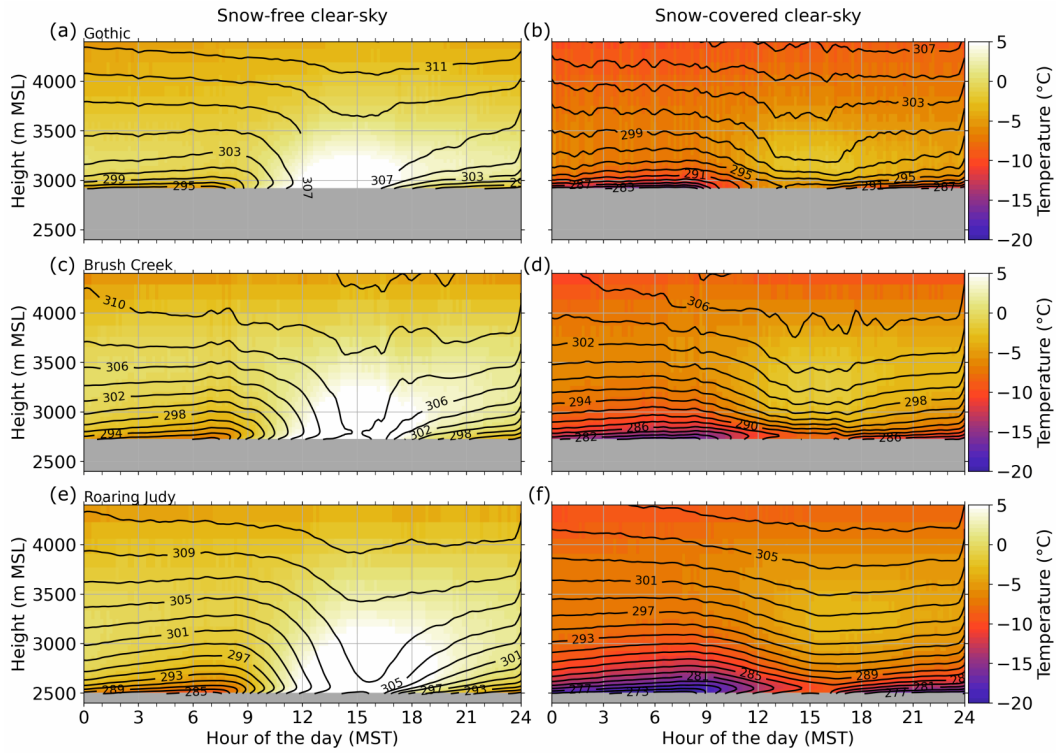


Figure 6. 24-h mean composites of temperature (color-coded) and potential temperature (iso-lines) profiles for clear-sky days under snow-free conditions (a,c,e) and snow-covered conditions (b,d,f) at Gothic (top row), Brush Creek (middle row), and Roaring Judy (bottom row). The thermodynamic profiles are retrieved with TROPoe.

465 The composite temperature profiles nicely show the much colder temperatures un-
 466 der snow-covered conditions (Fig. 6). The stratification in the valley was strongly stable
 467 at all sites during the night, independent of snow cover. A surface inversion started
 468 forming in the late afternoon indicated by an increase in the low-level temperature gra-
 469 dient (Fig. 5c,d). After the initial increase, the temperature gradients were nearly con-
 470 stant throughout the night and similar at all sites with values larger by approximately
 471 1-2 °C 100 m⁻¹ during the snow-covered regime. Under snow-free conditions, the inver-
 472 sion deepened gradually with time at all sites (Figs. 5e, 6a,c,e) with the strongest in-
 473 crease occurring during the first half of the night. After the initial growth, the inversion
 474 was quite stationary and very similar at all sites with respect to mean sea level indicat-
 475 ing that a layered cold pool formed in the East River Valley with the coldest air accu-
 476 mulating at the lowest parts of the valley. Under snow-covered conditions, no gradual
 477 increase in inversion depth was detected at any of the sites at the beginning of the night,
 478 but immediately occurred at around 3200 m MSL on the average (Fig. 5f). During its
 479 stationary phase, the inversion height was between around 3200 and 3700 m MSL which
 480 roughly coincided with ridge heights in the area (Fig. 1b,d). The temporal evolution of
 481 the low-level inversion is well reflected in the heat deficit with values increasing grad-
 482 ually during the night (Fig. 5i,j). Heat deficit values are largest at Roaring Judy, because
 483 this is the lowest altitude site and the inversion depth is largest and strongest here tem-
 484 perature increasing by 10 °C under snow-free conditions and 15 °C under snow-covered
 485 conditions from the surface to the top of the inversion (Fig. 6e,f).

486 Distinct differences in ABL structure are visible during daytime depending on snow
 487 cover. Under snow-free conditions, a well-mixed CBL developed equally at all sites af-
 488 ter sunrise reaching maximum depths of around 800 to 1000 m (Fig. 5g). It eroded the
 489 nocturnal temperature inversion in the valley (Fig. 6a,c,e) and resulted in near-zero heat
 490 deficit values in the afternoon (Fig. 5i). On the contrary, a very shallow CBL of less than
 491 150 m depth developed under snow-covered conditions Fig. 5h). Above the CBL, the val-
 492 ley atmosphere remained strongly stably stratified (Fig. 6b,d,f) causing the high heat
 493 deficit values during the day (Fig. 5j). This also explains why no gradual increase in in-
 494 version depth was detected at the beginning of the night (Fig. 5f). The thermal struc-
 495 ture of the ABL in the East River Valley under snow-covered conditions is very similar
 496 to the one found during wintertime in Alpine Valleys near Grenoble in the French Alps
 497 (Largeron & Staquet, 2016b, 2016a).

498 Even though the CBL was very shallow (Fig. 5h) and most of the valley atmosphere
 499 remained stably stratified during daytime (Fig. 6b,d,f), the heat deficit still decreased
 500 under snow-covered conditions (Fig. 5j). This can be related to a warming of the sta-
 501 bly stratified valley atmosphere up to around 4000 m MSL (Fig. 6b,d,f) associated with
 502 a descent of the inversion top. This warming can be attributed to subsidence heating when
 503 the core of the valley subsides compensating for upslope flows carrying mass up the side-
 504 walls (Whiteman, 1982). The inversion breakup mechanisms we found in the East River
 505 Valley, namely the upward growth of a CBL under snow-free conditions and the subsi-
 506 dence heating under snow-covered conditions, are consistent with the mechanisms pro-
 507 posed by Whiteman (1982). While we did not find observational evidence for a descend-
 508 ing top of the inversion under snow-free conditions, it may exist, but might not be de-
 509 tectable due to the coarse vertical resolution of the retrieved profiles and the retrieval's
 510 inability to detect sharp elevated inversions (Djalalova et al., 2022). Unfortunately, no
 511 radio soundings were available during daytime to further investigate this.

512 4 Representation of the ABL in the HRRR model

513 4.1 Temperature errors

514 To evaluate the representation of the thermal ABL structure in the HRRR model,
 515 we computed 24-h mean composites of bias (Eq. 1) and MAE (Eq. 2) of 2-m temper-

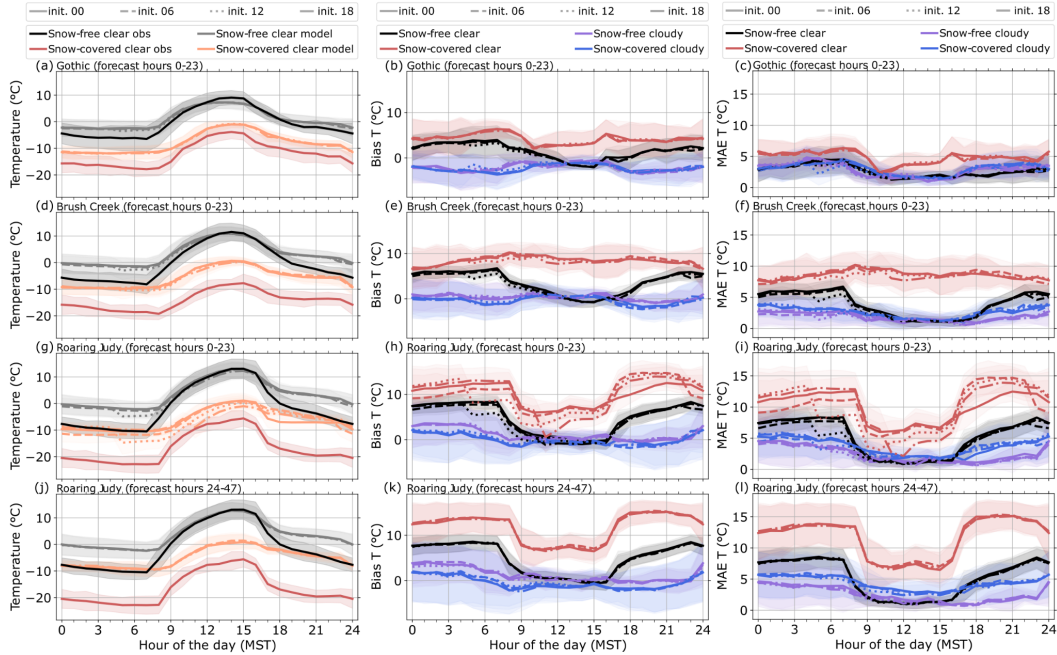


Figure 7. 24-h mean composites of (a,d,g,j) observed and simulated 2-m temperature and (b,e,h,k) bias and (c,f,i,l) mean absolute error (MAE) between simulated and observed 2-m temperature (model - observations) at Gothic, Brush Creek and Roaring Judy for clear-sky days under snow-free and snow-covered conditions. (a-i) show data from forecast hours 0-23 and (j-l) from forecast hours 24-47. The line style indicates different initialisation times (init.). Bias and MAE are additionally shown for cloudy days. The shading indicates the standard deviation.

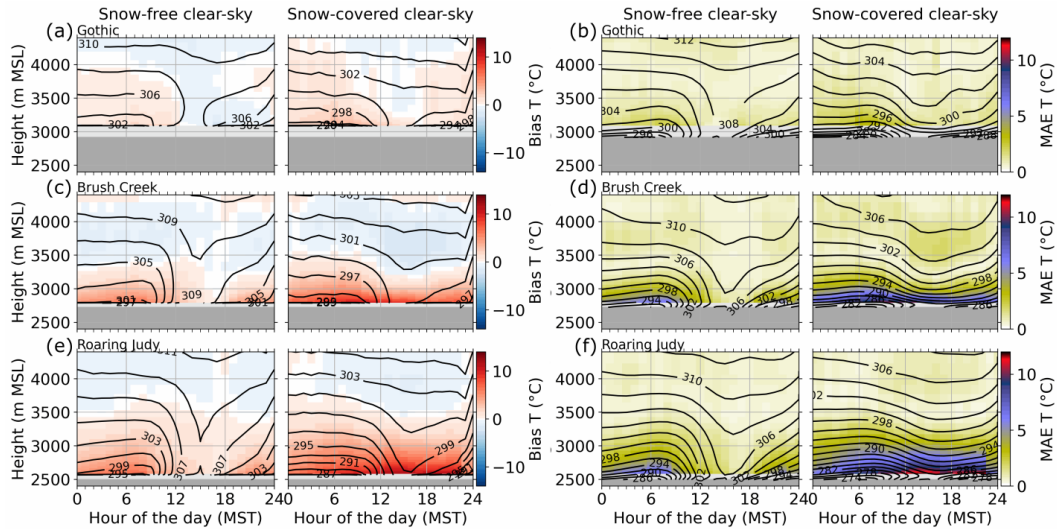


Figure 8. 24-h mean composites of (a,c,e) bias and (b,d,f) mean absolute error (MAE) profiles between simulated and observed temperature (model - observations) at Gothic, Brush Creek, and Roaring Judy for clear-sky days under snow-free and snow-covered conditions. The black iso-lines are 24-h mean composites of potential temperature simulated with the HRRR model (a,c,e) and retrieved with TROPoe (b,d,f). Model data for forecast hours 0-23 initialized at 6 UTC are shown. The dark grey shading indicates real world station height.

516 ature at Roaring Judy, Brush Creek, and Gothic (Fig. 7). On clear-sky days, the errors
 517 showed a diurnal cycle with lower values during the day and larger values during the night,
 518 except for Gothic. The errors were generally largest under snow-covered conditions. Model
 519 performance was worst at Roaring Judy with an average bias of up to 13 °C (Fig. 7h)
 520 and a MAE of up to 15 °C (Fig. 7i) during the night. The temporal evolution and mag-
 521 nitude of the errors at Gothic and Brush Creek were very similar for all initialization times
 522 (Fig. 7b,c,e,f). At Roaring Judy, however, the errors at a certain time of the day clearly
 523 depended on initialization time (Fig. 7h,i). The errors were generally lowest at the time
 524 of initialization and increased with forecast hour, as e.g. visible in the drops at 5, 11, and
 525 23 MST under snow-covered conditions. For longer forecast hours (24-47 hours) the er-
 526 rors did not depend any more on initialization time, but were equally high and showed
 527 the same diurnal cycle (shown for Roaring Judy in Fig. 7j,k,l). Maximum errors for longer
 528 forecast hours were also not markedly higher than for the configurations using the first
 529 24 forecast hours. This indicates that the time of initialization does not matter equally
 530 for all sites and that the model does not introduce ever growing errors with forecast length.
 531 Observed and simulated 2-m temperature indicates that nighttime cooling in the model,
 532 especially at the beginning of the night, is largely underestimated (Fig. 7a,d,g). After
 533 sunrise, the observed 2-m temperature increased more than the simulated one leading
 534 to a reduction in model errors, best visible at Roaring Judy. For comparison, we also com-
 535 puted the errors for cloudy days (indicated by blue and purple shading in Fig. 3). Bi-
 536 ases for these days were near 0 °C or slightly negative and MAE was usually less than
 537 5 °C, that is, much smaller than during clear-sky days.

538 The findings derived from the 2-m temperature errors generally hold for the tem-
 539 perature profiles as well. Figure 8 shows 24-hr mean composite profiles of bias and MAE
 540 as well as observed and simulated potential temperature isolines. The errors are com-
 541 puted with respect to mean sea level. Because terrain height at the individual sites was
 542 higher in the model than in the observations (Fig. 1d), the distance to the ground at a
 543 certain height was larger in the observations than in the model. In the presence of tem-
 544 perature inversions, computing the error profiles with respect to ground level would only
 545 lead to even larger MAE and positive biases than the ones shown in Fig. 8. Errors dur-
 546 ing clear-sky days were largest at lower altitude stations and increased towards the ground.
 547 This was clearly related to the failure of the model to correctly forecast the thermal strat-
 548 ification. Comparing observed (isolines in Fig. 8b,d,f) and simulated (isolines in Fig. 8a,c,e)
 549 potential temperature profiles revealed that the nocturnal strong surface inversions present
 550 in the observations at all sites independent of snow-cover were largely missing in the model.
 551 This has been identified as a common problem in NWP models (Zhong & Chow, 2013).
 552 Because the observed inversion was deepest and strongest at the lowest altitude site Roar-
 553 ing Judy (Fig. 8f), the impact of the erroneous stratification in the model was most pro-
 554 nounced here explaining the largest errors at this site (Figs. 7h,i and 8e,f). Under snow-
 555 free conditions, the warm bias and large MAE present during the night were much re-
 556 duced or even absent during daytime with the formation of a well-mixed CBL in both
 557 the model and the observations. While in the observations a strongly stably stratified
 558 layer persisted above the shallow CBL during the day under snow-covered conditions (iso-
 559 lines in Fig. 8b,d,f), the valley atmosphere was only weakly stably stratified in the model
 560 (isolines in Fig. 8a,c,e) resulting in large model errors also during daytime.

561 4.2 Possible reasons for model errors during clear-sky days

562 The smaller model errors during cloudy days suggest that the errors during clear-
 563 sky days are related to one or more physical processes which are only present or most
 564 pronounced during clear-sky days and which are not correctly represented in the model.
 565 This could be thermally driven flows such as slope and valley winds which form and are
 566 most pronounced during clear-sky days. Another possible reason could be errors in the
 567 surface radiation budget.

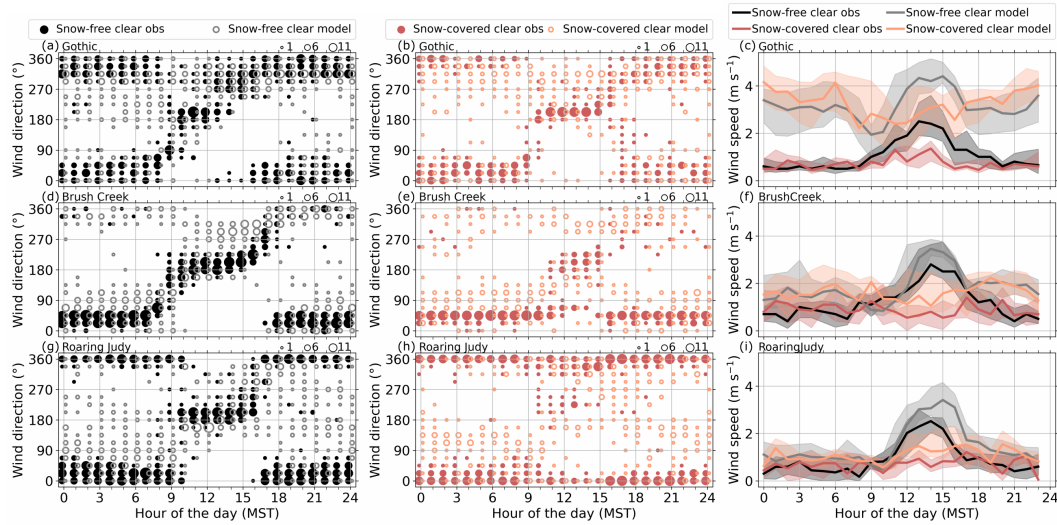


Figure 9. 24-h composites of observed and simulated near-surface (a,b,d,e,g,h) wind direction and (c,f,i) mean (solid line) wind speed at Gothic, Brush Creek and Roaring Judy for clear-sky and cloudy days under snow-free and snow-covered conditions. Model data from forecast hours 0-23 are shown. For wind direction, the marker size indicates how often a specific wind direction occurs at each time stamp using bins of 22.5 degree width. Model data for forecast hours 0-23 initialized at 6 UTC are shown. The shading in (c,f,i) indicates the standard deviation.

568

4.2.1 Thermally driven flows

569

570

571

572

573

574

575

576

577

578

579

580

581

582

583

We start with investigating the thermally driven flows by computing 24-h composites of near-surface wind speed and direction for clear-sky days (Fig. 9). Preferred wind directions are clearly visible in the observations at all three sites independent of snow cover. At Gothic, northwesterly to northeasterly flow prevailed during the night. Northwesterly flow indicates drainage along the main valley axis, while north-easterly flow was likely related to drainage outflow from a small tributary located to the north-east of Gothic (Fig. 1b). At Brush Creek and Roaring Judy, distinct downvalley wind along the main valley axis (oriented in north-easterly and northerly direction, respectively) dominated during the night. Southerly upvalley wind developed during daytime at all sites. It was more pronounced and lasted longer under snow-free conditions. When the ground was snow-covered, a shift to upvalley wind during daytime was not always observed on every day, especially at Roaring Judy and Brush Creek where downvalley wind sometimes persisted throughout the day. This lack of an upvalley wind during daytime is a common feature over glaciers or in snow-covered valleys (e.g. Obleitner, 1994; Whiteman, 2000; Song et al., 2007; Zardi & Whiteman, 2013).

584

585

586

587

588

589

590

591

592

593

Valley winds are driven by a horizontal pressure gradient along the valley axis which develops as a function of height between air columns with different vertical temperature structures in different sections of the valley (Zardi & Whiteman, 2013). During the day, the pressure at a given height is generally lower further up the valley causing an upvalley wind and vice versa during the night. The relationship between pressure difference and valley wind under clear-sky days was for example confirmed in the Inn Valley in Austria (Lehner et al., 2019) and the Adige Valley in Italy (Giovannini et al., 2017). We computed the horizontal pressure difference between Roaring Judy and Gothic after reducing the pressure at Roaring Judy to the altitude of Gothic for clear-sky days. Under snow-free conditions, we found a diurnal cycle of the pressure difference with Gothic having

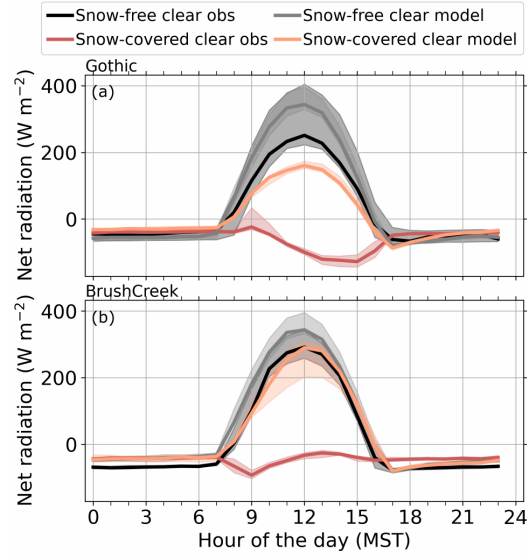


Figure 10. 24-h mean composites of observed and simulated net radiation at Gothic and Brush Creek for clear-sky days under snow-free and snow-covered conditions. Model data for forecast hours 0-23 initialized at 6 UTC are shown. The shading indicates the standard deviation.

594 lower pressure during the day and higher pressure during the night (not shown) which
 595 is consistent with the diurnal cycle in wind direction (Fig. 9a,d,g). Under snow-covered
 596 conditions, hardly any diurnal cycle in pressure difference was distinguishable which again
 597 agrees with the less distinct diurnal cycle in wind direction (Fig. 9b,e,f).

598 With the coarse model resolution, the fine-scale structure of the valley, such as the
 599 small tributary north-east of Gothic, is not resolved (Fig. 1c) and we did not expect the
 600 model to get all the details of the observed thermally driven flows right. Nevertheless,
 601 we were surprised by the absence of valley winds in the model data (Fig. 9). Wind di-
 602 rection was much more scattered than in the observations at all sites independent of snow-
 603 cover and a clear diurnal cycle was missing. The overestimation of near-surface horizon-
 604 tal wind speed especially visible at Gothic, may be an indication that stronger upper-
 605 level wind was able to penetrate into the weakly stably stratified valley atmosphere. The
 606 failure of the model to correctly simulate the nighttime drainage flows provides a possi-
 607 ble explanation for the large errors in the ABL thermal structure (Sect. 4.1). Drainage
 608 flows transport cold high-density air that forms near the surface due to radiative cool-
 609 ing from higher parts of the valley to lower parts which leads to the accumulation of cold
 610 air on the valley floor and the buildup of a temperature inversion. The wind and tem-
 611 perature observations provide strong evidence that this was the main process responsi-
 612 ble for the formation of the observed strong nocturnal inversions. We hypothesize that
 613 because drainage flows were largely missing in the model (Fig. 9), no strong nocturnal
 614 inversions could form and they were easily mixed out during daytime (Fig. 8). In par-
 615 ticular under snow-covered conditions, this could lead to the very large errors in the layer
 616 where the stable stratification was maintained in the observations.

617 4.2.2 Surface radiation budget

618 An underprediction of radiative cooling at night could add to the warm nighttime
 619 biases. We therefore computed 24-h median composites of observed and simulated net

620 radiation under both snow-cover conditions at Gothic and Brush Creek (Fig. 10). No
621 radiation measurements were available at Roaring Judy. Nighttime net radiation was neg-
622 ative and on the same order of magnitude in both the model and the observations, rul-
623 ing out errors in the surface radiation budget as a relevant reason for the warm surface
624 air temperature biases and too weak nighttime inversions in the model.

625 In contrast to nighttime, huge differences in net radiation are visible during day-
626 time under snow-covered conditions. We found that this is largely related to an under-
627 prediction of albedo in the model over snow-covered ground, which was less than 0.55
628 in the model compared to more than 0.9 in the observations (Fig. 3e). While snow was
629 present in the whole valley during the snow-covered regime as evident from satellite ob-
630 servations, snow frequently melted during daytime in the 24-h forecasts in the lower parts
631 of the valley where simulated snow depth was lower. This indicates weaknesses in sim-
632 ulated snow-melting rates. The HRRR did not show a dry bias with respect to 2-m wa-
633 ter vapor mixing ratio in the lower part of the valley (not shown). The warm bias, how-
634 ever, led to an underestimation of 2-m relative humidity which could enhance snow melt.
635 The HRRR model uses the Rapid Update Cycle (RUC) LSM in which snow albedo de-
636 pends on vegetation type, snow age, snow depth, snow cover, and snow temperature (Smirnova
637 et al., 2016). Reasons for the erroneous representation of albedo and snow cover might
638 be related to the missing representation of subgrid variability of snow in the current RUC
639 LSM (He et al., 2021), biases introduced by the current data assimilation system (Benjamin
640 et al., 2022; Dowell et al., 2022), or other potential errors in the physics parameteriza-
641 tions. He et al. (2021) showed that estimates of snow cover fraction are improved and
642 surface heat fluxes are more realistic when coupling a stochastic snow model to the RUC
643 LSM to represent the subgrid variability of snow. Modifications to both the land and
644 atmospheric data assimilation system and to the RUC LSM will be addressed by the new
645 Rapid Refresh Forecast System (RRFS), which is currently under development as part
646 of NOAA’s Unified Forecast System. It is expected that the RRFS will become the op-
647 erational 3-km grid model, replacing the HRRR, in 2024.

648 Even though albedo differences are large and likely have implications for the land-
649 atmosphere exchange during daytime and may contribute to the mix out of the simu-
650 lated nighttime inversion, we do not think that they are the main reason for the large
651 temperature errors. Instead we suspect the missing drainage flows. In a future study,
652 we plan to run a nested simulation with smaller horizontal grid spacing to test if higher
653 horizontal resolution allows to better simulate the thermally driven circulations in the
654 East River Valley.

655 5 Summary and conclusions

656 In this study, we analyzed the response of the ABL to changes in the surface en-
657 ergy balance on clear-sky days during the seasonal transition from snow-free to snow-
658 covered ground in the East River Valley near Crested Butte in Colorado’s Rocky Moun-
659 tains over a three-month period from October 2021 to January 2022. The simultaneous
660 deployment of three infrared spectrometers provided a unique opportunity to study the
661 thermal structure of the valley ABL. Temperature profiles were obtained from infrared
662 spectrometer radiances using the optimal estimation physical retrieval TROPoe. We fur-
663 ther evaluated NOAA’s operational HRRR model with the observations to assess how
664 well the model captures primary ABL characteristics under different snow-cover condi-
665 tions.

666 The three-month observation period can roughly be divided in half, with mostly
667 snow-free conditions during the first 6 weeks and snow-covered conditions after a multi-
668 day snowfall event at the beginning of December. The changes in snow cover were as-
669 sociated with changes in observed surface albedo which increased from less than 0.3 to
670 more than 0.9. Under snow-covered conditions, daily mean net radiation was directed

671 upwards from the surface indicating radiative cooling, sensible heat flux was directed down-
672 wards in turn compensating for some of the radiative cooling, and daily minimum and
673 maximum 2-m air temperature values dropped with maximum values usually below freez-
674 ing. Strong diurnal cycles in low-level air temperature were observed on clear-sky days
675 throughout the whole period with the formation of a daytime CBL and a nocturnal sur-
676 face inversion, which was strongest and deepest at the Roaring Judy site, located fur-
677 thest down the valley. After an initial growth phase, the top of the inversion with respect
678 to sea level was roughly the same at all three sites, indicating that a layered cold air pool
679 filled the whole valley during nighttime. While the stable stratification in the valley was
680 mostly mixed out during the day under snow-free conditions, a persistent inversion was
681 present above a very shallow CBL under snow-covered conditions.

682 The HRRR model showed a large nocturnal warm bias in the ABL on clear-sky days
683 (up to 13 °C at 2 m AGL under snow-covered conditions), because the model failed to
684 form strong nocturnal inversions. The errors decreased with formation of the CBL dur-
685 ing daytime. Unlike in the observations, where an inversion persisted above a very shal-
686 low CBL during the day under snow-covered conditions, much weaker simulated night-
687 time inversions were mostly mixed out, leading to large warm biases above the observed
688 CBL in the valley atmosphere during daytime. The model errors were much smaller on
689 cloudy days. We assert the main reason for the large temperature errors is a failure of
690 the model to correctly simulate the thermally driven flows in the East River Valley. While
691 nighttime drainage flows are a very clear and persistent feature in the observations, they
692 are largely missing in the simulations. A future study will use a higher-resolution sim-
693 ulation to investigate if that inability of the HRRR to simulate the thermally driven flow
694 was due to its 3-km grid spacing.

695 We showed that with careful processing, temperature profiles retrieved with TROPoe
696 from ground-based passive remote sensing infrared spectrometers are suited to study the
697 ABL evolution in complex terrain. With a temporal resolution of minutes, these retrievals
698 are able to resolve diurnal changes in stratification under different snow-cover conditions.
699 While we focused on clear-sky days only, temperature profiles can also be retrieved un-
700 der cloud base and the response of lower tropospheric stability and subsequent surface
701 energy fluxes to radiatively clear and cloudy conditions is the subject of another study
702 (Sedlar et al. (n.d.)). The ABL plays a crucial role in the temporal evolution of seasonal
703 snow cover, particularly during spring snowmelt. The continuous temperature profiles
704 retrieved with TROPoe can provide invaluable information on the ABL thermal struc-
705 ture during the seasonal changes.

706 Retrieved temperature profiles proved further to be very useful for the model eval-
707 uation of ABL structure and stratification. From near-surface measurements alone we
708 would not have been able to identify the problems the model has with simulating inver-
709 sion strength and with maintaining the persistent inversion during daytime. The chal-
710 lenges faced by the model to correctly form and maintain inversions under snow-covered
711 conditions can, for example, have implications for air quality forecasts in mountainous
712 terrain.

713 **Open Research Section**

714 Measurements at Gothic are part of the Atmospheric Radiation Measurement (ARM)
715 Mobile Facility (AMF2). The used data at Gothic are AERI radiances (Gero et al., 2021),
716 radiosonde profiles (Burk, 2021), ceilometer cloud base height (Morris et al., 2021), ra-
717 diation flux components (Shi, 2021b, 2021a), sensible heat flux (Sullivan et al., 2021),
718 near-surface meteorological standard measurements (Keeler et al., 2021), and precipi-
719 tation measurements (Cromwell & Bartholomew, 2021). NOAA Global Monitoring Lab-
720 oratory conducted the ceilometer (NOAA Global Monitoring Laboratory, 2021b) and ra-
721 diation (NOAA Global Monitoring Laboratory, 2021c) measurements at Kettle Ponds

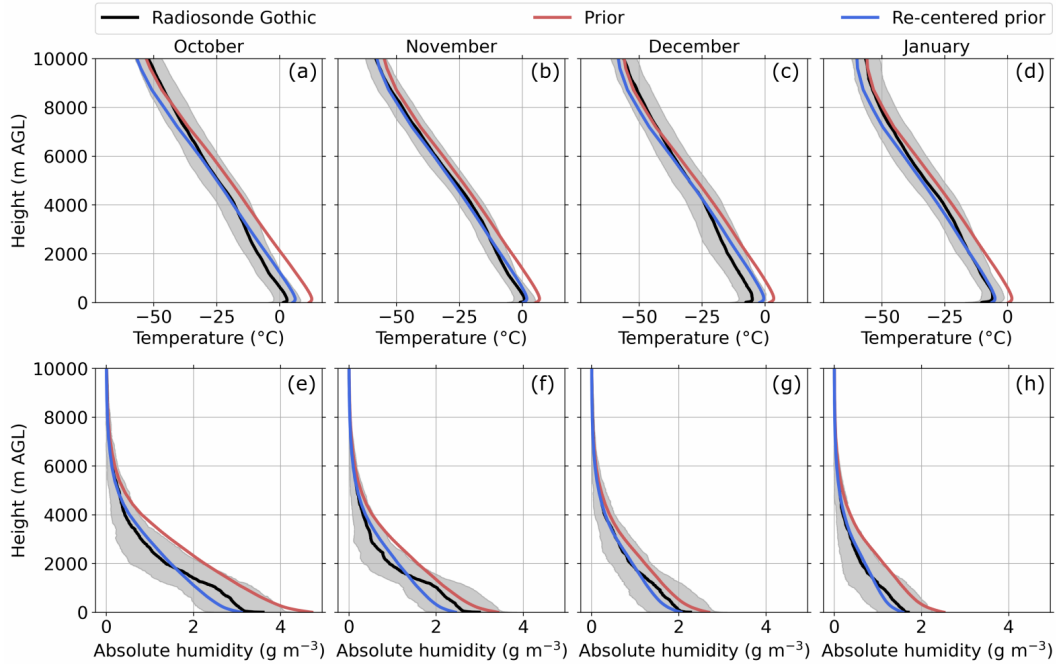


Figure A1. Monthly profiles of (a-d) temperature and (e-h) absolute humidity. The twice daily radiosonde launches at Gothic are averaged for each month with the shading showing the standard deviation. The red line shows the climatological prior computed from radiosonde launches at Denver and the green line shows the profiles after the prior was re-centered using the monthly mean IWV values from the radio soundings at Gothic.

722 and the ceilometer (NOAA Global Monitoring Laboratory, 2021a) and radiation (NOAA
 723 Global Monitoring Laboratory, 2021d) measurements at Brush Creek. NOAA Air Re-
 724 sources Laboratory provided sensible heat flux measurements at Brush Creek. NOAA
 725 Physical Science Laboratory conducted the Atmospheric Surface Flux Stations (ASFS)
 726 measurements at Avery Picnic and Kettle Ponds (NOAA Physical Science Laboratory,
 727 2021a), and surface meteorology (NOAA Physical Science Laboratory, 2021c), ASSIST
 728 (Adler, Bianco, Djalalova, Myers, & Wilczak, 2022), and ceilometer (Adler, Bianco, Djalalova,
 729 Myers, Pezoa, et al., 2022) measurements at Roaring Judy. The AERI data at Brush Creek
 730 (NOAA National Severe Storms Laboratory, 2021) were collected as part of the Collab-
 731 orative Lower Atmospheric Profiling System (CLAMPS) by NOAA National Severe Storms
 732 Laboratory.

733 Appendix A Re-centering of the prior

734 Although radiosondes are launched twice daily at the AMF2 at Gothic, the num-
 735 ber of these soundings is not enough to compute the level-to-level covariance for the 110-
 736 element state vector of the prior needed for the TROPoe retrievals. Instead, we computed
 737 monthly priors using the operational radio soundings launched at Denver, CO, just east
 738 of the Rocky Mountains. Although the horizontal distance between the East River Val-
 739 ley and the launch site at Denver is only around 220 km, the elevation difference is 1300
 740 m and the atmospheric conditions can be quite different between the central Rocky Moun-
 741 tains and Denver. To account for differences in the integrated water vapor (IWV) in the
 742 atmospheric column due to the elevation difference and to avoid systematic offsets in the
 743 prior, we re-centered the mean prior profiles while preserving the relative humidity pro-

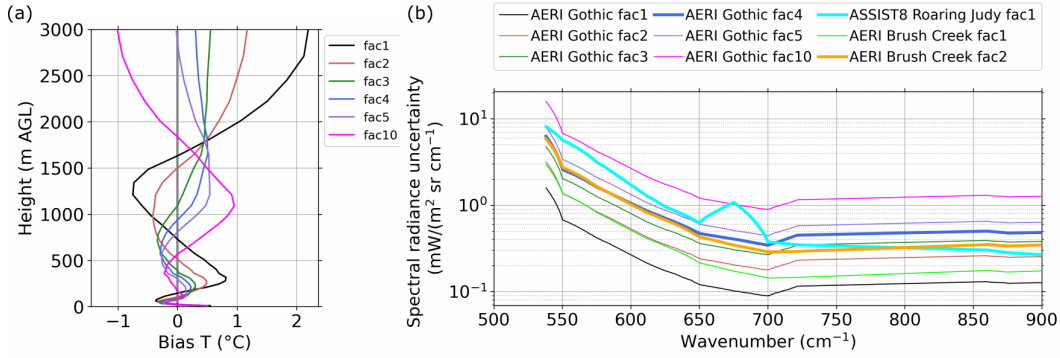


Figure B1. (a) Mean bias between the temperature profiles retrieved with TROPoe for the AERI at Gothic and colocated radio soundings (retrieved profile - radiosonde profile). (b) Mean spectral radiance uncertainty for the AERIs at Gothic and Brush Creek and the ASSIST at Roaring Judy. fac1 indicates that the original uncertainty radiance was used, fac2, fac3, fac4, fac5, and fac10 indicates that the uncertainty radiance was multiplied with a factor of 2, 3, 4, 5, and 10, respectively.

744 files. We borrowed the concept of recentering from the data assimilation community (e.g.
 745 Wang et al., 2013), as TROPoe essentially is a 1-dimensional data assimilation frame-
 746 work. We computed the ratio of the monthly mean IWV from radio soundings at Gothic
 747 and the mean IWV of the prior and multiplied the prior mixing ratio profile by this fac-
 748 tor. We then adjusted the temperature profile to preserve the relative humidity from the
 749 original prior. The re-centered monthly mean prior profiles agreed very well with monthly
 750 mean radiosonde profiles at Gothic (Fig. A1).

751 Appendix B AERI noise modification for TROPoe

752 The radiance uncertainty of the ARM AERI at Gothic and the CLAMPS AERI
 753 at Brush Creek was not large enough to compensate for the missing uncertainty of the
 754 forward model in TROPoe which led to unrealistic profiles at Brush Creek and Gothic
 755 (temperature inversion always between about 1500 and 2000 m AGL), which indicated
 756 an overfitting of the temperature profiles. Figure B1b indicates that the noise of the AERI
 757 at Gothic is about a factor of 4 smaller and the noise of the AERI at Brush Creek is about
 758 a factor of 2 smaller than the noise of the ASSIST at Roaring Judy. We ran the retrieval
 759 for the AERI at Gothic at the time of the radiosonde launches, i.e. at 0 and 12 UTC,
 760 for the whole investigation period (92 profiles) and computed the mean differences be-
 761 tween the temperature profiles (black line in Fig. B1a). Large differences are visible
 762 with a warm bias below around 750 m AGL, a cold bias between 750 m and 1600 m AGL,
 763 and a strong warm bias above 1600 m AGL, which is consistent with the unrealistic temper-
 764 ature inversion in the retrieved temperature profiles.

765 We then systematically increased the noise of the AERI at Gothic by multiplying
 766 the spectral radiance uncertainties by the factors 2, 3, 4, 5, and 10 and ran TROPoe with
 767 each increased noise level. The spectral radiance uncertainties for the different config-
 768 urations are shown in Fig. B1b and the resulting temperature bias profiles are shown in
 769 Fig. B1a. We decided to use a factor 4 for the AERI at Gothic because (i) the radiance
 770 uncertainty was then the same order of magnitude as the ASSIST and (ii) the warm bias
 771 above around 1600 m AGL and the cold bias below were much reduced. Even though
 772 no radiosonde profiles were available to compare to the retrieved profiles at Brush Creek,

773 we decided to increase the radiance uncertainty for the AERI there by a factor of 2 to
774 have similar uncertainty radiance values for all three infrared radiometers.

775 Acknowledgments

776 We thank all of the individuals, in particular Rocky Mountain Biological Laboratory (RMBL),
777 for help with the SPLASH site selection, leases, instrument deployment and maintenance,
778 data collection, and data quality control. Funding for this work was provided by the NOAA
779 Physical Sciences Laboratory, the U.S. Department of Energy (DOE) Office of Energy
780 Efficiency and Renewable Energy, Wind Energy Technologies Office, and by the NOAA
781 Atmospheric Science for Renewable Energy program. This work was supported by NOAA
782 cooperative agreements NA17OAR4320101 and NA22OAR4320151.

783 References

- 784 Adler, B., Bianco, L., Djalalova, I., Myers, T., Pezoa, S., Bariteau, L., & Wilczak, J.
785 (2022). *NOAA PSL CL31 Ceilometer Backscatter and Cloud Base Height Data*
786 *for SPLASH* [dataset]. Zenodo. doi: 10.5281/zenodo.7438524
- 787 Adler, B., Bianco, L., Djalalova, I., Myers, T., & Wilczak, J. (2022). *NOAA PSL*
788 *thermodynamic profiles retrieved from ASSIST infrared radiances with the opti-*
789 *mal estimation physical retrieval TROPoe during SPLASH* [dataset]. Zenodo.
790 doi: 10.5281/zenodo.7435060
- 791 Adler, B., Gohm, A., Kalthoff, N., Babić, N., Corsmeier, U., Lehner, M., ... Geor-
792 gousis, G. (2021). CROSSINN: a field experiment to study the three-
793 dimensional flow structure in the Inn Valley, Austria. *Bull. Amer. Meteor.*
794 *Soc.*, 102(1), E38–E60. doi: 10.1175/BAMS-D-19-0283.1
- 795 Adler, B., & Kalthoff, N. (2014). Multi-scale transport processes observed in the
796 boundary layer over a mountainous island. *Boundary-Layer Meteorol.*, 153,
797 515–537. doi: 10.1007/s10546-014-9957-8
- 798 Adler, B., Wilczak, J. M., Bianco, L., Djalalova, I., Duncan Jr, J. B., & Turner,
799 D. D. (2021). Observational case study of a persistent cold pool and gap flow
800 in the Columbia River Basin. *J. Appl. Meteor. Climatol.*, 60(8), 1071–1090.
801 doi: 10.1175/JAMC-D-21-0013.1
- 802 Adler, B., Wilczak, J. M., Kenyon, J., Bianco, L., Djalalova, I. V., Olson, J. B., &
803 Turner, D. D. (2022). Evaluation of a cloudy cold-air pool in the Columbia
804 River Basin in different versions of the HRRR model. *EGUsphere*, 2022, 1–32.
805 doi: 10.5194/egusphere-2022-355
- 806 Benjamin, S. G., Smirnova, T. G., James, E. P., Lin, L.-F., Hu, M., Turner, D. D.,
807 & He, S. (2022). Land–snow data assimilation including a moderately coupled
808 initialization method applied to NWP. *J. Hydrometeorol.*, 23(6), 825–845. doi:
809 10.1175/JHM-D-21-0198.1
- 810 Benjamin, S. G., Weygandt, S. S., Brown, J. M., Hu, M., Alexander, C. R.,
811 Smirnova, T. G., ... others (2016). A North American hourly assimilation
812 and model forecast cycle: The Rapid Refresh. *Mon. Wea. Rev.*, 144(4), 1669–
813 1694. doi: 10.1175/MWR-D-15-0242.1
- 814 Burk, K. (2021). *Balloon-Borne Sounding System (SONDEWNP)*. doi: 10.5439/
815 1595321
- 816 Butterworth, B. J., Desai, A. R., Townsend, P. A., Petty, G. W., Andresen, C. G.,
817 Bertram, T. H., ... others (2021). Connecting land–atmosphere interactions to
818 surface heterogeneity in CHEESEHEAD19. *Bull. Amer. Meteor. Soc.*, 102(2),
819 E421–E445. doi: 10.1175/BAMS-D-19-0346.1
- 820 Chemel, C., Arduini, G., Staquet, C., Llargeron, Y., Legain, D., Tzanos, D., & Paci,
821 A. (2016). Valley heat deficit as a bulk measure of wintertime particulate
822 air pollution in the Arve River Valley. *Atmos. Env.*, 128, 208–215. doi:
823 10.1016/j.atmosenv.2015.12.058

- 824 Clough, S. A., & Iacono, M. J. (1995). Line-by-line calculation of atmospheric fluxes
825 and cooling rates: 2. application to carbon dioxide, ozone, methane, nitrous
826 oxide and the halocarbons. *J. Geophys. Res.: Atmos.*, *100*(D8), 16519–16535.
827 doi: 10.1029/95JD01386
- 828 Clough, S. A., Shephard, M. W., Mlawer, E. J., Delamere, J. S., Iacono, M. J.,
829 Cady-Pereira, K., . . . Brown, P. D. (2005, March). Atmospheric radiative
830 transfer modeling: a summary of the AER codes. *J. Quant. Spectrosc. Radiat.*
831 *Transf.*, *91*(2), 233–244. doi: 10.1016/j.jqsrt.2004.05.058
- 832 Cox, C. J., Gallagher, M., Shupe, M., Persson, P., Solomon, A., Ayers, T., . . . Ut-
833 tal, T. (2023). Continuous observations of the surface energy budget and
834 meteorology over arctic sea ice during mosaic. *Nature Scientific Data, to be*
835 *submitted*.
- 836 Cromwell, E., & Bartholomew, M. (2021). *Weighing Bucket Precipitation Gauge*
837 *(WBPLUVIO2)*. doi: 10.5439/1338194
- 838 Cullen, N. J., & Conway, J. P. (2015). A 22 month record of surface meteorology
839 and energy balance from the ablation zone of Brewster Glacier, New Zealand.
840 *J. Glaciol.*, *61*(229), 931–946. doi: 10.3189/2015JoG15J004
- 841 Djalalova, I. V., Turner, D. D., Bianco, L., Wilczak, J. M., Duncan, J., Adler,
842 B., & Gottas, D. (2022, January). Improving thermodynamic profile re-
843 trievals from microwave radiometers by including radio acoustic sounding
844 system (RASS) observations. *Atmos. Meas. Tech.*, *15*(2), 521–537. doi:
845 10.5194/amt-15-521-2022
- 846 Dowell, D. C., Alexander, C. R., James, E. P., Weygandt, S. S., Benjamin, S. G.,
847 Manikin, G. S., . . . Alcott, T. I. (2022). The High-Resolution Rapid Refresh
848 (HRRR): An hourly updating convection-allowing forecast model. part i: Mo-
849 tivation and system description. *Wea. Forecasting*, *37*(8), 1371 - 1395. doi:
850 10.1175/WAF-D-21-0151.1
- 851 Duncan Jr., J. B., Bianco, L., Adler, B., Bell, T., Djalalova, I. V., Riihimaki, L., . . .
852 Wilczak, J. M. (2022). Evaluating convective planetary boundary layer height
853 estimations resolved by both active and passive remote sensing instruments
854 during the CHEESEHEAD19 field campaign. *Atmos. Meas. Tech.*, *15*(8),
855 2479–2502. doi: 10.5194/amt-15-2479-2022
- 856 Feldman, D., Aiken, A., Boos, W., Carroll, R., Chandrasekar, V., Collins, W., . . .
857 Williams, K. (2021). *Surface atmosphere integrated field laboratory (sail)*
858 *science plan* (Tech. Rep. No. DOE/SC-ARM-21-004). ARM user facility.
- 859 Gero, J., Garcia, R., Hackel, D., Ermold, B., & Gaustad, K. (2021). *Atmospheric*
860 *Emitted Radiance Interferometer (AERICH1)*. (Date accessed: 2022-08-21)
861 doi: 10.5439/1025143
- 862 Giovannini, L., Laiti, L., Serafin, S., & Zardi, D. (2017). The thermally driven di-
863 urnal wind system of the Adige Valley in the Italian Alps. *Quart. J. Roy. Me-*
864 *teor. Soc.*, *143*(707), 2389–2402. doi: 10.1002/qj.3092
- 865 Hall, D. K., & Riggs, G. A. (2021). *MODIS/Terra Snow Cover Daily L3*
866 *Global 500m SIN Grid, Version 61*. NASA National Snow and Ice Data
867 Center Distributed Active Archive Center. Retrieved 2022-08-21, from
868 <https://nsidc.org/data/MOD10A1/versions/61> (Date accessed: 2022-
869 08-21) doi: 10.5067/MODIS/MOD10A1.061
- 870 He, S., Smirnova, T. G., & Benjamin, S. G. (2021). Single-Column validation of a
871 snow subgrid parameterization in the Rapid Update Cycle Land-Surface Model
872 (RUC LSM). *Water Resources Res.*, *57*(8). doi: 10.1029/2021WR029955
- 873 Herrera-Mejía, L., & Hoyos, C. D. (2019). Characterization of the atmospheric
874 boundary layer in a narrow tropical valley using remote-sensing and radiosonde
875 observations and the WRF model: the Aburrá Valley case-study. *Quart. J.*
876 *Roy. Meteor. Soc.*, *145*(723), 2641–2665. doi: 10.1002/qj.3583
- 877 Keeler, E., Kyröuac, J., & Ermold, B. (2021). *Automatic Weather Station (MAWS)*.
878 doi: 10.5439/1182027

- 879 Knuteson, R., Revercomb, H., Best, F., Ciganovich, N., Dedecker, R., Dirkx, T.,
880 ... others (2004a). Atmospheric emitted radiance interferometer. Part II:
881 Instrument performance. *J. Atmos. Oceanic Technol.*, *21*(12), 1777–1789. doi:
882 10.1175/JTECH-1663.1
- 883 Knuteson, R., Revercomb, H., Best, F., Ciganovich, N., Dedecker, R., Dirkx, T.,
884 ... others (2004b). Atmospheric emitted radiance interferometer. Part I:
885 Instrument design. *J. Atmos. Oceanic Technol.*, *21*(12), 1763–1776. doi:
886 10.1175/JTECH-1662.1
- 887 Lareau, N. P., Crosman, E., Whiteman, C. D., Horel, J. D., Hoch, S. W., Brown,
888 W. O., & Horst, T. W. (2013). The persistent cold-air pool study. *Bull. Amer.*
889 *Meteor. Soc.*, *94*(1), 51–63. doi: 10.1175/BAMS-D-11-00255.1
- 890 LARGERON, Y., & STAQUET, C. (2016a). The atmospheric boundary layer during win-
891 tertime persistent inversions in the Grenoble Valleys. *Front. Earth Sci.*, *4*. doi:
892 10.3389/feart.2016.00070
- 893 LARGERON, Y., & STAQUET, C. (2016b). Persistent inversion dynamics and wintertime
894 PM10 air pollution in Alpine valleys. *Atmos. Env.*, *135*, 92–108. doi: 10.1016/
895 j.atmosenv.2016.03.045
- 896 Lehner, M., Rotach, M. W., & Obleitner, F. (2019). A method to identify syn-
897 optically undisturbed, clear-sky conditions for valley-wind analysis. *Boundary-*
898 *Layer Meteorol.*, *173*(3), 435–450. doi: 10.1007/s10546-019-00471-2
- 899 McArthur, L. (2005). *World Climate Research Programme - Baseline Surface Radi-*
900 *ation Network (BSRN)-Operations Manual Version 2.1*. Experimental Studies
901 Division, Atmospheric Environment Service. Retrieved from [https://library](https://library.wmo.int/index.php?lvl=notice_display&id=11762)
902 [.wmo.int/index.php?lvl=notice_display&id=11762](https://library.wmo.int/index.php?lvl=notice_display&id=11762)
- 903 Morris, V., Zhang, D., & Ermold, B. (2021). *Ceilometer (ceil)*. doi: 10.5439/
904 1181954
- 905 Mott, R., Vionnet, V., & Grünewald, T. (2018). The seasonal snow cover dynam-
906 ics: review on wind-driven coupling processes. *Front. Earth Sci.*, *6*, 197. doi:
907 10.3389/feart.2018.00197
- 908 NOAA Global Monitoring Laboratory. (2021a). *Ceilometer CL51 Brush Creek*
909 [dataset]. Retrieved 2022-11-16, from [https://gml.noaa.gov/aftp/g-rad/](https://gml.noaa.gov/aftp/g-rad/surfrad/ceilometer/cl51_cloud_prod_lev0/cbc/)
910 [surfrad/ceilometer/cl51_cloud_prod_lev0/cbc/](https://gml.noaa.gov/aftp/g-rad/surfrad/ceilometer/cl51_cloud_prod_lev0/cbc/)
- 911 NOAA Global Monitoring Laboratory. (2021b). *Ceilometer CL51 Kettle Ponds*
912 [dataset]. Retrieved 2022-11-16, from [https://gml.noaa.gov/aftp/g-rad/](https://gml.noaa.gov/aftp/g-rad/surfrad/ceilometer/cl51_cloud_prod_lev0/ckp/)
913 [surfrad/ceilometer/cl51_cloud_prod_lev0/ckp/](https://gml.noaa.gov/aftp/g-rad/surfrad/ceilometer/cl51_cloud_prod_lev0/ckp/)
- 914 NOAA Global Monitoring Laboratory. (2021c). *Radiation and surface meteorological*
915 *station Brush Creek* [dataset]. Retrieved 2022-11-16, from [https://gml.noaa](https://gml.noaa.gov/aftp/data/radiation/campaigns/Format/ckp/)
916 [.gov/aftp/data/radiation/campaigns/Format/ckp/](https://gml.noaa.gov/aftp/data/radiation/campaigns/Format/ckp/)
- 917 NOAA Global Monitoring Laboratory. (2021d). *Radiation and surface meteorological*
918 *station Brush Creek* [dataset]. Retrieved 2022-11-16, from [https://gml.noaa](https://gml.noaa.gov/aftp/data/radiation/campaigns/Format/cbc/)
919 [.gov/aftp/data/radiation/campaigns/Format/cbc/](https://gml.noaa.gov/aftp/data/radiation/campaigns/Format/cbc/)
- 920 NOAA National Severe Storms Laboratory. (2021). *Collaborative Lower Atmo-*
921 *spheric Profiling System Brush Creek* [dataset]. Retrieved 2022-11-16, from
922 [https://data.nssl.noaa.gov/thredds/catalog/FRDD/CLAMPS/clamps/](https://data.nssl.noaa.gov/thredds/catalog/FRDD/CLAMPS/clamps/clamps2/ingested/catalog.html)
923 [clamps2/ingested/catalog.html](https://data.nssl.noaa.gov/thredds/catalog/FRDD/CLAMPS/clamps/clamps2/ingested/catalog.html)
- 924 NOAA Physical Science Laboratory. (2021a). *Atmospheric Surface Flux Statinos*
925 *(ASFS)* [dataset]. Retrieved 2022-11-16, from [ftp://ftp1.esrl.noaa.gov/](ftp://ftp1.esrl.noaa.gov/Observations/Campaigns/SPLASH/)
926 [Observations/Campaigns/SPLASH/](ftp://ftp1.esrl.noaa.gov/Observations/Campaigns/SPLASH/)
- 927 NOAA Physical Science Laboratory. (2021b). *SPLASH - Study of Precipitation,*
928 *the Lower Atmosphere, and Surface for Hydrometeorology* [website]. Retrieved
929 2022-08-04, from <https://psl.noaa.gov/splash/>
- 930 NOAA Physical Science Laboratory. (2021c). *Surface meteorological station Roaring*
931 *Judy* [dataset]. Retrieved 2022-11-16, from [https://psl.noaa.gov/data/obs/](https://psl.noaa.gov/data/obs/sites/view_site_details.php?siteID=rjy)
932 [sites/view_site_details.php?siteID=rjy](https://psl.noaa.gov/data/obs/sites/view_site_details.php?siteID=rjy)
- 933 Obleitner, F. (1994). Climatological features of glacier and valley winds at the

- 934 Hintereisferner (Ötztal Alps, Austria). *Theor. Appl. Climatol.*, 49(4), 225–239.
 935 Retrieved 2022-09-09, from <http://link.springer.com/10.1007/BF00867462>
 936 doi: 10.1007/BF00867462
- 937 Rochette, L., Smith, W. L., Howard, M., & Bratcher, T. (2009). ASSIST, Atmo-
 938 spheric Sounder Spectrometer for Infrared Spectral Technology: latest devel-
 939 opment and improvement in the atmospheric sounding technology. In *Imaging*
 940 *spectrometry xiv* (Vol. 7457, pp. 9–17). doi: 10.1117/12.829344
- 941 Sedlar, J., Meyers, T., Adler, B., & Cox, C. (n.d.). Low-level liquid-bearing clouds
 942 drive lower atmosphere stability and surface energy forcing over a seasonally
 943 snow-covered high-mountain watershed environment.
- 944 Sedlar, J., Riihimaki, L., Turner, D., Duncan, J., Adler, B., Bianco, L., . . . others
 945 (2022). Investigating the impacts of daytime boundary layer clouds on sur-
 946 face energy fluxes and boundary layer structure during CHEESEHEAD19. *J.*
 947 *Geophys. Res.*, 127(5), e2021JD036060. doi: 10.1029/2021JD036060
- 948 Seibert, P., Beyrich, F., Gryning, S.-E., Joffre, S., Rasmussen, A., & Tercier, P.
 949 (2000). Review and intercomparison of operational methods for the de-
 950 termination of the mixing height. *Atmos. Env.*, 34(7), 1001–1027. doi:
 951 10.1016/S1352-2310(99)00349-0
- 952 Serafin, S., Adler, B., Cuxart, J., De Wekker, S., Gohm, A., Grisogono, B., . . . oth-
 953 ers (2018). Exchange processes in the atmospheric boundary layer over
 954 mountainous terrain. *Atmosphere*, 9(3), 102. doi: 10.3390/atmos9030102
- 955 Shi, Y. (2021a). *Ground Radiometers on Stand for Upwelling Radiation (GN-*
 956 *DRAD60S)*. (Date accessed: 2022-08-21) doi: 10.5439/1377837
- 957 Shi, Y. (2021b). *Sky Radiometers on Stand for Downwelling Radiation*
 958 *(SKYRAD60S)*. (Date accessed: 2022-08-21) doi: 10.5439/1377836
- 959 Skamarock, W. C. (2004, December). Evaluating mesoscale NWP models using ki-
 960 netic energy spectra. *Mon. Wea. Rev.*, 132(12), 3019–3032. Retrieved 2022-
 961 09-11, from <http://journals.ametsoc.org/doi/10.1175/MWR2830.1> doi: 10
 962 .1175/MWR2830.1
- 963 Skamarock, W. C., & Klemp, J. B. (2008, March). A time-split nonhydro-
 964 static atmospheric model for weather research and forecasting applica-
 965 tions. *J. Comput. Phys.*, 227(7), 3465–3485. Retrieved 2022-09-11, from
 966 <https://linkinghub.elsevier.com/retrieve/pii/S0021999107000459>
 967 doi: 10.1016/j.jcp.2007.01.037
- 968 Smirnova, T. G., Brown, J. M., Benjamin, S. G., & Kenyon, J. S. (2016). Modifi-
 969 cations to the Rapid Update Cycle Land Surface Model (RUC LSM) available
 970 in the Weather Research and Forecasting (WRF) Model. *Mon. Wea. Rev.*,
 971 144(5), 1851–1865. doi: 10.1175/MWR-D-15-0198.1
- 972 Song, Y., Zhu, T., Cai, X., Lin, W., & Kang, L. (2007). Glacier winds in
 973 the Rongbuk Valley, north of Mount Everest: 1. Meteorological model-
 974 ing with remote sensing data. *J. Geophys. Res.*, 112(D11), D11101. doi:
 975 10.1029/2006JD007867
- 976 Stigter, E. E., Steiner, J. F., Koch, I., Saloranta, T. M., Kirkham, J. D., & Im-
 977 merzeel, W. W. (2021). Energy and mass balance dynamics of the seasonal
 978 snowpack at two high-altitude sites in the Himalaya. *Cold Regions Science and*
 979 *Technology*, 183, 103233. doi: 10.1016/j.coldregions.2021.103233
- 980 Stull, R. B. (1988). *An introduction to boundary layer meteorology*. Dordrecht, The
 981 Netherlands: Kluwer Academic Publishers, 666 pp.
- 982 Sullivan, R., Billesbach, D., Keeler, E., & Ermold, B. (2021). *Eddy Correlation Flux*
 983 *Measurement System (30ECOR)*. doi: 10.5439/1025039
- 984 Turner, D. D., & Blumberg, W. G. (2019). Improvements to the AERIOe ther-
 985 modynamic profile retrieval algorithm. *IEEE Journal of Selected Topics in Ap-
 986 plied Earth Observations and Remote Sensing*, 12(5), 1339–1354. doi: 10.1109/
 987 JSTARS.2018.2874968
- 988 Turner, D. D., Knuteson, R. O., Revercomb, H. E., Lo, C., & Dedecker, R. G.

- 989 (2006). Noise reduction of Atmospheric Emitted Radiance Interferometer
 990 (AERI) observations using principal component analysis. *J. Atmos. Oceanic*
 991 *Technol.*, *23*(9), 1223–1238. doi: 10.1175/JTECH1906.1
- 992 Turner, D. D., & Löhnert, U. (2021). Ground-based temperature and humidity
 993 profiling: combining active and passive remote sensors. *Atmos. Meas. Tech.*,
 994 *14*(4), 3033–3048. doi: 10.5194/amt-14-3033-2021
- 995 Turner, D. D., & Löhnert, U. (2014, 03). Information content and uncertainties in
 996 thermodynamic profiles and liquid cloud properties retrieved from the ground-
 997 based atmospheric emitted radiance interferometer (AERI). *J. Appl. Meteor.*
 998 *Climatol.*, *53*(3), 752–771. doi: 10.1175/JAMC-D-13-0126.1
- 999 Wagner, T. J., Klein, P. M., & Turner, D. D. (2019). A new generation of ground-
 1000 based mobile platforms for active and passive profiling of the boundary layer.
 1001 *Bull. Amer. Meteor. Soc.*, *100*(1), 137–153. doi: 10.1175/BAMS-D-17-0165.1
- 1002 Wang, X., Parrish, D., Kleist, D., & Whitaker, J. (2013). GSI 3DVar-based
 1003 ensemble-variational hybrid data assimilation for NCEP Global Forecast
 1004 System: Single-resolution experiments. *Mon. Wea. Rev.*, *141*(11), 4098–4117.
 1005 doi: 10.1175/MWR-D-12-00141.1
- 1006 Whiteman, C. D. (1982). Breakup of temperature inversions in deep mountain val-
 1007 leys. *J. Appl. Meteor.*, *21*, 270–289. doi: 10.1175/1520-0450(1982)021<0270:
 1008 BOTIID>2.0.CO;2
- 1009 Whiteman, C. D. (2000). *Mountain meteorology fundamentals and applications*. New
 1010 York: Oxford University Press, 355 pp.
- 1011 Whiteman, C. D., Bian, X., & Zhong, S. (1999). Wintertime evolution of the tem-
 1012 perature inversion in the Colorado Plateau Basin. *J. Appl. Meteor.*, *38*(8),
 1013 1103–1117. doi: 10.1175/1520-0450(1999)038<1103:WEOTTI>2.0.CO;2
- 1014 Xu, Z., Siirila-Woodburn, E. R., Rhoades, A. M., & Feldman, D. (2022). Sensitiv-
 1015 ities of subgrid-scale physics schemes, meteorological forcing, and topographic
 1016 radiation in atmosphere-through-bedrock integrated process models: A case
 1017 study in the Upper Colorado River Basin. *EGUsphere*, *2022*, 1–29. doi:
 1018 10.5194/egusphere-2022-437
- 1019 Zardi, D., & Whiteman, C. D. (2013). Diurnal mountain wind systems. In
 1020 F. K. Chow, S. F. J. De Wekker, & B. J. Snyder (Eds.), *Mountain weather*
 1021 *research and forecasting* (pp. 35–119). Dordrecht: Springer.
- 1022 Zhong, S., & Chow, F. K. (2013). Meso- and fine-scale modeling over complex ter-
 1023 rain: Parameterizations and applications. In F. K. Chow, S. F. De Wekker,
 1024 & B. J. Snyder (Eds.), *Mountain weather research and forecasting: Recent*
 1025 *progress and current challenges* (pp. 591–653). Dordrecht: Springer Nether-
 1026 lands. doi: 10.1007/978-94-007-4098-3_10

1 **Passive remote sensing of the atmospheric boundary**
2 **layer in Colorado’s East River Valley during the**
3 **seasonal change from snow-free to snow-covered ground**

4 **Bianca Adler^{1,2}, James Wilczak,² Laura Bianco^{1,2}, Ludovic Bariteau^{1,2},**
5 **Christopher J. Cox², Gijs de Boer^{1,2,3}, Irina Djalalova^{1,2}, Michael Gallagher^{1,2},**
6 **Janet M. Intrieri², Tilden Meyers,⁴ Timothy Myers^{1,2}, Joseph B. Olson⁵,**
7 **Sergio Pezoa^{1,2}, Joseph Sedlar^{1,6}, Elizabeth Smith⁷, David D. Turner⁵, Allen**
8 **White²**

9 ¹Cooperative Institute for Research in Environmental Sciences (CIRES), University of Colorado Boulder

10 ²NOAA Physical Sciences Laboratory, Boulder CO

11 ³IRISS, University of Colorado, Boulder CO

12 ⁴NOAA Air Resources Laboratory, Boulder CO

13 ⁵NOAA Global Systems Laboratory, Boulder CO

14 ⁶NOAA Global Monitoring Laboratory, Boulder CO

15 ⁶NOAA National Severe Storms Laboratory, Norman OK

16 **Key Points:**

- 17 • Temperature profiles retrieved from remotely sensed infrared radiances allow to
18 study the valley boundary layer over different snow covers.
- 19 • The nocturnal inversion in a high-altitude mountain valley is mixed out under snow-
20 free conditions and persists during daytime over snow.
- 21 • NOAA’s operational weather prediction model struggles to correctly forecast the
22 boundary layer likely due to the too coarse grid spacing.

Abstract

The structure and evolution of the atmospheric boundary layer (ABL) under clear-sky fair weather conditions over mountainous terrain is dominated by the diurnal cycle of the surface energy balance and thus strongly depends on surface snow cover. We use data from three passive ground-based infrared spectrometers deployed in the East River Valley in Colorado’s Rocky Mountains to investigate the response of the thermal ABL structure to changes in surface energy balance during the seasonal transition from snow-free to snow-covered ground. Temperature profiles were retrieved from the infrared radiances using the optimal estimation physical retrieval TROPoe. A nocturnal surface inversion formed in the valley during clear-sky days, which was subsequently mixed out during daytime with the development of a convective boundary layer during snow-free periods. When the ground was snow covered, a very shallow convective boundary layer formed, above which the inversion persisted through the daytime hours. We compare these observations to NOAA’s operational High-Resolution-Rapid-Refresh (HRRR) model and find large warm biases on clear-sky days resulting from the model’s inability to form strong nocturnal inversions and to maintain the stable stratification in the valley during daytime when there was snow on the ground. A possible explanation for these model shortcomings is the influence of the model’s relatively coarse horizontal grid spacing (3 km) and its impact on the model’s ability to represent well-developed thermally driven flows, specifically nighttime drainage flows.

Plain Language Summary

We investigated how the vertical temperature structure in a high-altitude mountain valley in Colorado’s Rocky Mountains evolves over snow-free and snow-covered ground. The vertical temperature structure in valleys determines how well air and thus pollutants in the valley can be mixed with the air above and is thus decisive for air quality and human health. During the night, air near the surface cools more than air above leading to an increase of temperature with height, a so-called temperature inversion forms which suppresses vertical mixing. During the day, solar radiation warms the ground and vertically mixes the air in the valley. When the ground is snow-covered, the mixing is limited to a shallow layer of a few hundred meter depth adjacent to the surface and the nocturnal inversion persists above through the daytime hours trapping air in the valley. We compared the observations to NOAA’s operational forecast model and found that minimum nighttime temperatures and daytime mixing were overestimated by the model, especially over snow-covered ground. We attributed the model errors to the relatively coarse horizontal grid spacing of 3 km, which suggests that a reduction of grid spacing in the operational model could improve the forecast accuracy in mountainous terrain.

1 Introduction

The atmospheric boundary layer (ABL) is the lowest part of the atmosphere that is directly affected by the Earth’s surface (Stull, 1988). Over mountainous terrain under clear sky fair weather conditions, the evolution of its structure is forced by convection and thermally driven circulations (Zardi & Whiteman, 2013; Serafin et al., 2018), which, in turn, are influenced by diurnal and terrain-induced variability in surface radiation and energy balance. Nighttime radiative cooling and drainage flows (i.e. downslope and downvalley winds) lead to formation of a surface temperature inversion in valleys and basins, that is, a layer in which temperature increases with height. Depending on the magnitude of energy input at the surface during the day, the nocturnal temperature inversions may erode after sunrise, either due to the upward growth of a well-mixed convective boundary layer (CBL) and/or the descent of the inversion top (Whiteman, 1982). While the convective heating in snow-free valleys is usually sufficient to erode the nocturnal inversion (e.g. Herrera-Mejía & Hoyos, 2019; Adler, Gohm, et al., 2021), multi-

73 day low-level inversions may persist in snow-covered valleys with very shallow CBLs form-
74 ing above the ground (e.g. Chemel et al., 2016; Llargeron & Staquet, 2016a, 2016b; Adler,
75 Wilczak, et al., 2021). During periods with strong persistent inversions, pollutants can
76 accumulate in valleys with significant implications for air quality and human health (e.g.
77 Lareau et al., 2013; Llargeron & Staquet, 2016b). Over areas of continuous snow cover,
78 average net radiation and sensible heat flux are often negative during wintertime (e.g.
79 Cullen & Conway, 2015; Stigter et al., 2021; Mott et al., 2018) meaning that solar en-
80 ergy is reflected and the surface is emitting energy, primarily at longer (infrared) wave-
81 lengths. Over patchy horizontally heterogeneous snow cover, very large differences in albedo
82 and surface fluxes occur on small scales, internal boundary layers form, and local advec-
83 tion of sensible heat becomes relevant (Mott et al., 2018).

84 Errors and uncertainties in mesoscale numerical weather prediction (NWP) mod-
85 els are usually amplified over mountainous terrain compared to flat terrain (Zhong & Chow,
86 2013, and references therein). One common problem is that nocturnal inversions in val-
87 leys are often too weak compared to observations, which may result in misrepresenta-
88 tion of the breakup of inversions during the day. Model performance largely depends on
89 the specific configuration, including details related to horizontal and vertical grid spac-
90 ing, domain extent, grid nesting, and the initial and boundary conditions applied. Also,
91 the physical parameterizations employed, such as turbulence and boundary layer param-
92 eterizations, land surface models (LSM), land use data sets, and radiation models, play
93 a central role in dictating model performance. One item that is known to be particularly
94 problematic is the model’s horizontal grid spacing, as coarse resolution limits the capa-
95 bility of the model to represent the detailed orographic structure of mesoscale valleys and
96 tributaries. Additionally, terrain smoothing used in some NWP systems results in the
97 underestimation of elevation differences between ridges and valley floors. Evaluating the
98 configuration of a specific model is also impacted by coarse resolution, as the detailed
99 observations required for such evaluation are often from instrumentation deployed to a
100 single location. This is particularly problematic in areas of complex terrain, where there
101 can be substantial variability in ABL conditions over very short distances. For exam-
102 ple, large differences between simulated and observed ABL thermal structure may re-
103 sult if observational data collected on a valley floor is compared to the nearest model grid
104 point, located on the adjacent slope. In general, high resolutions are required to accu-
105 rately portray flows over complex terrain, in part due to the need to have multiple grid
106 points present to detect features of interest. For example, to resolve flow features such
107 as thermally driven winds, the feature scale should be 6-8 times the horizontal grid spac-
108 ing according to Skamarock (2004) and Skamarock and Klemp (2008). This means that
109 models with a grid spacing on the order of 2-3 km would not be able to adequately cap-
110 ture features of less than 15 km in scale.

111 Much of the research on the ABL structure and evolution in snow-covered valleys
112 is based on *in situ* measurements on surface towers or airborne platforms such as radioson-
113 des and tether sondes. While the latter give detailed information on the vertical struc-
114 ture of the ABL, the measurements are not continuous and only provide snapshots. This
115 can be problematic in areas where atmospheric conditions evolve at time scales signif-
116 icantly shorter than those observed by these platforms. Great potential to gain a deeper
117 insight in the evolution of the vertical thermal ABL structure comes from ground-based
118 remote sensing instruments such as passive microwave radiometers and infrared spec-
119 trometers and active water vapor absorption lidars (Turner & Löhnert, 2021), which pro-
120 vide continuous information on the profiles of temperature and humidity. Such instru-
121 ments have been successfully deployed to study, for example, the summertime ABL in
122 a valley on the mountainous island of Corsica (Adler & Kalthoff, 2014), the wintertime
123 ABL in a snow-covered valley in the French Alps (Chemel et al., 2016), and the ABL
124 in a tropical valley in the Colombian Andes (Herrera-Mejía & Hoyos, 2019). The eval-
125 uation of NWP models in mountainous terrain is often based on near-surface measure-
126 ments only, as these measurements are widespread and readily available. However, im-

127 portant quantities like ABL depth and thermal stratification can only be evaluated against
128 profile measurements which emphasizes the value of continuous remotely sensed profiles
129 for NWP model evaluation. By utilizing both types of observations, Adler, Wilczak, et
130 al. (2022) evaluated the representation of a wintertime persistent cold air pool in differ-
131 ent versions of the National Oceanic and Atmospheric Administration (NOAA) opera-
132 tional High-Resolution-Rapid-Refresh (HRRR) model.

133 In this study, we investigate the response of the ABL thermal vertical structure to
134 changes in the energy balance at the surface during the seasonal transition from snow-
135 free to snow-covered ground in a high-altitude valley using continuous remotely sensed
136 temperature profiles. We then compare these observations to the operational HRRR model
137 to evaluate the model performance and investigate possible reasons for model errors. To
138 clearly isolate the response of the ABL to changes in snow cover and to avoid compli-
139 cating factors such as low-level clouds or synoptically-driven flows, we focus on completely
140 clear-sky days. Our research questions are grouped into two sets of questions, with the
141 first focused on process understanding, and the second focused on model evaluation: (i)
142 What is the vertical thermal structure of the ABL under different snow-cover conditions
143 and how does that structure change along the valley? How do the nocturnal tempera-
144 ture inversion, CBL, and stratification in the valley atmosphere vary temporally and spa-
145 tially? (ii) How well does the operational HRRR model capture the conditions in the val-
146 ley? Do the model errors depend on the time of the day, snow cover, and meteorolog-
147 ical situation, and do they vary along the valley?

148 To address these questions, we use data from a collaborative research initiative cur-
149 rently ongoing in the East River Watershed of Colorado. This work includes efforts as-
150 sociated with the National Oceanic and Atmospheric Administration (NOAA) Study of
151 Precipitation, the Lower Atmosphere, and Surface for Hydrometeorology (SPLASH, NOAA
152 Physical Science Laboratory, 2021b) and the U.S. Department of Energy (DOE) Atmo-
153 spheric Radiation Measurement (ARM) program Surface Atmosphere Integrated Field
154 Laboratory (SAIL, Feldman et al., 2021) campaigns. The main focus of the SPLASH ini-
155 tiative is to enhance weather and water prediction capabilities by measuring, evaluat-
156 ing, and understanding integrated atmospheric and hydrologic processes relevant to wa-
157 ter resources. The East River Watershed is a representative mountainous headwater catch-
158 ment of the Colorado River Basin, which is a primary source of water for much of the
159 southwestern United States. As part of the multi-year SPLASH and SAIL field campaigns,
160 three passive remote sensing infrared spectrometers were deployed simultaneously along
161 the axis of the East River Valley for a three-month period from the end of October 2021
162 to the end of January 2022, covering the seasonal change from snow-free to snow-covered
163 ground. To our knowledge, this is the first time such an instrument combination is used
164 to study the spatio-temporal characteristics of the ABL in a high-altitude valley. To ob-
165 tain temperature profiles from infrared spectrometers, we use an optimal estimation phys-
166 ical retrieval (i.e. Tropospheric Remotely Observed Profiling via Optimal Estimation (TROPOe
167 Turner & Löhnert, 2014; Turner & Blumberg, 2019; Turner & Löhnert, 2021). We then
168 compare the observations to model output at the grid point closest to the stations to in-
169 vestigate model errors under different snow-cover conditions.

170 The manuscript is structured as follows: Section 2 describes the investigation area
171 as well as the observational and model data. In Sect. 3, the temporal evolution of ob-
172 served near-surface conditions, including radiation and energy balance components dur-
173 ing the whole 3-month period, is analyzed (Sect. 3.1). This is followed by an investiga-
174 tion of the observed diurnal cycle of the ABL on a day-to-day basis at one site (Sect. 3.2)
175 and along the valley axis using 24-h composites (Sect. 3.3). In Sect. 4, the ABL ther-
176 mal structure in the HRRR model is evaluated (Sect. 4.1) and possible reasons for the
177 model errors are discussed (Sect. 4.2).

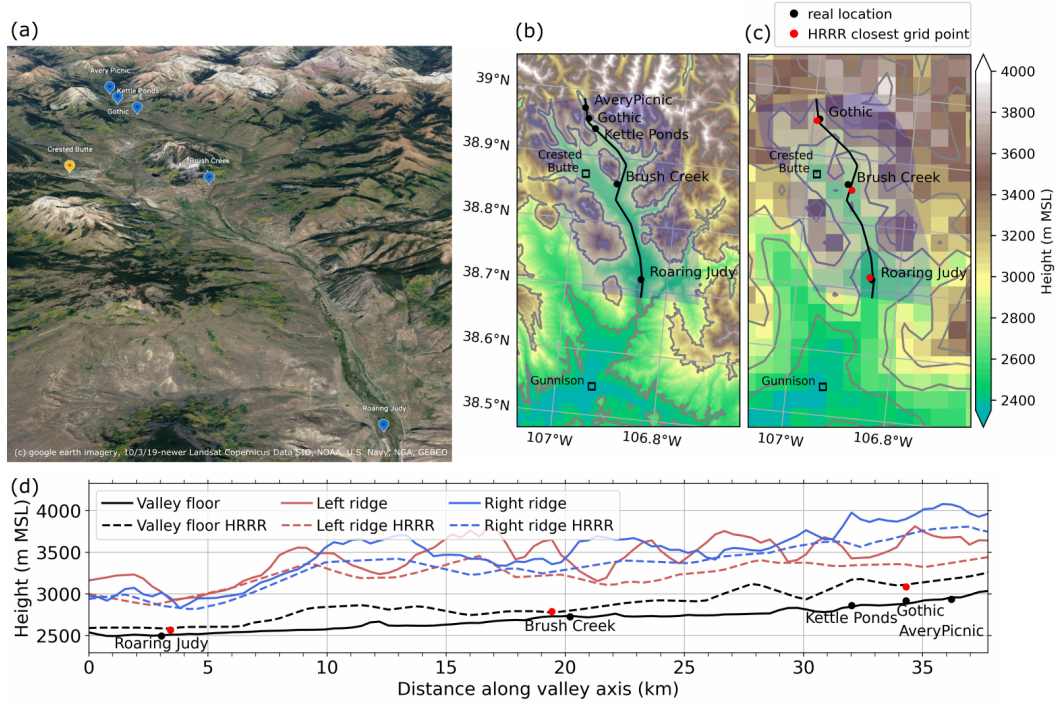


Figure 1. (a) Google earth imagery of the investigation area. Terrain height (b) based on 30-m resolution elevation data from the Shuttle Radar Topography Mission and (c) as used in the operational HRRR model with 3 km grid spacing. (d) Elevation of the valley floor and ridges (left and right of the valley axis when looking upvalley) computed from SRTM and HRRR elevation data along the axis of the East River Valley indicated by the black line in (b) and (c). The shaded polygon in (b) and (c) marks the area used for the estimates of the ridge heights. Black and red dots in (b)-(d) indicate the location and heights of the sites in the real world and in the HRRR model grid.

2 Investigation area, observational, and model data

The study area is the East River Valley, which is embedded in the East River Watershed and located near Crested Butte and Gunnison in Colorado’s Rocky Mountains (Fig. 1a,b). The land cover type is a mix of evergreen and deciduous forest, grasslands, and barren land (Xu et al., 2022). The distance along the valley axis from the measurement site furthest down the valley (Roaring Judy) to the site furthest up the valley (Avery Picnic) is around 35 km (Fig. 1). All measurement sites are on the valley floor. The valley floor rises from around 2500 m above mean sea level (MSL) at Roaring Judy to nearly 3000 m MSL at Avery Picnic. The valley depth on average is more than 500 m and the flat part of the valley floor ranges in width from a few kilometers at its widest part to less than 1 km near the Kettle Ponds, Gothic, and Avery Picnic sites.

While the valley orography is much smoother in the 3-km HRRR model configurations, the primary features of the valley are still resolved (Fig. 1c). To characterize the ridge height on both sites of the valley floor in the observations and simulations, we manually defined a valley axis (black line in Fig. 1b,c) and extracted elevation data along slices perpendicular to the valley axes spanning 10 km on each side. For each slice and each side of the valley we determined the maximum elevation value. Figure 1d shows the elevation of the valley floor and ridges in reality (solid lines) and in the HRRR model (dashed lines). As can be expected due to the coarse model resolution, valley depth is reduced in the model compared to reality. In an automated near-real time routine, model data at the grid points closest to the real-world locations of the sites (red dots in Fig. 1c) are extracted from the operational HRRR forecasts. We evaluated the HRRR data at Gothic, Brush Creek and Roaring Judy, since these are the sites where continuous temperature profiles from the TROPoe retrievals were available. The extracted model grid points for these sites are on the simulated valley floor (Fig. 1c,d).

2.1 Observational data

2.1.1 Thermodynamic profilers

Three ground-based infrared spectrometers were deployed along the axis of the East River Valley at Gothic, Brush Creek, and Roaring Judy during the three-month investigation period from 21 October 2021 to 28 January 2022. At Gothic, an Atmospheric Emitted Radiance Interferometer (AERI Knuteson et al., 2004b, 2004a) is operated as part of the second ARM Mobile Facility (AMF2) deployed for the SAIL campaign (Feldman et al., 2021). A second AERI was deployed at Brush Creek as part of the Collaborative Lower Atmospheric Mobile Profiling System (CLAMPS) system (Wagner et al., 2019). A third infrared spectrometer at Roaring Judy was an Atmospheric Sounder Spectrometer by Infrared Spectral Technology (ASSIST Rochette et al., 2009) operated by NOAA’s Physical Science Laboratory. The AERI and ASSIST generally have the same functionality, construction, and operating principles. While the AERI at Gothic and the ASSIST at Roaring Judy were operated during the whole study period, the AERI at Brush Creek was taken down 10 days earlier on 18 January to support a separate field campaign.

The AERI and ASSIST are passive spectrometers that receive downwelling infrared radiation between the wavelengths of 3.3 and 19 μm ($520\text{-}3000\text{ cm}^{-1}$) at a spectral resolution of about 0.5 wavenumber (Knuteson et al., 2004b, 2004a). The instruments have a hatch that closes during precipitation events to protect the fore optics, which inhibits measurements during rain or snow. We retrieved thermodynamic profiles every 10 min from the observed instantaneous radiances using the optimal estimation physical retrieval TROPoe (Turner & Löhnert, 2014; Turner & Blumberg, 2019; Turner & Löhnert, 2021). The spectral bands used in the retrieval are in the wavenumber range from 612 - 905.4 cm^{-1} and are specified in Turner and Löhnert (2021). Additional input data in TROPoe are cloud base height from a colocated ceilometer, temperature and water vapor mixing ratio from near-surface measurements and from hourly analysis profiles from the op-

229 erational Rapid Refresh (RAP, Benjamin et al., 2016) weather prediction model at the
 230 closest grid point. The latter are used only outside the ABL above 4 km above ground
 231 level (AGL) and provide information in the middle and upper troposphere where little
 232 to no information content is available from the infrared radiances. In addition to these
 233 temporally resolved input data, TROPoe requires an a priori dataset (*prior*) which pro-
 234 vides mean climatological estimates of thermodynamic profiles and specifies how tem-
 235 perature and humidity covary with height as an input (for details see e.g. Djalalova et
 236 al., 2022). The prior is a key component of the retrieval and provides a constraint on the
 237 ill-posed inversion problem. For this study, we computed the prior from operational ra-
 238 diosondes launched near Denver, CO, and re-centered the mean profiles of water vapor
 239 and temperature to account for the elevation difference between the East River Valley
 240 and the launch site near Denver to get a more representative prior (for details see Ap-
 241 pendix Appendix A).

242 The retrieval determines the optimal state vector, which consists of thermodynamic
 243 profiles, and satisfies both the observations, RAP profiles above 4 km AGL, and the prior.
 244 The state vector includes temperature and water vapor profiles with 55 vertical levels
 245 each from the surface up to 17 km, with the distance between levels starting at 10 m and
 246 increasing with height, as well as liquid water path. Starting with the mean prior as a
 247 first guess of the state vector, a forward model is used to compute pseudo-observations,
 248 which are then compared to the actual observations. The retrieval iterates until the dif-
 249 ferences between the pseudo-observations and the observations are small within a spec-
 250 ified uncertainty. As the forward model, we use the Line-By-Line Radiative Transfer Model
 251 LBLRTM (Clough & Iacono, 1995; Clough et al., 2005).

252 Before running TROPoe, a principal component noise filter is applied to the infrared
 253 radiances to reduce the random error (Turner et al., 2006). Ideally, uncertainties in the
 254 observations, prior, and forward model are propagated and characterized by the poste-
 255 rior covariance matrix. Because including the uncertainty of the forward model would
 256 increase the computational costs of the retrieval substantially, we assume the uncertainty
 257 of the forward model is zero and inflate the uncertainty associated with the observed ra-
 258 diances by using the radiance uncertainty before noise filtering is applied (for details see
 259 Turner & Blumberg, 2019). Because the AERI performs longer sky averages than the
 260 ASSIST, the radiance uncertainty of the AERI is lower and we found that it was not suf-
 261 ficient to compensate for the missing uncertainty in the forward model, resulting in an
 262 overfitting of the profiles. We hence further increased the noise in the AERI radiances
 263 by multiplying the radiance uncertainties with a factor for which the retrieved temper-
 264 ature profiles best agreed with the radiosonde profiles (for details see Appendix Appendix
 265 B).

266 **2.1.2 Surface observations**

267 Measurements of 2-m temperature and horizontal wind speed and direction were
 268 obtained at five sites along the valley axis, including Avery Picnic, Gothic, Kettle Ponds,
 269 Brush Creek, and Roaring Judy. Wind measurement heights were 3.8 m AGL at Avery
 270 Picnic, 10 m AGL at Gothic, 3 m AGL at Kettle Ponds and Brush Creek, and 4 m AGL
 271 at Roaring Judy. Measurement heights refer to snow-free ground, the growing snowpack
 272 reduced the height separation between sensor and surface through the season. Up- and
 273 downwelling longwave and shortwave radiation flux components as well as 30-min sen-
 274 sible heat fluxes were measured at the upper four sites, Avery Picnic, Gothic, Kettle Ponds,
 275 and Brush Creek, and precipitation measurements were used from Gothic. In this study,
 276 net radiation is positive when directed downwards towards the surface and sensible heat
 277 flux is positive when directed upwards away from the surface.

278 All data at Gothic were collected with AMF2. At the other sites, we utilized data
 279 from Atmospheric Surface Flux Stations (ASFS, Cox et al. (2023)) at Avery Picnic and

280 Kettle Ponds (sensible heat flux only) and from mobile SURFRAD-like stations (Butterworth
 281 et al., 2021; Sedlar et al., 2022) at Brush Creek and Kettle Ponds for radiation, cloud
 282 properties, and meteorology. To estimate albedo we averaged shortwave downward and
 283 shortwave upward radiation fluxes when the solar zenith angle was less than 85° before
 284 computing the ratio. At Gothic and Brush Creek, measurements of direct and diffuse
 285 solar radiation were available to compute shortwave downward radiation fluxes (McArthur,
 286 2005), while at the other sites we used broadband fluxes. Details on the platforms and
 287 sensors can be found in the meta data for the individual data sets (see Data Availabil-
 288 ity section).

289 **2.1.3 Radiosondes**

290 As part of the AMF2 deployment, radiosondes were launched twice daily at 5 and
 291 17 MST (0 and 12 UTC) at Gothic, providing thermodynamic and wind profiles through-
 292 out the troposphere. The radiosonde profiles were used to re-center the prior (Appendix
 293 Appendix A), to help determine the optimal uncertainty configuration for the AERIs (Ap-
 294 pendix Appendix B), and to compute different ABL quantities (Sect. 3.3). When com-
 295 paring the radiosonde profiles to TROPoe retrieved profiles, we first interpolated the ra-
 296 diosonde profiles to the same height levels as the retrieved profiles to avoid differences
 297 arising from the higher vertical resolution of the sonde.

298 **2.1.4 Ceilometer**

299 Four ceilometers manufactured by Vaisala were deployed at Gothic, Kettle Ponds,
 300 Brush Creek, and Roaring Judy measuring attenuated aerosol backscatter profiles with
 301 a temporal resolution of less than 1 min. In this study, we used the first cloud-base height,
 302 as determined using Vaisala’s CL-view software, to identify clear-sky and cloudy days.
 303 At each site, we computed a daily cloud-base fraction for cloud bases below 3 km AGL.
 304 We required it to be less than 5 % at all sites for a day to be considered clear-sky and
 305 we identified cloudy days for which the temporal low-level cloud-base fraction was larger
 306 than 50 % at any of the sites.

307 **2.1.5 Terra satellite**

308 To get information on the temporal evolution of spatial snow coverage in the area,
 309 we used the normalized difference snow index (NDSI) from MODIS on-board of the Terra
 310 satellite (Hall & Riggs, 2021). Snow-covered surfaces typically have a very high reflectance
 311 in visible bands and very low reflectance in shortwave infrared bands. The NDSI reveals
 312 the magnitude of this difference. NDSI is available daily on a regular grid with 500 m
 313 spacing. We computed a mean daily NDSI for the investigation area when valid NDSI
 314 data are available for at least 50 % of the pixels and not obscured by clouds.

315 **2.2 HRRR model data**

316 We evaluated the currently operational version of NOAA’s HRRR weather predic-
 317 tion model (version 4, Dowell et al., 2022) with a horizontal grid spacing of 3 km by com-
 318 paring the observations to the closest grid point in the model (Fig. 1c). The operational
 319 HRRR model is initialized hourly with a forecast horizon of 19 h. Every 6 hours, the fore-
 320 cast horizon is extended to 48 h. For this study, we used hourly model output from the
 321 48-hr forecasts which were initialized at 0, 6, 12, and 18 UTC. For each of these initial-
 322 ization times, we split the 48-hr forecasts in half and concatenated the first and last 24
 323 hours of the forecasts, illustrated in Fig. 2. This resulted in the development of a con-
 324 tinuous time series of model data for the different configurations (i.e., eight in total with
 325 four initialization times and forecast periods 0-23 and 24-47), which we could compare
 326 against the observations. With this method, discontinuities in model data resulted at

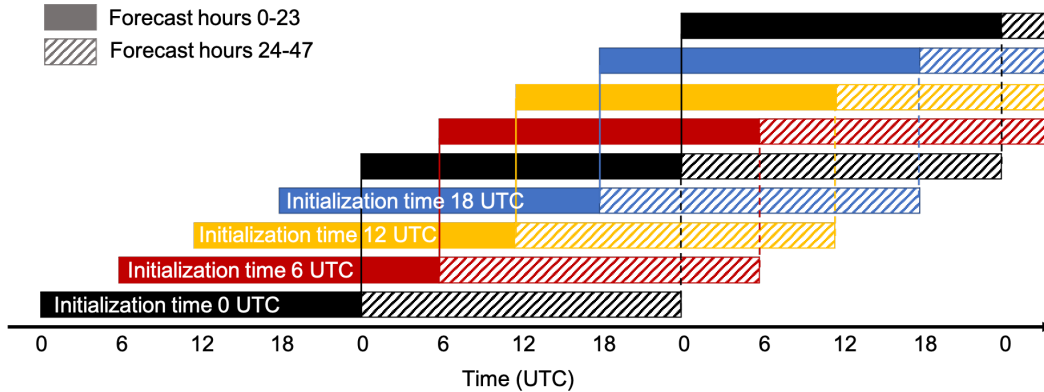


Figure 2. Illustration of the eight different configurations which are used to develop continuous time series of the HRRR model data. The different colored boxes indicate blocks of 24 h of data from runs initialized at different times, which are then concatenated to get continuous time series. Solid boxes indicate data from forecasts hour 0 to 23 and hatched boxes from 24-27.

327 the initialization times when the model data shifted from one forecast run to the next.
 328 We evaluated the model for all eight configurations and found that the main conclusions
 329 are similar for each configuration. Because of this, we decided to mostly show results from
 330 the first 24 hours of the forecasts initialized at 6 UTC (red boxes in Fig. 2).

331 Hourly model data were compared against instantaneous observation nearest in time
 332 with a maximum tolerance of 10 min, and simulated profiles were linearly interpolated
 333 to the measurement heights. Because wind observations were not performed at 10 m AGL
 334 at Brush Creek and Roaring Judy, the simulated 10-m horizontal wind data were reduced
 335 to the actual wind measurement height at the respective site assuming a logarithmic wind
 336 profile.

337 We computed 24-h composites of bias and mean absolute error (MAE) of temper-
 338 ature T as:

$$339 \quad Bias = \frac{1}{n} \sum_{i=1}^n (T_{i,model} - T_{i,obs}) \quad (1)$$

$$340 \quad MAE = \frac{1}{n} \sum_{i=1}^n |T_{i,model} - T_{i,obs}| \quad (2)$$

342 with n being the number of samples available at each hour of the day, T_{obs} being
 343 the observed temperature, and T_{model} being the simulated temperature.

344 **3 Observed evolution of the ABL during the seasonal snow cover change**

345 **3.1 Near-surface conditions**

346 Significant changes in near-surface conditions occurred during the three-month ob-
 347 servation period (Fig. 3) and these can clearly be linked to the snow cover. Smaller snow-
 348 fall events during the first half of the period (Fig. 3c) led to temporary increases in albedo
 349 (Fig. 3f), but this snow melted quickly and therefore did not result in an area-wide snow
 350 cover, as the mean NDSI values remained less than 20 % (Fig. 3d). This changed with
 351 a multi-day snowfall event between 6 and 10 December, after which the albedo increased
 352 to values larger than 0.9 and the mean NDSI remained above 60 % through the end of
 353 the investigation period in January. Using albedo and NDSI as criteria for snow cover,

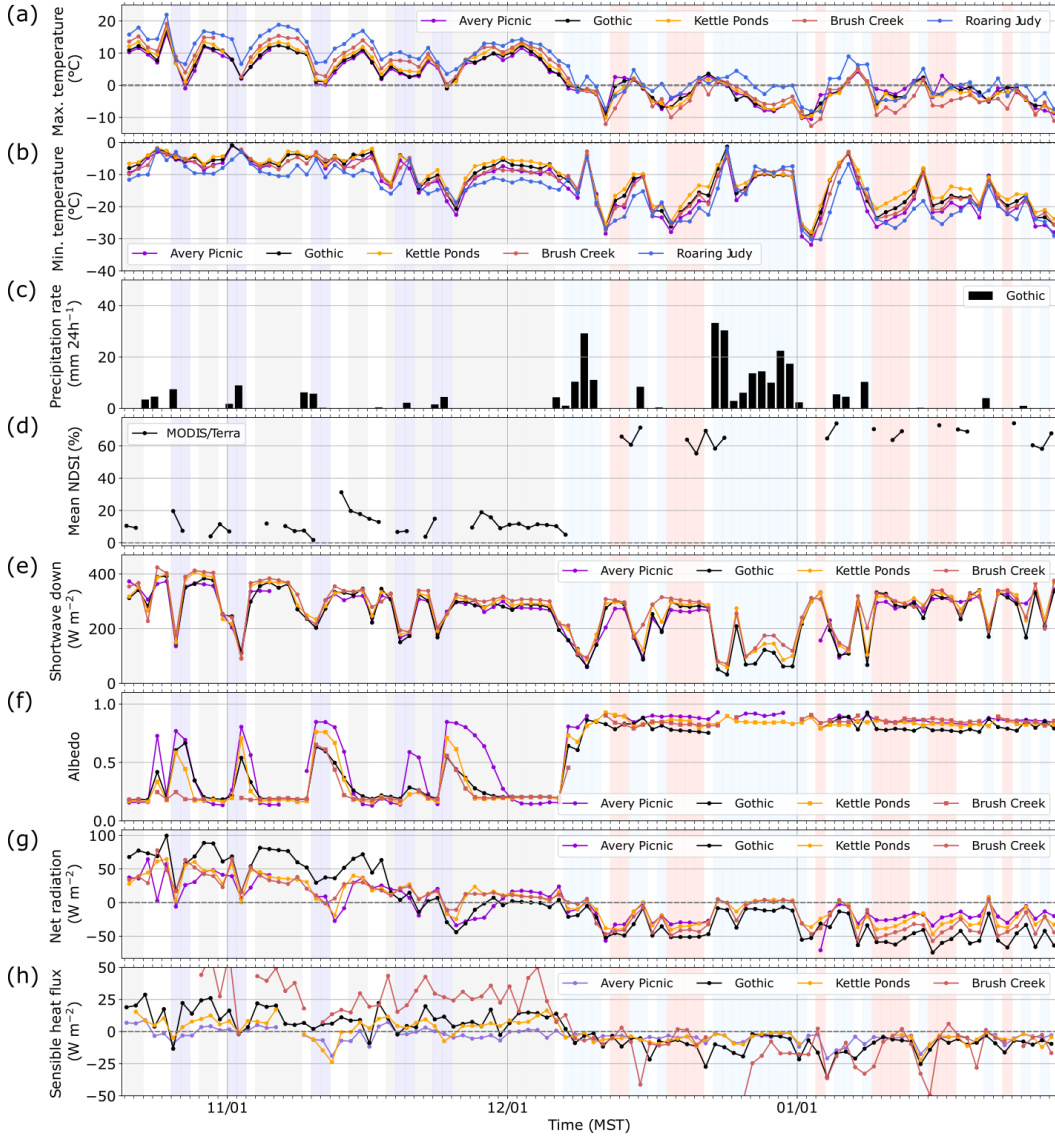


Figure 3. Daily (a) maximum and (b) minimum 2-m temperature, (c) daily precipitation rate, (d) domain mean normalized difference snow index (NDSI), (e) daily daytime mean shortwave downward radiation flux, (f) albedo at noon, (g) daily mean net radiation (positive when directed towards the surface), and (h) daily mean sensible heat flux (positive when directed away from the surface) during the 3-month investigation period. Grey and red shadings indicate clear-sky days and purple and blue shadings mark cloudy days during the snow-free and snow-covered regimes, respectively, determined using daily cloud-base fractions from ceilometers.

354 we split the observational period into two regimes. This includes a *snow-free* regime in-
 355 cluding and up to 6 December, during which any snow cover was patchy, intermittent,
 356 and heterogeneous, and a *snow-covered* regime including and following 7 December, dur-
 357 ing which a large fraction of the surface was continuously covered by snow. Visible cam-
 358 era images taken automatically at Gothic, Kettle Ponds, and Brush Creek confirmed the
 359 snow-cover change (not shown).

360 For both regimes, we identified clear-sky and cloudy days using cloud-base heights
 361 from the four ceilometers deployed along the valley axis (Sect. 2.1.4). Clear-sky days dur-
 362 ing the snow-free and snow-covered regime are indicated by gray and red shading and
 363 cloudy days by purple and blue shading in Fig. 3. During a few of the identified clear-
 364 sky days, mid-or high-level clouds occurred but were found to have a small impact on
 365 solar radiation (Fig. 3e).

366 Daily mean solar radiation on clear-sky days decreased before and increased after
 367 the winter solstice (Fig. 3e). This may explain the gradual decrease of daily mean net
 368 radiation (Fig. 3g) and daily maximum temperature (Fig. 3a) during the snow-free regime.
 369 Under snow-covered conditions, daily mean net radiation remained negative, even as one
 370 gets further away from winter solstice. Daily mean surface sensible heat flux dropped
 371 to negative values under snow-covered conditions (Fig. 3h), that is, it was directed to-
 372 wards the surface compensating for some of the surface radiative cooling (Fig. 3g). While
 373 maximum daytime temperatures regularly reached more than 10 °C under snow-free con-
 374 ditions at all sites, they generally did not exceed 0 °C on clear-sky days under snow-covered
 375 conditions (Fig. 3a). Minimum nighttime temperatures during clear-sky days were mostly
 376 between -5 to -10 °C under snow-free conditions, but regularly dropped below -20 °C un-
 377 der snow-covered conditions (Fig. 3b).

378 While the primary changes in near-surface conditions during the transition from
 379 snow-free to snow-covered ground generally occurred at all sites alike, differences are vis-
 380 ible between the sites on individual days which demonstrate the impact local terrain fea-
 381 tures can have on the surface energy balance components and air temperature. For ex-
 382 ample, the higher mean sensible heat fluxes at Brush Creek under snow-free conditions
 383 (Fig. 3h) were likely related to local site characteristics such as more rocks, more exposed
 384 aggregate, and fewer grass than at the other sites as well as its vicinity to a steep slope.
 385 Independent of snow cover, the overall lowest nighttime temperatures on clear-sky days
 386 were measured at Roaring Judy (Fig. 3b), that is the site furthest down the valley and
 387 lowest in altitude (Fig. 1) which is an indication of an extensive cold air pool filling the
 388 whole valley and which will be investigated in more detail in (Sect. 3.3). Despite being
 389 only a few kilometers apart from each other (Fig. 1d), minimum nighttime temperatures
 390 at the three sites furthest up the valley differed by several degrees with Avery Picnic mea-
 391 suring the lowest temperature (Fig. 3b). While the sites at Gothic and Kettle Ponds were
 392 not at the lowest point of the valley floor, the site at Avery Picnic was in close proxim-
 393 ity to the river and a small-scale terrain depression likely favored the formation of a lo-
 394 cal cold pool at this site.

395 3.2 Diurnal cycle of the ABL

396 After having investigated daily mean, minimum and maximum values in Sect. 3.1,
 397 we now focus on the diurnal cycle of the ABL through the snow-cover transition using
 398 measurements at Roaring Judy as an example (Fig. 4), as this was the site with the great-
 399 est and most continuous data availability for temperature profiles (Fig. 5a,b). While the
 400 2-m temperature on clear-sky days was overall lower under snow-covered conditions com-
 401 pared to snow-free conditions, a clear diurnal cycle was visible during both (Fig. 4a). Tem-
 402 perature started to increase about one hour after sunrise and started to decrease about
 403 one hour before sunset. Note that sunrise and sunset times were computed using the ge-

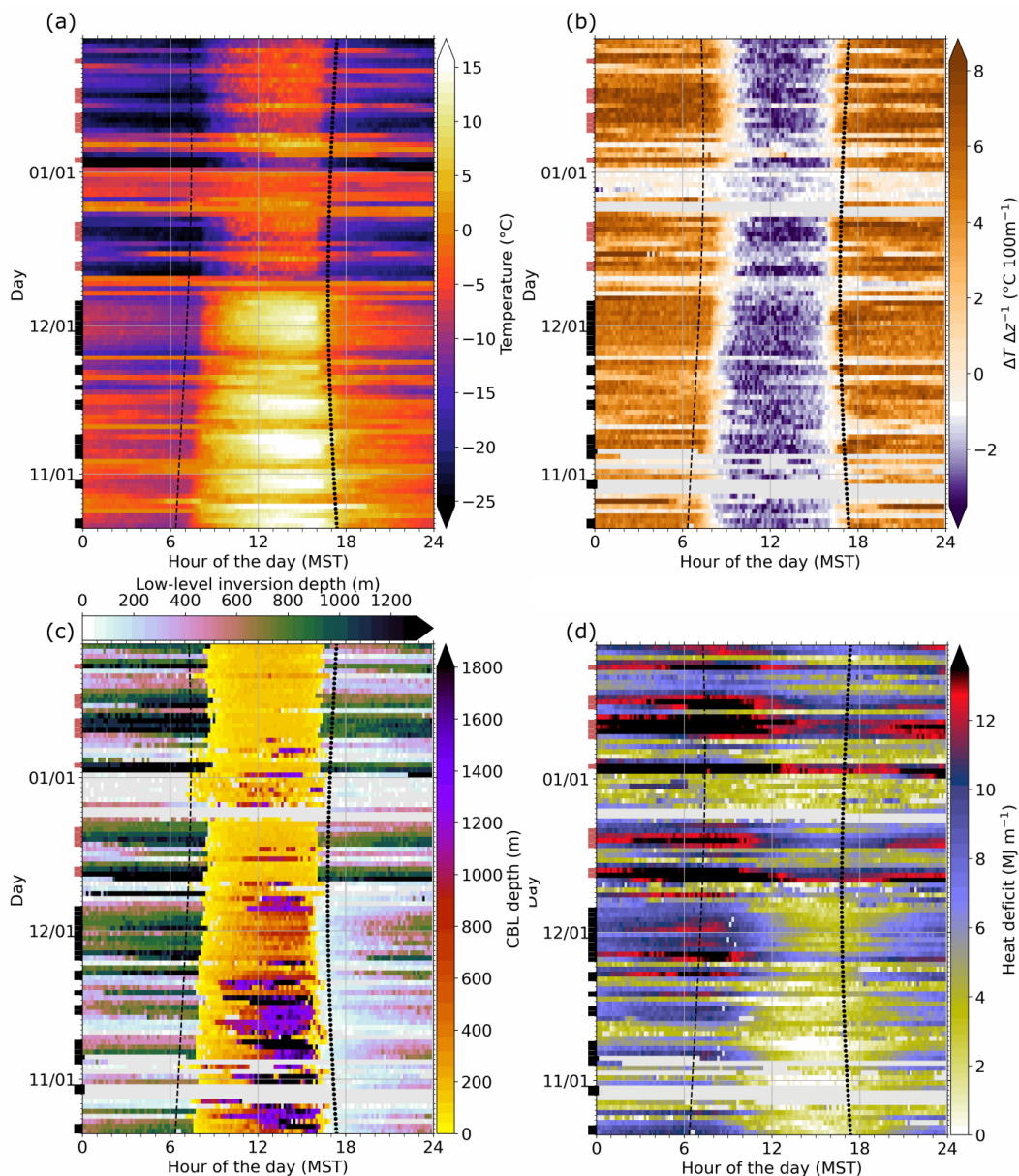


Figure 4. Daily evolution of (a) 2-m temperature, (b) temperature gradient over the lowest 100 m above ground, (c) CBL depth determined between sunrise and sunset using the parcel method and depth of the low-level inversion defined as the layer adjacent to the surface in which temperature increases with height, and (d) heat deficit computed after Eq. 3 at Roaring Judy. Besides the 2-m temperature, all quantities are computed using thermodynamic profiles retrieved with TROPoe. The dashed and dotted lines indicate sunrise and sunset, respectively. Black and red bars at the left y-axis indicate clear-sky days under snow-free and snow-covered conditions, respectively.

ographic location and do not consider local topographic impacts like shading from valley sidewalls.

Associated with the decrease in 2-m temperature shortly before sunset, a surface inversion regularly formed during clear-sky days as indicated by positive temperature gradients in the lowest 100 m AGL (Fig. 4b). Temperature gradients were typically around 5 to 6 °C 100 m⁻¹ and did not change much throughout the night. During the day, an unstable layer evolved near the surface, which was similar in strength (around -2 to -3 °C 100 m⁻¹) under both snow-cover conditions. The CBL, however, was much deeper under snow-free conditions (Fig. 4c). Its depth was computed between sunrise and sunset using the parcel method (Seibert et al., 2000), that is we determined the height at which the surface value of virtual potential temperature matched the virtual potential temperature profile. Duncan Jr. et al. (2022) found a good agreement for CBL depth estimates with the parcel method when using radiosonde and AERI-based TROPoe retrieved profiles.

The temporal evolution and depth of the stably stratified layer varied considerably with snow cover (Fig. 4c). We defined a low-level inversion as the layer adjacent to the surface in which temperature increased with height and determined its depth as the height above ground where temperature started to decrease. Under snow-free conditions, an inversion gradually formed, reaching average maximum depths of around 900 m in the early morning. In contrast when the ground was snow covered, an inversion of around 750 m depth on the average was detected as soon as the unstable layer near the surface diminished, preventing the detection of a CBL. This indicates that the very shallow CBL under snow-covered conditions was topped by a deep stably-stratified layer which connected to the surface-based inversion as soon as convection stopped. This will be investigated more in Sect. 3.3.

As a proxy for the stratification in the valley, we computed the heat deficit Q (Whiteman et al., 1999) from the surface (h_{sfc}) up to 4000 m MSL (this is the height above which we no longer found diurnal temperature changes, Sect. 3.3):

$$Q = c_p \int_{h_{\text{sfc}}}^{4000} \rho(z) [\theta_{4000} - \theta(z)] dz \quad (3)$$

where c_p is the specific heat capacity of air at constant pressure, $\rho(z)$ is the air density profile, θ_{4000} is the potential temperature at 4000 m MSL, and $\theta(z)$ denotes the potential temperature profile. With a station height of 2494 m MSL, the layer depth over which Q is computed amounts to 1500 m for Roaring Judy. Q describes the heat required to mix out the stable stratification below 4000 m MSL and to obtain a well-mixed layer with height-constant potential temperature. Small values indicate that the stratification is close to well-mixed, while large values are a sign of very stable layering. The temporal evolution of the heat deficit describes if stable layers are built, maintained or destroyed. Under snow-free conditions, the heat deficit showed a clear diurnal cycle with low values during daytime and high values during the night (Fig. 4d), reflecting the evolution of the CBL (Fig. 4c) which eroded the inversion during daytime and the build-up of the low-level inversion during nighttime. The heat deficit still generally decreased during the day under snow-covered conditions, which can be attributed to the formation of the shallow CBL (Fig. 4c) and upper-level warming (see Sect. 3.3), but the values remained much higher indicating that the stable layer was far from being mixed out. The persistent stable layer in the valley was washed out several times by synoptically-driven systems indicated by low heat deficit values (Fig. 4d), for example during the period between 24 December and 1 January, a period with heavy snowfall (Fig. 3b), but quickly rebuilt under clear-sky conditions.

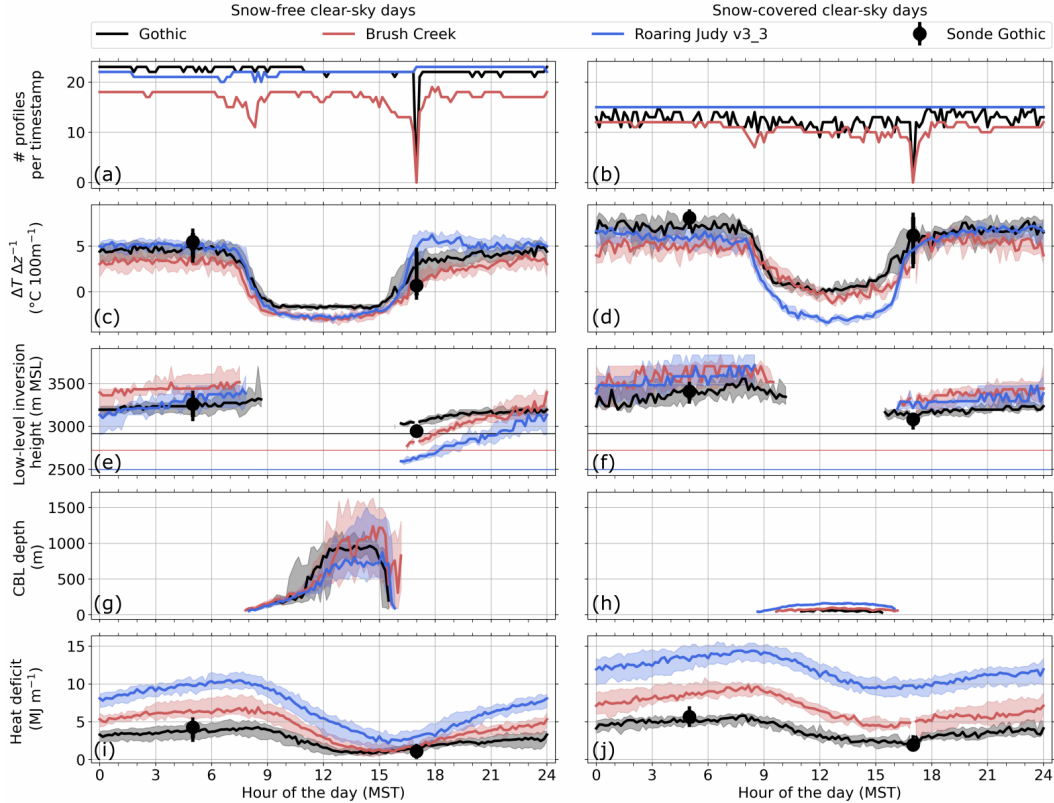


Figure 5. (a,b) Number of temperature profiles available for the analysis at each time stamp. 24-h median composites of (c,d) temperature gradient over the lowest 100 m AGL, (e,f) height of the low-level inversion defined as the layer adjacent to the surface in which temperature increases with height, (g,h) CBL depth determined between sunrise and sunset using the parcel method, and (i,j) heat deficit computed after Eq. 3 at Gothic, Brush Creek, and Roaring Judy for clear-sky days under snow-free (left column) and snow-covered (right column) conditions. In (c-j), shading marks the interquartile range. In (e,f), the thin horizontal lines indicate the respective station height. The black markers show quantities retrieved from the radio soundings at Gothic, all other quantities are computed using thermodynamic profiles retrieved with TROPoe.

452 Some of the changes we see in ABL conditions between both snow-cover regimes
 453 (Fig. 4) may be related to the reduction in solar radiation as one gets closer to winter
 454 solstice (Fig. 3d). However, the very abrupt changes right after the snowfall event ended
 455 on 10 December and the fact that the CBL depth remained low and the inversion remained
 456 deep even after solar radiation increased again in January, provide convincing evidence
 457 that the changes were dominated by snow cover strongly reflecting solar radiation and
 458 not by solar insolation.

459 3.3 Average ABL evolution along the valley axis

460 To compare the ABL evolution at the three sites Roaring Judy, Brush Creek, and
 461 Gothic along the valley axis (Fig. 1), we computed 24-h composites for clear-sky days
 462 under snow-free and snow-covered conditions of temperature profiles (Fig. 6) and, to pro-
 463 vide a quantitative analysis, of low-level stability, low-level inversion height, CBL depth,
 464 and heat deficit (Fig. 5).

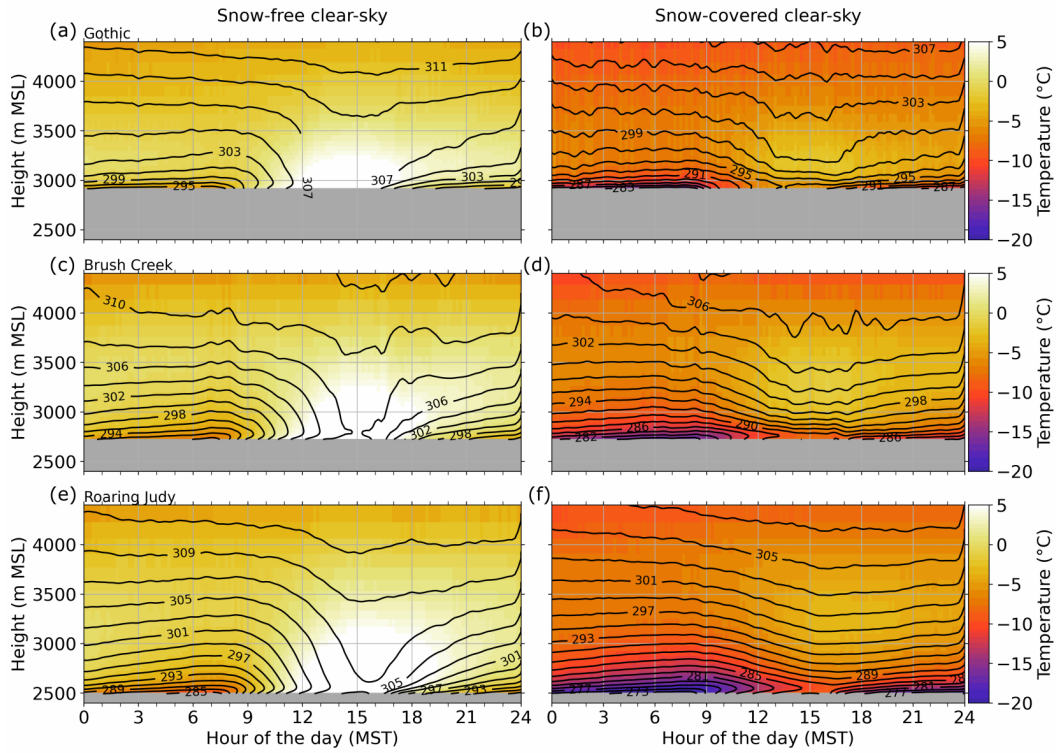


Figure 6. 24-h mean composites of temperature (color-coded) and potential temperature (iso-lines) profiles for clear-sky days under snow-free conditions (a,c,e) and snow-covered conditions (b,d,f) at Gothic (top row), Brush Creek (middle row), and Roaring Judy (bottom row). The thermodynamic profiles are retrieved with TROPoe.

465 The composite temperature profiles nicely show the much colder temperatures un-
 466 der snow-covered conditions (Fig. 6). The stratification in the valley was strongly stable
 467 at all sites during the night, independent of snow cover. A surface inversion started
 468 forming in the late afternoon indicated by an increase in the low-level temperature gra-
 469 dient (Fig. 5c,d). After the initial increase, the temperature gradients were nearly con-
 470 stant throughout the night and similar at all sites with values larger by approximately
 471 1-2 °C 100 m⁻¹ during the snow-covered regime. Under snow-free conditions, the inver-
 472 sion deepened gradually with time at all sites (Figs. 5e, 6a,c,e) with the strongest in-
 473 crease occurring during the first half of the night. After the initial growth, the inversion
 474 was quite stationary and very similar at all sites with respect to mean sea level indicat-
 475 ing that a layered cold pool formed in the East River Valley with the coldest air accu-
 476 mulating at the lowest parts of the valley. Under snow-covered conditions, no gradual
 477 increase in inversion depth was detected at any of the sites at the beginning of the night,
 478 but immediately occurred at around 3200 m MSL on the average (Fig. 5f). During its
 479 stationary phase, the inversion height was between around 3200 and 3700 m MSL which
 480 roughly coincided with ridge heights in the area (Fig. 1b,d). The temporal evolution of
 481 the low-level inversion is well reflected in the heat deficit with values increasing grad-
 482 ually during the night (Fig. 5i,j). Heat deficit values are largest at Roaring Judy, because
 483 this is the lowest altitude site and the inversion depth is largest and strongest here tem-
 484 perature increasing by 10 °C under snow-free conditions and 15 °C under snow-covered
 485 conditions from the surface to the top of the inversion (Fig. 6e,f).

486 Distinct differences in ABL structure are visible during daytime depending on snow
 487 cover. Under snow-free conditions, a well-mixed CBL developed equally at all sites af-
 488 ter sunrise reaching maximum depths of around 800 to 1000 m (Fig. 5g). It eroded the
 489 nocturnal temperature inversion in the valley (Fig. 6a,c,e) and resulted in near-zero heat
 490 deficit values in the afternoon (Fig. 5i). On the contrary, a very shallow CBL of less than
 491 150 m depth developed under snow-covered conditions Fig. 5h). Above the CBL, the val-
 492 ley atmosphere remained strongly stably stratified (Fig. 6b,d,f) causing the high heat
 493 deficit values during the day (Fig. 5j). This also explains why no gradual increase in in-
 494 version depth was detected at the beginning of the night (Fig. 5f). The thermal struc-
 495 ture of the ABL in the East River Valley under snow-covered conditions is very similar
 496 to the one found during wintertime in Alpine Valleys near Grenoble in the French Alps
 497 (Largeron & Staquet, 2016b, 2016a).

498 Even though the CBL was very shallow (Fig. 5h) and most of the valley atmosphere
 499 remained stably stratified during daytime (Fig. 6b,d,f), the heat deficit still decreased
 500 under snow-covered conditions (Fig. 5j). This can be related to a warming of the sta-
 501 bly stratified valley atmosphere up to around 4000 m MSL (Fig. 6b,d,f) associated with
 502 a descent of the inversion top. This warming can be attributed to subsidence heating when
 503 the core of the valley subsides compensating for upslope flows carrying mass up the side-
 504 walls (Whiteman, 1982). The inversion breakup mechanisms we found in the East River
 505 Valley, namely the upward growth of a CBL under snow-free conditions and the subsi-
 506 dence heating under snow-covered conditions, are consistent with the mechanisms pro-
 507 posed by Whiteman (1982). While we did not find observational evidence for a descend-
 508 ing top of the inversion under snow-free conditions, it may exist, but might not be de-
 509 tectable due to the coarse vertical resolution of the retrieved profiles and the retrieval's
 510 inability to detect sharp elevated inversions (Djalalova et al., 2022). Unfortunately, no
 511 radio soundings were available during daytime to further investigate this.

512 4 Representation of the ABL in the HRRR model

513 4.1 Temperature errors

514 To evaluate the representation of the thermal ABL structure in the HRRR model,
 515 we computed 24-h mean composites of bias (Eq. 1) and MAE (Eq. 2) of 2-m temper-

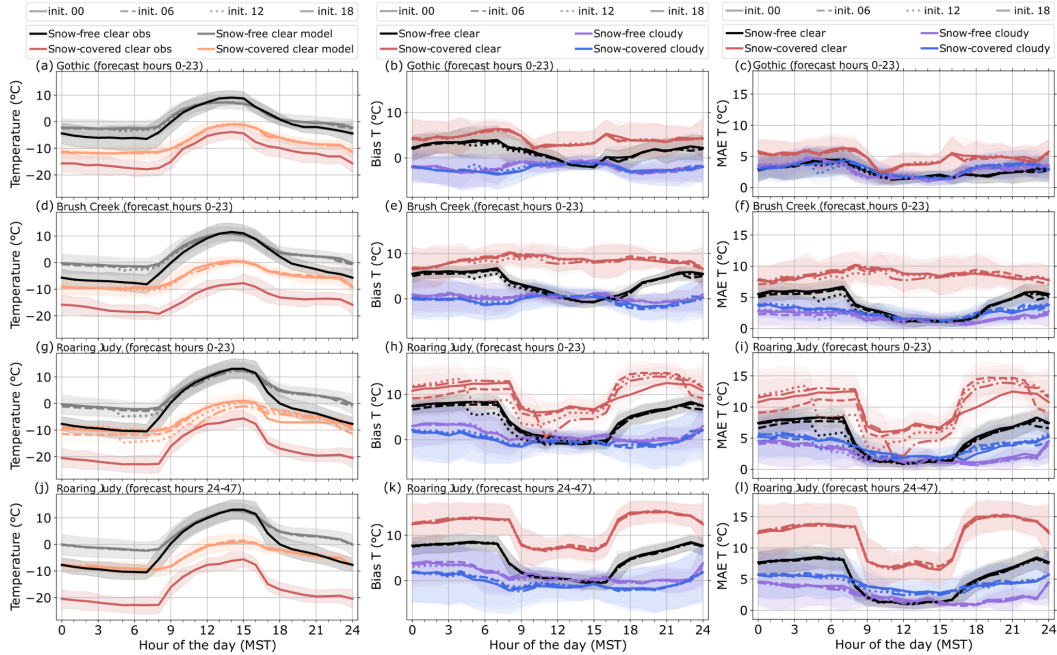


Figure 7. 24-h mean composites of (a,d,g,j) observed and simulated 2-m temperature and (b,e,h,k) bias and (c,f,i,l) mean absolute error (MAE) between simulated and observed 2-m temperature (model - observations) at Gothic, Brush Creek and Roaring Judy for clear-sky days under snow-free and snow-covered conditions. (a-i) show data from forecast hours 0-23 and (j-l) from forecast hours 24-47. The line style indicates different initialisation times (init.). Bias and MAE are additionally shown for cloudy days. The shading indicates the standard deviation.

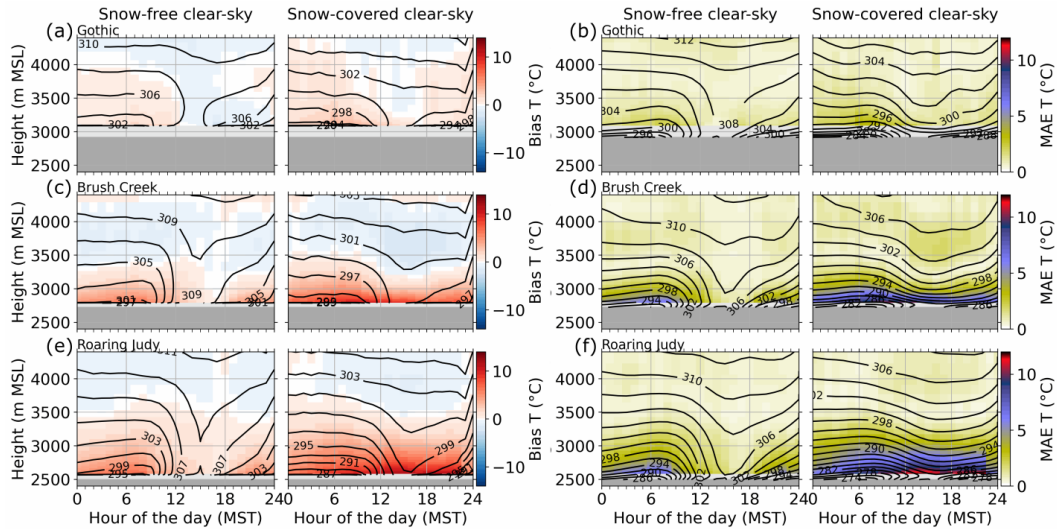


Figure 8. 24-h mean composites of (a,c,e) bias and (b,d,f) mean absolute error (MAE) profiles between simulated and observed temperature (model - observations) at Gothic, Brush Creek, and Roaring Judy for clear-sky days under snow-free and snow-covered conditions. The black iso-lines are 24-h mean composites of potential temperature simulated with the HRRR model (a,c,e) and retrieved with TROPoe (b,d,f). Model data for forecast hours 0-23 initialized at 6 UTC are shown. The dark grey shading indicates real world station height.

516 ature at Roaring Judy, Brush Creek, and Gothic (Fig. 7). On clear-sky days, the errors
 517 showed a diurnal cycle with lower values during the day and larger values during the night,
 518 except for Gothic. The errors were generally largest under snow-covered conditions. Model
 519 performance was worst at Roaring Judy with an average bias of up to 13 °C (Fig. 7h)
 520 and a MAE of up to 15 °C (Fig. 7i) during the night. The temporal evolution and mag-
 521 nitude of the errors at Gothic and Brush Creek were very similar for all initialization times
 522 (Fig. 7b,c,e,f). At Roaring Judy, however, the errors at a certain time of the day clearly
 523 depended on initialization time (Fig. 7h,i). The errors were generally lowest at the time
 524 of initialization and increased with forecast hour, as e.g. visible in the drops at 5, 11, and
 525 23 MST under snow-covered conditions. For longer forecast hours (24-47 hours) the er-
 526 rors did not depend any more on initialization time, but were equally high and showed
 527 the same diurnal cycle (shown for Roaring Judy in Fig. 7j,k,l). Maximum errors for longer
 528 forecast hours were also not markedly higher than for the configurations using the first
 529 24 forecast hours. This indicates that the time of initialization does not matter equally
 530 for all sites and that the model does not introduce ever growing errors with forecast length.
 531 Observed and simulated 2-m temperature indicates that nighttime cooling in the model,
 532 especially at the beginning of the night, is largely underestimated (Fig. 7a,d,g). After
 533 sunrise, the observed 2-m temperature increased more than the simulated one leading
 534 to a reduction in model errors, best visible at Roaring Judy. For comparison, we also com-
 535 puted the errors for cloudy days (indicated by blue and purple shading in Fig. 3). Bi-
 536 ases for these days were near 0 °C or slightly negative and MAE was usually less than
 537 5 °C, that is, much smaller than during clear-sky days.

538 The findings derived from the 2-m temperature errors generally hold for the tem-
 539 perature profiles as well. Figure 8 shows 24-hr mean composite profiles of bias and MAE
 540 as well as observed and simulated potential temperature isolines. The errors are com-
 541 puted with respect to mean sea level. Because terrain height at the individual sites was
 542 higher in the model than in the observations (Fig. 1d), the distance to the ground at a
 543 certain height was larger in the observations than in the model. In the presence of tem-
 544 perature inversions, computing the error profiles with respect to ground level would only
 545 lead to even larger MAE and positive biases than the ones shown in Fig. 8. Errors dur-
 546 ing clear-sky days were largest at lower altitude stations and increased towards the ground.
 547 This was clearly related to the failure of the model to correctly forecast the thermal strat-
 548 ification. Comparing observed (isolines in Fig. 8b,d,f) and simulated (isolines in Fig. 8a,c,e)
 549 potential temperature profiles revealed that the nocturnal strong surface inversions present
 550 in the observations at all sites independent of snow-cover were largely missing in the model.
 551 This has been identified as a common problem in NWP models (Zhong & Chow, 2013).
 552 Because the observed inversion was deepest and strongest at the lowest altitude site Roar-
 553 ing Judy (Fig. 8f), the impact of the erroneous stratification in the model was most pro-
 554 nounced here explaining the largest errors at this site (Figs. 7h,i and 8e,f). Under snow-
 555 free conditions, the warm bias and large MAE present during the night were much re-
 556 duced or even absent during daytime with the formation of a well-mixed CBL in both
 557 the model and the observations. While in the observations a strongly stably stratified
 558 layer persisted above the shallow CBL during the day under snow-covered conditions (iso-
 559 lines in Fig. 8b,d,f), the valley atmosphere was only weakly stably stratified in the model
 560 (isolines in Fig. 8a,c,e) resulting in large model errors also during daytime.

561 4.2 Possible reasons for model errors during clear-sky days

562 The smaller model errors during cloudy days suggest that the errors during clear-
 563 sky days are related to one or more physical processes which are only present or most
 564 pronounced during clear-sky days and which are not correctly represented in the model.
 565 This could be thermally driven flows such as slope and valley winds which form and are
 566 most pronounced during clear-sky days. Another possible reason could be errors in the
 567 surface radiation budget.

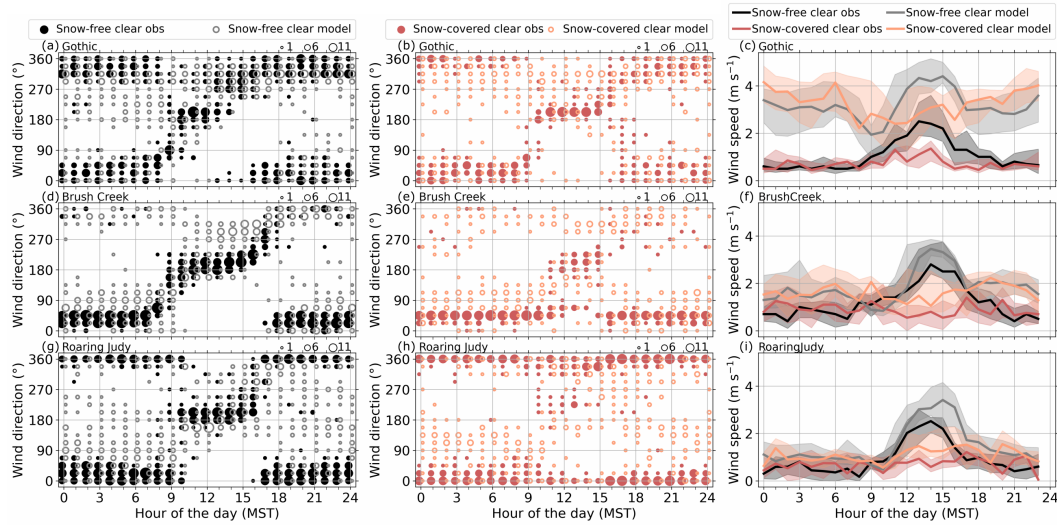


Figure 9. 24-h composites of observed and simulated near-surface (a,b,d,e,g,h) wind direction and (c,f,i) mean (solid line) wind speed at Gothic, Brush Creek and Roaring Judy for clear-sky and cloudy days under snow-free and snow-covered conditions. Model data from forecast hours 0-23 are shown. For wind direction, the marker size indicates how often a specific wind direction occurs at each time stamp using bins of 22.5 degree width. Model data for forecast hours 0-23 initialized at 6 UTC are shown. The shading in (c,f,i) indicates the standard deviation.

568

4.2.1 Thermally driven flows

569

570

571

572

573

574

575

576

577

578

579

580

581

582

583

We start with investigating the thermally driven flows by computing 24-h composites of near-surface wind speed and direction for clear-sky days (Fig. 9). Preferred wind directions are clearly visible in the observations at all three sites independent of snow cover. At Gothic, northwesterly to northeasterly flow prevailed during the night. Northwesterly flow indicates drainage along the main valley axis, while north-easterly flow was likely related to drainage outflow from a small tributary located to the north-east of Gothic (Fig. 1b). At Brush Creek and Roaring Judy, distinct downvalley wind along the main valley axis (oriented in north-easterly and northerly direction, respectively) dominated during the night. Southerly upvalley wind developed during daytime at all sites. It was more pronounced and lasted longer under snow-free conditions. When the ground was snow-covered, a shift to upvalley wind during daytime was not always observed on every day, especially at Roaring Judy and Brush Creek where downvalley wind sometimes persisted throughout the day. This lack of an upvalley wind during daytime is a common feature over glaciers or in snow-covered valleys (e.g. Obleitner, 1994; Whiteman, 2000; Song et al., 2007; Zardi & Whiteman, 2013).

584

585

586

587

588

589

590

591

592

593

Valley winds are driven by a horizontal pressure gradient along the valley axis which develops as a function of height between air columns with different vertical temperature structures in different sections of the valley (Zardi & Whiteman, 2013). During the day, the pressure at a given height is generally lower further up the valley causing an upvalley wind and vice versa during the night. The relationship between pressure difference and valley wind under clear-sky days was for example confirmed in the Inn Valley in Austria (Lehner et al., 2019) and the Adige Valley in Italy (Giovannini et al., 2017). We computed the horizontal pressure difference between Roaring Judy and Gothic after reducing the pressure at Roaring Judy to the altitude of Gothic for clear-sky days. Under snow-free conditions, we found a diurnal cycle of the pressure difference with Gothic having

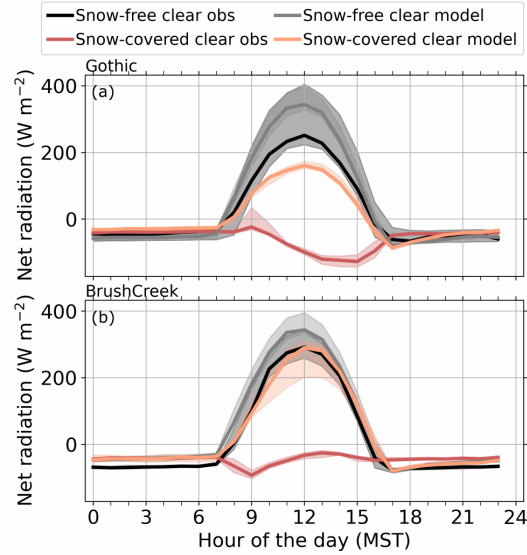


Figure 10. 24-h mean composites of observed and simulated net radiation at Gothic and Brush Creek for clear-sky days under snow-free and snow-covered conditions. Model data for forecast hours 0-23 initialized at 6 UTC are shown. The shading indicates the standard deviation.

594 lower pressure during the day and higher pressure during the night (not shown) which
 595 is consistent with the diurnal cycle in wind direction (Fig. 9a,d,g). Under snow-covered
 596 conditions, hardly any diurnal cycle in pressure difference was distinguishable which again
 597 agrees with the less distinct diurnal cycle in wind direction (Fig. 9b,e,f).

598 With the coarse model resolution, the fine-scale structure of the valley, such as the
 599 small tributary north-east of Gothic, is not resolved (Fig. 1c) and we did not expect the
 600 model to get all the details of the observed thermally driven flows right. Nevertheless,
 601 we were surprised by the absence of valley winds in the model data (Fig. 9). Wind di-
 602 rection was much more scattered than in the observations at all sites independent of snow-
 603 cover and a clear diurnal cycle was missing. The overestimation of near-surface horizon-
 604 tal wind speed especially visible at Gothic, may be an indication that stronger upper-
 605 level wind was able to penetrate into the weakly stably stratified valley atmosphere. The
 606 failure of the model to correctly simulate the nighttime drainage flows provides a possi-
 607 ble explanation for the large errors in the ABL thermal structure (Sect. 4.1). Drainage
 608 flows transport cold high-density air that forms near the surface due to radiative cool-
 609 ing from higher parts of the valley to lower parts which leads to the accumulation of cold
 610 air on the valley floor and the buildup of a temperature inversion. The wind and tem-
 611 perature observations provide strong evidence that this was the main process responsi-
 612 ble for the formation of the observed strong nocturnal inversions. We hypothesize that
 613 because drainage flows were largely missing in the model (Fig. 9), no strong nocturnal
 614 inversions could form and they were easily mixed out during daytime (Fig. 8). In par-
 615 ticular under snow-covered conditions, this could lead to the very large errors in the layer
 616 where the stable stratification was maintained in the observations.

617 4.2.2 Surface radiation budget

618 An underprediction of radiative cooling at night could add to the warm nighttime
 619 biases. We therefore computed 24-h median composites of observed and simulated net

radiation under both snow-cover conditions at Gothic and Brush Creek (Fig. 10). No radiation measurements were available at Roaring Judy. Nighttime net radiation was negative and on the same order of magnitude in both the model and the observations, ruling out errors in the surface radiation budget as a relevant reason for the warm surface air temperature biases and too weak nighttime inversions in the model.

In contrast to nighttime, huge differences in net radiation are visible during daytime under snow-covered conditions. We found that this is largely related to an underprediction of albedo in the model over snow-covered ground, which was less than 0.55 in the model compared to more than 0.9 in the observations (Fig. 3e). While snow was present in the whole valley during the snow-covered regime as evident from satellite observations, snow frequently melted during daytime in the 24-h forecasts in the lower parts of the valley where simulated snow depth was lower. This indicates weaknesses in simulated snow-melting rates. The HRRR did not show a dry bias with respect to 2-m water vapor mixing ratio in the lower part of the valley (not shown). The warm bias, however, led to an underestimation of 2-m relative humidity which could enhance snow melt. The HRRR model uses the Rapid Update Cycle (RUC) LSM in which snow albedo depends on vegetation type, snow age, snow depth, snow cover, and snow temperature (Smirnova et al., 2016). Reasons for the erroneous representation of albedo and snow cover might be related to the missing representation of subgrid variability of snow in the current RUC LSM (He et al., 2021), biases introduced by the current data assimilation system (Benjamin et al., 2022; Dowell et al., 2022), or other potential errors in the physics parameterizations. He et al. (2021) showed that estimates of snow cover fraction are improved and surface heat fluxes are more realistic when coupling a stochastic snow model to the RUC LSM to represent the subgrid variability of snow. Modifications to both the land and atmospheric data assimilation system and to the RUC LSM will be addressed by the new Rapid Refresh Forecast System (RRFS), which is currently under development as part of NOAA’s Unified Forecast System. It is expected that the RRFS will become the operational 3-km grid model, replacing the HRRR, in 2024.

Even though albedo differences are large and likely have implications for the land-atmosphere exchange during daytime and may contribute to the mix out of the simulated nighttime inversion, we do not think that they are the main reason for the large temperature errors. Instead we suspect the missing drainage flows. In a future study, we plan to run a nested simulation with smaller horizontal grid spacing to test if higher horizontal resolution allows to better simulate the thermally driven circulations in the East River Valley.

5 Summary and conclusions

In this study, we analyzed the response of the ABL to changes in the surface energy balance on clear-sky days during the seasonal transition from snow-free to snow-covered ground in the East River Valley near Crested Butte in Colorado’s Rocky Mountains over a three-month period from October 2021 to January 2022. The simultaneous deployment of three infrared spectrometers provided a unique opportunity to study the thermal structure of the valley ABL. Temperature profiles were obtained from infrared spectrometer radiances using the optimal estimation physical retrieval TROPoe. We further evaluated NOAA’s operational HRRR model with the observations to assess how well the model captures primary ABL characteristics under different snow-cover conditions.

The three-month observation period can roughly be divided in half, with mostly snow-free conditions during the first 6 weeks and snow-covered conditions after a multi-day snowfall event at the beginning of December. The changes in snow cover were associated with changes in observed surface albedo which increased from less than 0.3 to more than 0.9. Under snow-covered conditions, daily mean net radiation was directed

671 upwards from the surface indicating radiative cooling, sensible heat flux was directed down-
672 wards in turn compensating for some of the radiative cooling, and daily minimum and
673 maximum 2-m air temperature values dropped with maximum values usually below freez-
674 ing. Strong diurnal cycles in low-level air temperature were observed on clear-sky days
675 throughout the whole period with the formation of a daytime CBL and a nocturnal sur-
676 face inversion, which was strongest and deepest at the Roaring Judy site, located fur-
677 thest down the valley. After an initial growth phase, the top of the inversion with respect
678 to sea level was roughly the same at all three sites, indicating that a layered cold air pool
679 filled the whole valley during nighttime. While the stable stratification in the valley was
680 mostly mixed out during the day under snow-free conditions, a persistent inversion was
681 present above a very shallow CBL under snow-covered conditions.

682 The HRRR model showed a large nocturnal warm bias in the ABL on clear-sky days
683 (up to 13 °C at 2 m AGL under snow-covered conditions), because the model failed to
684 form strong nocturnal inversions. The errors decreased with formation of the CBL dur-
685 ing daytime. Unlike in the observations, where an inversion persisted above a very shal-
686 low CBL during the day under snow-covered conditions, much weaker simulated night-
687 time inversions were mostly mixed out, leading to large warm biases above the observed
688 CBL in the valley atmosphere during daytime. The model errors were much smaller on
689 cloudy days. We assert the main reason for the large temperature errors is a failure of
690 the model to correctly simulate the thermally driven flows in the East River Valley. While
691 nighttime drainage flows are a very clear and persistent feature in the observations, they
692 are largely missing in the simulations. A future study will use a higher-resolution sim-
693 ulation to investigate if that inability of the HRRR to simulate the thermally driven flow
694 was due to its 3-km grid spacing.

695 We showed that with careful processing, temperature profiles retrieved with TROPoe
696 from ground-based passive remote sensing infrared spectrometers are suited to study the
697 ABL evolution in complex terrain. With a temporal resolution of minutes, these retrievals
698 are able to resolve diurnal changes in stratification under different snow-cover conditions.
699 While we focused on clear-sky days only, temperature profiles can also be retrieved un-
700 der cloud base and the response of lower tropospheric stability and subsequent surface
701 energy fluxes to radiatively clear and cloudy conditions is the subject of another study
702 (Sedlar et al. (n.d.)). The ABL plays a crucial role in the temporal evolution of seasonal
703 snow cover, particularly during spring snowmelt. The continuous temperature profiles
704 retrieved with TROPoe can provide invaluable information on the ABL thermal struc-
705 ture during the seasonal changes.

706 Retrieved temperature profiles proved further to be very useful for the model eval-
707 uation of ABL structure and stratification. From near-surface measurements alone we
708 would not have been able to identify the problems the model has with simulating inver-
709 sion strength and with maintaining the persistent inversion during daytime. The chal-
710 lenges faced by the model to correctly form and maintain inversions under snow-covered
711 conditions can, for example, have implications for air quality forecasts in mountainous
712 terrain.

713 **Open Research Section**

714 Measurements at Gothic are part of the Atmospheric Radiation Measurement (ARM)
715 Mobile Facility (AMF2). The used data at Gothic are AERI radiances (Gero et al., 2021),
716 radiosonde profiles (Burk, 2021), ceilometer cloud base height (Morris et al., 2021), ra-
717 diation flux components (Shi, 2021b, 2021a), sensible heat flux (Sullivan et al., 2021),
718 near-surface meteorological standard measurements (Keeler et al., 2021), and precipi-
719 tation measurements (Cromwell & Bartholomew, 2021). NOAA Global Monitoring Lab-
720 oratory conducted the ceilometer (NOAA Global Monitoring Laboratory, 2021b) and ra-
721 diation (NOAA Global Monitoring Laboratory, 2021c) measurements at Kettle Ponds

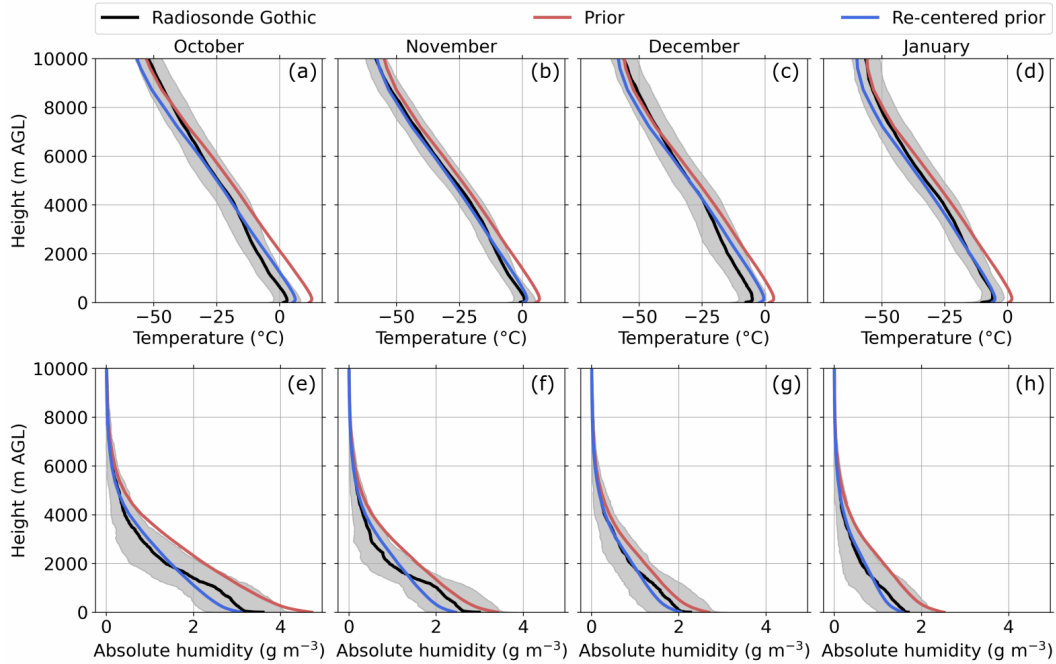


Figure A1. Monthly profiles of (a-d) temperature and (e-h) absolute humidity. The twice daily radiosonde launches at Gothic are averaged for each month with the shading showing the standard deviation. The red line shows the climatological prior computed from radiosonde launches at Denver and the green line shows the profiles after the prior was re-centered using the monthly mean IWV values from the radio soundings at Gothic.

722 and the ceilometer (NOAA Global Monitoring Laboratory, 2021a) and radiation (NOAA
 723 Global Monitoring Laboratory, 2021d) measurements at Brush Creek. NOAA Air Re-
 724 sources Laboratory provided sensible heat flux measurements at Brush Creek. NOAA
 725 Physical Science Laboratory conducted the Atmospheric Surface Flux Stations (ASFS)
 726 measurements at Avery Picnic and Kettle Ponds (NOAA Physical Science Laboratory,
 727 2021a), and surface meteorology (NOAA Physical Science Laboratory, 2021c), ASSIST
 728 (Adler, Bianco, Djalalova, Myers, & Wilczak, 2022), and ceilometer (Adler, Bianco, Djalalova,
 729 Myers, Pezoa, et al., 2022) measurements at Roaring Judy. The AERI data at Brush Creek
 730 (NOAA National Severe Storms Laboratory, 2021) were collected as part of the Collab-
 731 orative Lower Atmospheric Profiling System (CLAMPS) by NOAA National Severe Storms
 732 Laboratory.

733 Appendix A Re-centering of the prior

734 Although radiosondes are launched twice daily at the AMF2 at Gothic, the num-
 735 ber of these soundings is not enough to compute the level-to-level covariance for the 110-
 736 element state vector of the prior needed for the TROPoe retrievals. Instead, we computed
 737 monthly priors using the operational radio soundings launched at Denver, CO, just east
 738 of the Rocky Mountains. Although the horizontal distance between the East River Val-
 739 ley and the launch site at Denver is only around 220 km, the elevation difference is 1300
 740 m and the atmospheric conditions can be quite different between the central Rocky Moun-
 741 tains and Denver. To account for differences in the integrated water vapor (IWV) in the
 742 atmospheric column due to the elevation difference and to avoid systematic offsets in the
 743 prior, we re-centered the mean prior profiles while preserving the relative humidity pro-

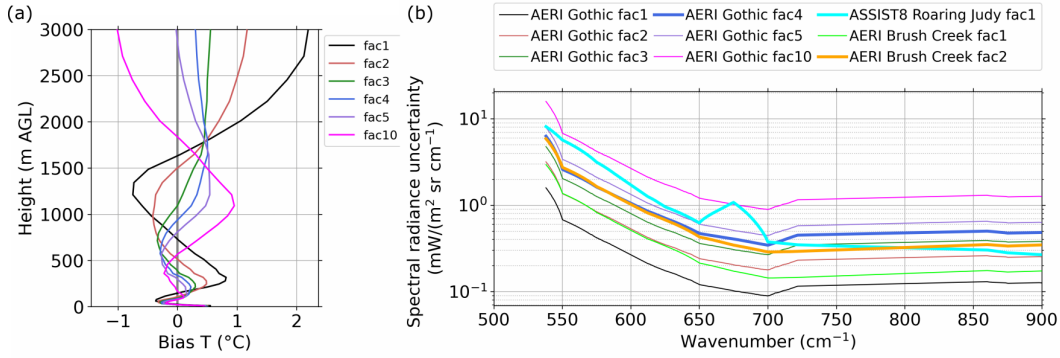


Figure B1. (a) Mean bias between the temperature profiles retrieved with TROPoe for the AERI at Gothic and colocated radio soundings (retrieved profile - radiosonde profile). (b) Mean spectral radiance uncertainty for the AERIs at Gothic and Brush Creek and the ASSIST at Roaring Judy. fac1 indicates that the original uncertainty radiance was used, fac2, fac3, fac4, fac5, and fac10 indicates that the uncertainty radiance was multiplied with a factor of 2, 3, 4, 5, and 10, respectively.

744 files. We borrowed the concept of recentering from the data assimilation community (e.g.
 745 Wang et al., 2013), as TROPoe essentially is a 1-dimensional data assimilation frame-
 746 work. We computed the ratio of the monthly mean IWV from radio soundings at Gothic
 747 and the mean IWV of the prior and multiplied the prior mixing ratio profile by this fac-
 748 tor. We then adjusted the temperature profile to preserve the relative humidity from the
 749 original prior. The re-centered monthly mean prior profiles agreed very well with monthly
 750 mean radiosonde profiles at Gothic (Fig. A1).

751 Appendix B AERI noise modification for TROPoe

752 The radiance uncertainty of the ARM AERI at Gothic and the CLAMPS AERI
 753 at Brush Creek was not large enough to compensate for the missing uncertainty of the
 754 forward model in TROPoe which led to unrealistic profiles at Brush Creek and Gothic
 755 (temperature inversion always between about 1500 and 2000 m AGL), which indicated
 756 an overfitting of the temperature profiles. Figure B1b indicates that the noise of the AERI
 757 at Gothic is about a factor of 4 smaller and the noise of the AERI at Brush Creek is about
 758 a factor of 2 smaller than the noise of the ASSIST at Roaring Judy. We ran the retrieval
 759 for the AERI at Gothic at the time of the radiosonde launches, i.e. at 0 and 12 UTC,
 760 for the whole investigation period (92 profiles) and computed the mean differences be-
 761 tween the temperature profiles (black line in Fig. B1a). Large differences are visible
 762 with a warm bias below around 750 m AGL, a cold bias between 750 m and 1600 m AGL,
 763 and a strong warm bias above 1600 m AGL, which is consistent with the unrealistic temper-
 764 ature inversion in the retrieved temperature profiles.

765 We then systematically increased the noise of the AERI at Gothic by multiplying
 766 the spectral radiance uncertainties by the factors 2, 3, 4, 5, and 10 and ran TROPoe with
 767 each increased noise level. The spectral radiance uncertainties for the different config-
 768 urations are shown in Fig. B1b and the resulting temperature bias profiles are shown in
 769 Fig. B1a. We decided to use a factor 4 for the AERI at Gothic because (i) the radiance
 770 uncertainty was then the same order of magnitude as the ASSIST and (ii) the warm bias
 771 above around 1600 m AGL and the cold bias below were much reduced. Even though
 772 no radiosonde profiles were available to compare to the retrieved profiles at Brush Creek,

773 we decided to increase the radiance uncertainty for the AERI there by a factor of 2 to
774 have similar uncertainty radiance values for all three infrared radiometers.

775 Acknowledgments

776 We thank all of the individuals, in particular Rocky Mountain Biological Laboratory (RMBL),
777 for help with the SPLASH site selection, leases, instrument deployment and maintenance,
778 data collection, and data quality control. Funding for this work was provided by the NOAA
779 Physical Sciences Laboratory, the U.S. Department of Energy (DOE) Office of Energy
780 Efficiency and Renewable Energy, Wind Energy Technologies Office, and by the NOAA
781 Atmospheric Science for Renewable Energy program. This work was supported by NOAA
782 cooperative agreements NA17OAR4320101 and NA22OAR4320151.

783 References

- 784 Adler, B., Bianco, L., Djalalova, I., Myers, T., Pezoa, S., Bariteau, L., & Wilczak, J.
785 (2022). *NOAA PSL CL31 Ceilometer Backscatter and Cloud Base Height Data*
786 *for SPLASH* [dataset]. Zenodo. doi: 10.5281/zenodo.7438524
- 787 Adler, B., Bianco, L., Djalalova, I., Myers, T., & Wilczak, J. (2022). *NOAA PSL*
788 *thermodynamic profiles retrieved from ASSIST infrared radiances with the opti-*
789 *mal estimation physical retrieval TROPoe during SPLASH* [dataset]. Zenodo.
790 doi: 10.5281/zenodo.7435060
- 791 Adler, B., Gohm, A., Kalthoff, N., Babić, N., Corsmeier, U., Lehner, M., ... Geor-
792 gousis, G. (2021). CROSSINN: a field experiment to study the three-
793 dimensional flow structure in the Inn Valley, Austria. *Bull. Amer. Meteor.*
794 *Soc.*, 102(1), E38–E60. doi: 10.1175/BAMS-D-19-0283.1
- 795 Adler, B., & Kalthoff, N. (2014). Multi-scale transport processes observed in the
796 boundary layer over a mountainous island. *Boundary-Layer Meteorol.*, 153,
797 515–537. doi: 10.1007/s10546-014-9957-8
- 798 Adler, B., Wilczak, J. M., Bianco, L., Djalalova, I., Duncan Jr, J. B., & Turner,
799 D. D. (2021). Observational case study of a persistent cold pool and gap flow
800 in the Columbia River Basin. *J. Appl. Meteor. Climatol.*, 60(8), 1071–1090.
801 doi: 10.1175/JAMC-D-21-0013.1
- 802 Adler, B., Wilczak, J. M., Kenyon, J., Bianco, L., Djalalova, I. V., Olson, J. B., &
803 Turner, D. D. (2022). Evaluation of a cloudy cold-air pool in the Columbia
804 River Basin in different versions of the HRRR model. *EGUsphere*, 2022, 1–32.
805 doi: 10.5194/egusphere-2022-355
- 806 Benjamin, S. G., Smirnova, T. G., James, E. P., Lin, L.-F., Hu, M., Turner, D. D.,
807 & He, S. (2022). Land–snow data assimilation including a moderately coupled
808 initialization method applied to NWP. *J. Hydrometeorol.*, 23(6), 825–845. doi:
809 10.1175/JHM-D-21-0198.1
- 810 Benjamin, S. G., Weygandt, S. S., Brown, J. M., Hu, M., Alexander, C. R.,
811 Smirnova, T. G., ... others (2016). A North American hourly assimilation
812 and model forecast cycle: The Rapid Refresh. *Mon. Wea. Rev.*, 144(4), 1669–
813 1694. doi: 10.1175/MWR-D-15-0242.1
- 814 Burk, K. (2021). *Balloon-Borne Sounding System (SONDEWNP)*. doi: 10.5439/
815 1595321
- 816 Butterworth, B. J., Desai, A. R., Townsend, P. A., Petty, G. W., Andresen, C. G.,
817 Bertram, T. H., ... others (2021). Connecting land–atmosphere interactions to
818 surface heterogeneity in CHEESEHEAD19. *Bull. Amer. Meteor. Soc.*, 102(2),
819 E421–E445. doi: 10.1175/BAMS-D-19-0346.1
- 820 Chemel, C., Arduini, G., Staquet, C., Llargeron, Y., Legain, D., Tzanos, D., & Paci,
821 A. (2016). Valley heat deficit as a bulk measure of wintertime particulate
822 air pollution in the Arve River Valley. *Atmos. Env.*, 128, 208–215. doi:
823 10.1016/j.atmosenv.2015.12.058

- 824 Clough, S. A., & Iacono, M. J. (1995). Line-by-line calculation of atmospheric fluxes
825 and cooling rates: 2. application to carbon dioxide, ozone, methane, nitrous
826 oxide and the halocarbons. *J. Geophys. Res.: Atmos.*, *100*(D8), 16519–16535.
827 doi: 10.1029/95JD01386
- 828 Clough, S. A., Shephard, M. W., Mlawer, E. J., Delamere, J. S., Iacono, M. J.,
829 Cady-Pereira, K., . . . Brown, P. D. (2005, March). Atmospheric radiative
830 transfer modeling: a summary of the AER codes. *J. Quant. Spectrosc. Radiat.*
831 *Transf.*, *91*(2), 233–244. doi: 10.1016/j.jqsrt.2004.05.058
- 832 Cox, C. J., Gallagher, M., Shupe, M., Persson, P., Solomon, A., Ayers, T., . . . Ut-
833 tal, T. (2023). Continuous observations of the surface energy budget and
834 meteorology over arctic sea ice during mosaic. *Nature Scientific Data, to be*
835 *submitted*.
- 836 Cromwell, E., & Bartholomew, M. (2021). *Weighing Bucket Precipitation Gauge*
837 *(WBPLUVIO2)*. doi: 10.5439/1338194
- 838 Cullen, N. J., & Conway, J. P. (2015). A 22 month record of surface meteorology
839 and energy balance from the ablation zone of Brewster Glacier, New Zealand.
840 *J. Glaciol.*, *61*(229), 931–946. doi: 10.3189/2015JoG15J004
- 841 Djalalova, I. V., Turner, D. D., Bianco, L., Wilczak, J. M., Duncan, J., Adler,
842 B., & Gottas, D. (2022, January). Improving thermodynamic profile re-
843 trievals from microwave radiometers by including radio acoustic sounding
844 system (RASS) observations. *Atmos. Meas. Tech.*, *15*(2), 521–537. doi:
845 10.5194/amt-15-521-2022
- 846 Dowell, D. C., Alexander, C. R., James, E. P., Weygandt, S. S., Benjamin, S. G.,
847 Manikin, G. S., . . . Alcott, T. I. (2022). The High-Resolution Rapid Refresh
848 (HRRR): An hourly updating convection-allowing forecast model. part i: Mo-
849 tivation and system description. *Wea. Forecasting*, *37*(8), 1371 - 1395. doi:
850 10.1175/WAF-D-21-0151.1
- 851 Duncan Jr., J. B., Bianco, L., Adler, B., Bell, T., Djalalova, I. V., Riihimaki, L., . . .
852 Wilczak, J. M. (2022). Evaluating convective planetary boundary layer height
853 estimations resolved by both active and passive remote sensing instruments
854 during the CHEESEHEAD19 field campaign. *Atmos. Meas. Tech.*, *15*(8),
855 2479–2502. doi: 10.5194/amt-15-2479-2022
- 856 Feldman, D., Aiken, A., Boos, W., Carroll, R., Chandrasekar, V., Collins, W., . . .
857 Williams, K. (2021). *Surface atmosphere integrated field laboratory (sail)*
858 *science plan* (Tech. Rep. No. DOE/SC-ARM-21-004). ARM user facility.
- 859 Gero, J., Garcia, R., Hackel, D., Ermold, B., & Gaustad, K. (2021). *Atmospheric*
860 *Emitted Radiance Interferometer (AERICH1)*. (Date accessed: 2022-08-21)
861 doi: 10.5439/1025143
- 862 Giovannini, L., Laiti, L., Serafin, S., & Zardi, D. (2017). The thermally driven di-
863 urnal wind system of the Adige Valley in the Italian Alps. *Quart. J. Roy. Me-*
864 *teor. Soc.*, *143*(707), 2389–2402. doi: 10.1002/qj.3092
- 865 Hall, D. K., & Riggs, G. A. (2021). *MODIS/Terra Snow Cover Daily L3*
866 *Global 500m SIN Grid, Version 61*. NASA National Snow and Ice Data
867 Center Distributed Active Archive Center. Retrieved 2022-08-21, from
868 <https://nsidc.org/data/MOD10A1/versions/61> (Date accessed: 2022-
869 08-21) doi: 10.5067/MODIS/MOD10A1.061
- 870 He, S., Smirnova, T. G., & Benjamin, S. G. (2021). Single-Column validation of a
871 snow subgrid parameterization in the Rapid Update Cycle Land-Surface Model
872 (RUC LSM). *Water Resources Res.*, *57*(8). doi: 10.1029/2021WR029955
- 873 Herrera-Mejía, L., & Hoyos, C. D. (2019). Characterization of the atmospheric
874 boundary layer in a narrow tropical valley using remote-sensing and radiosonde
875 observations and the WRF model: the Aburrá Valley case-study. *Quart. J.*
876 *Roy. Meteor. Soc.*, *145*(723), 2641–2665. doi: 10.1002/qj.3583
- 877 Keeler, E., Kyrouac, J., & Ermold, B. (2021). *Automatic Weather Station (MAWS)*.
878 doi: 10.5439/1182027

- 879 Knuteson, R., Revercomb, H., Best, F., Ciganovich, N., Dedecker, R., Dirkx, T.,
880 ... others (2004a). Atmospheric emitted radiance interferometer. Part II:
881 Instrument performance. *J. Atmos. Oceanic Technol.*, *21*(12), 1777–1789. doi:
882 10.1175/JTECH-1663.1
- 883 Knuteson, R., Revercomb, H., Best, F., Ciganovich, N., Dedecker, R., Dirkx, T.,
884 ... others (2004b). Atmospheric emitted radiance interferometer. Part I:
885 Instrument design. *J. Atmos. Oceanic Technol.*, *21*(12), 1763–1776. doi:
886 10.1175/JTECH-1662.1
- 887 Lareau, N. P., Crosman, E., Whiteman, C. D., Horel, J. D., Hoch, S. W., Brown,
888 W. O., & Horst, T. W. (2013). The persistent cold-air pool study. *Bull. Amer.*
889 *Meteor. Soc.*, *94*(1), 51–63. doi: 10.1175/BAMS-D-11-00255.1
- 890 LARGERON, Y., & STAQUET, C. (2016a). The atmospheric boundary layer during win-
891 tertime persistent inversions in the Grenoble Valleys. *Front. Earth Sci.*, *4*. doi:
892 10.3389/feart.2016.00070
- 893 LARGERON, Y., & STAQUET, C. (2016b). Persistent inversion dynamics and wintertime
894 PM10 air pollution in Alpine valleys. *Atmos. Env.*, *135*, 92–108. doi: 10.1016/
895 j.atmosenv.2016.03.045
- 896 Lehner, M., Rotach, M. W., & Obleitner, F. (2019). A method to identify syn-
897 optically undisturbed, clear-sky conditions for valley-wind analysis. *Boundary-*
898 *Layer Meteorol.*, *173*(3), 435–450. doi: 10.1007/s10546-019-00471-2
- 899 McArthur, L. (2005). *World Climate Research Programme - Baseline Surface Radi-*
900 *ation Network (BSRN)-Operations Manual Version 2.1*. Experimental Studies
901 Division, Atmospheric Environment Service. Retrieved from [https://library](https://library.wmo.int/index.php?lvl=notice_display&id=11762)
902 [.wmo.int/index.php?lvl=notice_display&id=11762](https://library.wmo.int/index.php?lvl=notice_display&id=11762)
- 903 Morris, V., Zhang, D., & Ermold, B. (2021). *Ceilometer (ceil)*. doi: 10.5439/
904 1181954
- 905 Mott, R., Vionnet, V., & Grünewald, T. (2018). The seasonal snow cover dynam-
906 ics: review on wind-driven coupling processes. *Front. Earth Sci.*, *6*, 197. doi:
907 10.3389/feart.2018.00197
- 908 NOAA Global Monitoring Laboratory. (2021a). *Ceilometer CL51 Brush Creek*
909 [dataset]. Retrieved 2022-11-16, from [https://gml.noaa.gov/aftp/g-rad/](https://gml.noaa.gov/aftp/g-rad/surfrad/ceilometer/cl51_cloud_prod_lev0/cbc/)
910 [surfrad/ceilometer/cl51_cloud_prod_lev0/cbc/](https://gml.noaa.gov/aftp/g-rad/surfrad/ceilometer/cl51_cloud_prod_lev0/cbc/)
- 911 NOAA Global Monitoring Laboratory. (2021b). *Ceilometer CL51 Kettle Ponds*
912 [dataset]. Retrieved 2022-11-16, from [https://gml.noaa.gov/aftp/g-rad/](https://gml.noaa.gov/aftp/g-rad/surfrad/ceilometer/cl51_cloud_prod_lev0/ckp/)
913 [surfrad/ceilometer/cl51_cloud_prod_lev0/ckp/](https://gml.noaa.gov/aftp/g-rad/surfrad/ceilometer/cl51_cloud_prod_lev0/ckp/)
- 914 NOAA Global Monitoring Laboratory. (2021c). *Radiation and surface meteorological*
915 *station Brush Creek* [dataset]. Retrieved 2022-11-16, from [https://gml.noaa](https://gml.noaa.gov/aftp/data/radiation/campaigns/Format/ckp/)
916 [.gov/aftp/data/radiation/campaigns/Format/ckp/](https://gml.noaa.gov/aftp/data/radiation/campaigns/Format/ckp/)
- 917 NOAA Global Monitoring Laboratory. (2021d). *Radiation and surface meteorological*
918 *station Brush Creek* [dataset]. Retrieved 2022-11-16, from [https://gml.noaa](https://gml.noaa.gov/aftp/data/radiation/campaigns/Format/cbc/)
919 [.gov/aftp/data/radiation/campaigns/Format/cbc/](https://gml.noaa.gov/aftp/data/radiation/campaigns/Format/cbc/)
- 920 NOAA National Severe Storms Laboratory. (2021). *Collaborative Lower Atmo-*
921 *spheric Profiling System Brush Creek* [dataset]. Retrieved 2022-11-16, from
922 [https://data.nssl.noaa.gov/thredds/catalog/FRDD/CLAMPS/clamps/](https://data.nssl.noaa.gov/thredds/catalog/FRDD/CLAMPS/clamps/clamps2/ingested/catalog.html)
923 [clamps2/ingested/catalog.html](https://data.nssl.noaa.gov/thredds/catalog/FRDD/CLAMPS/clamps/clamps2/ingested/catalog.html)
- 924 NOAA Physical Science Laboratory. (2021a). *Atmospheric Surface Flux Statios*
925 *(ASFS)* [dataset]. Retrieved 2022-11-16, from [ftp://ftp1.esrl.noaa.gov/](ftp://ftp1.esrl.noaa.gov/Observations/Campaigns/SPLASH/)
926 [Observations/Campaigns/SPLASH/](ftp://ftp1.esrl.noaa.gov/Observations/Campaigns/SPLASH/)
- 927 NOAA Physical Science Laboratory. (2021b). *SPLASH - Study of Precipitation,*
928 *the Lower Atmosphere, and Surface for Hydrometeorology* [website]. Retrieved
929 2022-08-04, from <https://psl.noaa.gov/splash/>
- 930 NOAA Physical Science Laboratory. (2021c). *Surface meteorological station Roaring*
931 *Judy* [dataset]. Retrieved 2022-11-16, from [https://psl.noaa.gov/data/obs/](https://psl.noaa.gov/data/obs/sites/view_site_details.php?siteID=rjy)
932 [sites/view_site_details.php?siteID=rjy](https://psl.noaa.gov/data/obs/sites/view_site_details.php?siteID=rjy)
- 933 Obleitner, F. (1994). Climatological features of glacier and valley winds at the

- 934 Hintereisferner (Ötztal Alps, Austria). *Theor. Appl. Climatol.*, 49(4), 225–239.
 935 Retrieved 2022-09-09, from <http://link.springer.com/10.1007/BF00867462>
 936 doi: 10.1007/BF00867462
- 937 Rochette, L., Smith, W. L., Howard, M., & Bratcher, T. (2009). ASSIST, Atmo-
 938 spheric Sounder Spectrometer for Infrared Spectral Technology: latest devel-
 939 opment and improvement in the atmospheric sounding technology. In *Imaging*
 940 *spectrometry xiv* (Vol. 7457, pp. 9–17). doi: 10.1117/12.829344
- 941 Sedlar, J., Meyers, T., Adler, B., & Cox, C. (n.d.). Low-level liquid-bearing clouds
 942 drive lower atmosphere stability and surface energy forcing over a seasonally
 943 snow-covered high-mountain watershed environment.
- 944 Sedlar, J., Riihimaki, L., Turner, D., Duncan, J., Adler, B., Bianco, L., . . . others
 945 (2022). Investigating the impacts of daytime boundary layer clouds on sur-
 946 face energy fluxes and boundary layer structure during CHEESEHEAD19. *J.*
 947 *Geophys. Res.*, 127(5), e2021JD036060. doi: 10.1029/2021JD036060
- 948 Seibert, P., Beyrich, F., Gryning, S.-E., Joffre, S., Rasmussen, A., & Tercier, P.
 949 (2000). Review and intercomparison of operational methods for the de-
 950 termination of the mixing height. *Atmos. Env.*, 34(7), 1001–1027. doi:
 951 10.1016/S1352-2310(99)00349-0
- 952 Serafin, S., Adler, B., Cuxart, J., De Wekker, S., Gohm, A., Grisogono, B., . . . oth-
 953 ers (2018). Exchange processes in the atmospheric boundary layer over
 954 mountainous terrain. *Atmosphere*, 9(3), 102. doi: 10.3390/atmos9030102
- 955 Shi, Y. (2021a). *Ground Radiometers on Stand for Upwelling Radiation (GN-*
 956 *DRAD60S)*. (Date accessed: 2022-08-21) doi: 10.5439/1377837
- 957 Shi, Y. (2021b). *Sky Radiometers on Stand for Downwelling Radiation*
 958 *(SKYRAD60S)*. (Date accessed: 2022-08-21) doi: 10.5439/1377836
- 959 Skamarock, W. C. (2004, December). Evaluating mesoscale NWP models using ki-
 960 netic energy spectra. *Mon. Wea. Rev.*, 132(12), 3019–3032. Retrieved 2022-
 961 09-11, from <http://journals.ametsoc.org/doi/10.1175/MWR2830.1> doi: 10
 962 .1175/MWR2830.1
- 963 Skamarock, W. C., & Klemp, J. B. (2008, March). A time-split nonhydro-
 964 static atmospheric model for weather research and forecasting applica-
 965 tions. *J. Comput. Phys.*, 227(7), 3465–3485. Retrieved 2022-09-11, from
 966 <https://linkinghub.elsevier.com/retrieve/pii/S0021999107000459>
 967 doi: 10.1016/j.jcp.2007.01.037
- 968 Smirnova, T. G., Brown, J. M., Benjamin, S. G., & Kenyon, J. S. (2016). Modifi-
 969 cations to the Rapid Update Cycle Land Surface Model (RUC LSM) available
 970 in the Weather Research and Forecasting (WRF) Model. *Mon. Wea. Rev.*,
 971 144(5), 1851–1865. doi: 10.1175/MWR-D-15-0198.1
- 972 Song, Y., Zhu, T., Cai, X., Lin, W., & Kang, L. (2007). Glacier winds in
 973 the Rongbuk Valley, north of Mount Everest: 1. Meteorological model-
 974 ing with remote sensing data. *J. Geophys. Res.*, 112(D11), D11101. doi:
 975 10.1029/2006JD007867
- 976 Stigter, E. E., Steiner, J. F., Koch, I., Saloranta, T. M., Kirkham, J. D., & Im-
 977 merzeel, W. W. (2021). Energy and mass balance dynamics of the seasonal
 978 snowpack at two high-altitude sites in the Himalaya. *Cold Regions Science and*
 979 *Technology*, 183, 103233. doi: 10.1016/j.coldregions.2021.103233
- 980 Stull, R. B. (1988). *An introduction to boundary layer meteorology*. Dordrecht, The
 981 Netherlands: Kluwer Academic Publishers, 666 pp.
- 982 Sullivan, R., Billesbach, D., Keeler, E., & Ermold, B. (2021). *Eddy Correlation Flux*
 983 *Measurement System (30ECOR)*. doi: 10.5439/1025039
- 984 Turner, D. D., & Blumberg, W. G. (2019). Improvements to the AERIOe ther-
 985 modynamic profile retrieval algorithm. *IEEE Journal of Selected Topics in Ap-
 986 plied Earth Observations and Remote Sensing*, 12(5), 1339–1354. doi: 10.1109/
 987 JSTARS.2018.2874968
- 988 Turner, D. D., Knuteson, R. O., Revercomb, H. E., Lo, C., & Dedecker, R. G.

- 989 (2006). Noise reduction of Atmospheric Emitted Radiance Interferometer
 990 (AERI) observations using principal component analysis. *J. Atmos. Oceanic*
 991 *Technol.*, *23*(9), 1223–1238. doi: 10.1175/JTECH1906.1
- 992 Turner, D. D., & Löhnert, U. (2021). Ground-based temperature and humidity
 993 profiling: combining active and passive remote sensors. *Atmos. Meas. Tech.*,
 994 *14*(4), 3033–3048. doi: 10.5194/amt-14-3033-2021
- 995 Turner, D. D., & Löhnert, U. (2014, 03). Information content and uncertainties in
 996 thermodynamic profiles and liquid cloud properties retrieved from the ground-
 997 based atmospheric emitted radiance interferometer (AERI). *J. Appl. Meteor.*
 998 *Climatol.*, *53*(3), 752–771. doi: 10.1175/JAMC-D-13-0126.1
- 999 Wagner, T. J., Klein, P. M., & Turner, D. D. (2019). A new generation of ground-
 1000 based mobile platforms for active and passive profiling of the boundary layer.
 1001 *Bull. Amer. Meteor. Soc.*, *100*(1), 137–153. doi: 10.1175/BAMS-D-17-0165.1
- 1002 Wang, X., Parrish, D., Kleist, D., & Whitaker, J. (2013). GSI 3DVar-based
 1003 ensemble-variational hybrid data assimilation for NCEP Global Forecast
 1004 System: Single-resolution experiments. *Mon. Wea. Rev.*, *141*(11), 4098–4117.
 1005 doi: 10.1175/MWR-D-12-00141.1
- 1006 Whiteman, C. D. (1982). Breakup of temperature inversions in deep mountain val-
 1007 leys. *J. Appl. Meteor.*, *21*, 270–289. doi: 10.1175/1520-0450(1982)021<0270:
 1008 BOTIID>2.0.CO;2
- 1009 Whiteman, C. D. (2000). *Mountain meteorology fundamentals and applications*. New
 1010 York: Oxford University Press, 355 pp.
- 1011 Whiteman, C. D., Bian, X., & Zhong, S. (1999). Wintertime evolution of the tem-
 1012 perature inversion in the Colorado Plateau Basin. *J. Appl. Meteor.*, *38*(8),
 1013 1103–1117. doi: 10.1175/1520-0450(1999)038<1103:WEOTTI>2.0.CO;2
- 1014 Xu, Z., Siirila-Woodburn, E. R., Rhoades, A. M., & Feldman, D. (2022). Sensitiv-
 1015 ities of subgrid-scale physics schemes, meteorological forcing, and topographic
 1016 radiation in atmosphere-through-bedrock integrated process models: A case
 1017 study in the Upper Colorado River Basin. *EGUsphere*, *2022*, 1–29. doi:
 1018 10.5194/egusphere-2022-437
- 1019 Zardi, D., & Whiteman, C. D. (2013). Diurnal mountain wind systems. In
 1020 F. K. Chow, S. F. J. De Wekker, & B. J. Snyder (Eds.), *Mountain weather*
 1021 *research and forecasting* (pp. 35–119). Dordrecht: Springer.
- 1022 Zhong, S., & Chow, F. K. (2013). Meso- and fine-scale modeling over complex ter-
 1023 rain: Parameterizations and applications. In F. K. Chow, S. F. De Wekker,
 1024 & B. J. Snyder (Eds.), *Mountain weather research and forecasting: Recent*
 1025 *progress and current challenges* (pp. 591–653). Dordrecht: Springer Nether-
 1026 lands. doi: 10.1007/978-94-007-4098-3_10